Non-Newtonian Stabilized Mass Transport Model: Applications to Thrombosis Research in Cardiovascular Hemodynamics

by

Sabrina R. Lynch

A dissertation submitted in partial fulfillment
of the requirements for the degree of
Doctor of Philosophy
(Biomedical Engineering)
in The University of Michigan
2021

Doctoral Committee:

Professor C. Alberto Figueroa, Chair
Research Associate Professor José A. Diaz, Vanderbilt University
Professor Krishna Garikipati
Associate Professor David Nordsletten

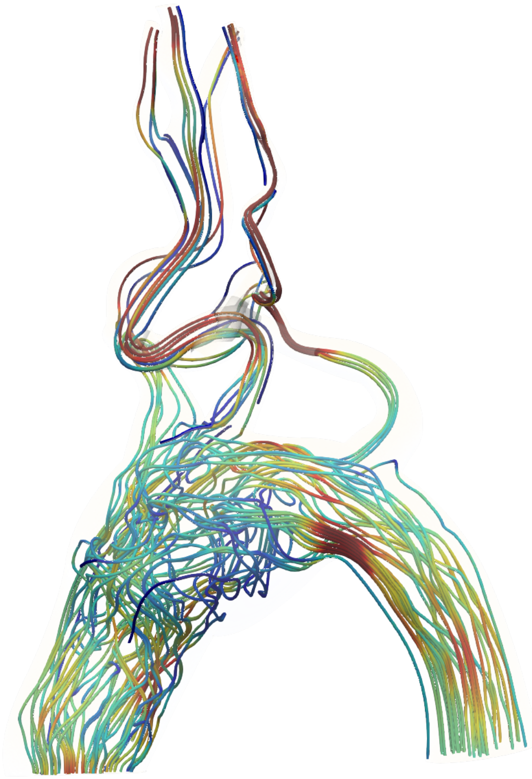

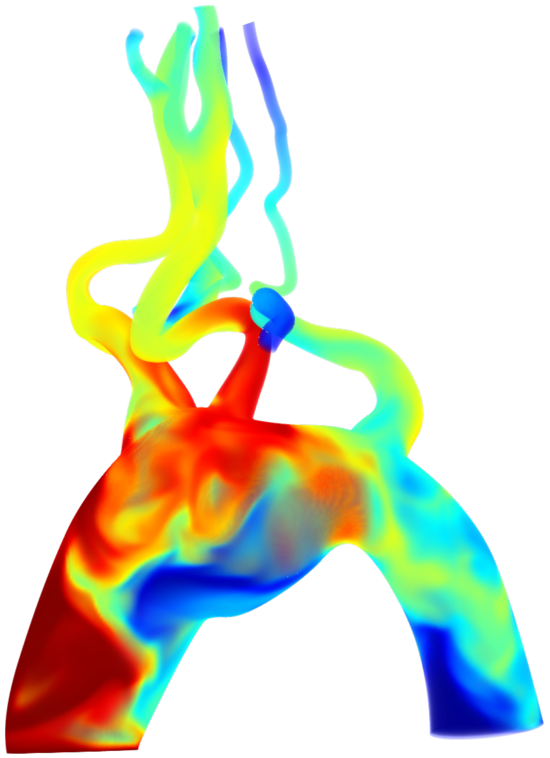

Sabrina Lynch

srlynch@umich.edu

ORCID iD: 0000-0002-5220-8861

© Sabrina Lynch 2021

To my family.

ACKNOWLEDGEMENTS

I would first like to thank two my PhD advisors Professor C. Alberto Figueroa and Professor José Diaz. I was immensely fortunate to have been mentored by two experts in numerical and experimental cardiovascular science. This combination has given me a great appreciation for the field and taught me lessons that I will always carry with me.

Professor C. Alberto Figueroa has always encouraged me to explore new opportunities and ideas. He has been a great technical instructor over the years, taking the time to educate me on many fundamental engineering principles. In addition, he has always provided insightful feedback and support that has guided my research projects. He has always been willing to spend the time to mentor me not only on science, but also on life skills. I will look back fondly on my years spent at Michigan and on the lab environment that he built. I hope that our relationship will continue to grow in the years to come.

Professor José Diaz dedicated countless hours to training me in mouse models of venous thrombosis and attending experiments. Throughout my PhD, even after moving to Vanderbilt University, he has been quick to answer questions, offer support and mentorship, and provide a good laugh. His door was always open to me, and I am grateful for his time and friendship. I thank both of my advisors for always being willing to talk and, for above all, giving me this opportunity.

I would like to provide a special thank you to my committee members: Professor David Nordsletten, for sharing his knowledge on numerical methods and his enthusiasm and support, and Professor Krishna Garikipati, for his inquisitive discussions and thoughtful questions that led me to a better understanding of my research.

I am extremely grateful to both the National Science Foundation and the American Heart Association for supporting my research during my Ph.D.

I would like to thank Professor Onkar Sahni. At the beginning on my PhD, I traveled to RPI to train on the PHASTA transport code. During my short stay at RPI, Professor Sahni provided training that has made this work possible.

Thank you to Dr. Nitesh Nama, who has been an amazing mentor to me. You have spent countless hours improving my technical knowledge and also providing life advice. Most importantly you have become a great friend. Thank you also to Dr. Christopher Arthurs, whose work made this project possible, for imparting invaluable knowledge, and for always having time for me, thank you!

A huge thank you and hug to Federica Cuomo. You have been my close ally and friend during these past five years. We have made countless memories from long days in the lab, conference travels, and much more. You always found a way to brighten my day even when it did not feel possible, and I admire your ability to always bring joy to others. Thank you for reading this dissertation and for always motivating me.

Thank you to the other members of the Figueroa lab. Thank you to Jonas Schollenberger for being a great friend and for teaching me to make authentic *brezel*. Thank you to Vasilina Filonova and Yunus Ahmed for the fun and much needed coffee breaks. Thank you to Alex Melville for motivating me to improve my coding abilities. Thank you to Sara Hopper for your kind words and for always making me laugh. Thank you to Ismael Assi for all of your hard work and for being an amazing mentee! Thank you to Christopher Tossas, Kritika Iyer, Liz Livingston, Hamid Gharahi, Jonathan Primeaux, Pieter van Bakel, Diederik van Bakel, Ignas Houben, Foeke Nauta, Sabrina Ben Ahmed, and Paula Rudenick. Thank you for the amazing supportive and collaborative environment you all created, the PhD would have not been the same without each one of you! Thank you for the unique memories and for all those moments that kept me going.

Thank you to my partner Alex for your constant support and for always believing in me.

I could not have asked for a better or braver quarantine partner.

Lastly, thank you to my family. Your endless love and support have made this possible, and I am forever grateful.

TABLE OF CONTENTS

CHAPTER

LIST OF FIGURES

LIST OF TABLES

Table

LIST OF APPENDICES

Appendix

LIST OF ABBREVIATIONS

AAA Abdominal Aortic Aneurysm

IVC Inferior Vena Cava

DVT Deep Vein Thrombosis

Pe Péclet Number

Re Reynold's Number

RAD Reaction-Advection-Diffusion

ARAD Arbitrary Reaction-Advection-Diffusion

FEM Finite Element Method

SUPG Streamline Upwind Petrov-Galerkin

DC Discontinuity Capturing

CY Carreau-Yasuda

PL Power-Law

WSS Wall Shear Stress

PLAP Platelet Activation Potential

RP Resting Platelets

AP Activated Platelets

II Prothrombin

IIa Thrombin

TF Tissue Factor

TF:VIIa Complex of Factor VIIa bound to Tissue Factor

ABSTRACT

Thrombosis is a process whereby a blood clot forms *in situ* within a vessel and impedes flow. Although necessary to maintain hemostasis, the human thrombotic system often becomes unstable leading to scenarios of thrombosis and subsequent diseases such as myocardial infarction, stroke, pulmonary embolism, and deep vein thrombosis. Computational modeling is a powerful tool to understand the complexity of thrombosis initiation and provides both temporal and spatial resolution that cannot be obtained via *in vivo* experimental techniques. The goal of this investigation is to develop a computational model of thrombosis initiation in patient-specific models that includes both a complex description of the hemodynamics and biochemistry of thrombin formation. We argue that the complex hemodynamics occurring *in vivo* significantly alter the initiation and progression of thrombosis.

While blood viscosity is known to exhibit nonlinear behavior, a Newtonian assumption is often employed in computational analyses. This assumption is valid in healthy arteries where shear rates are high and recirculation is low. However, in pathological geometries, such as aneurysms, and venous geometries, this assumption fails, and nonlinear viscous effects become exceedingly important. Previous computational models of thrombosis have investigated coagulation through chemistry based formulations focusing on protein dynamics[23,61] but have generally excluded complex 3D hemodynamics.

A computational framework was developed to investigate the interplay between 3D hemodynamics and the biochemical reactions involved in thrombosis initiation in patient-specific models under transient flow. The salient features of the framework are: *i)* nonlinear rheological models of blood flow; *ii)* a stabilized numerical framework for scalar mass transport;

and *iii)* a computational interface for nonlinear scalar models of protein dynamics that can be easily customized to include an arbitrary number of species and protein interactions.

We implemented and verified nonlinear rheological models of viscosity into CRIMSON[6] and investigated the effects of non-Newtonian viscosity on both hemodynamic and transport metrics in an arterial and venous patient-specific model. Results demonstrated the importance of considering accurate rheological models.

A stabilized finite element (FE) framework was developed to solve scalar mass transport problems in CRIMSON. Simulation of cardiovascular scalar mass transport problems offers significant numerical challenges such as highly advective flows and flow reversal at outlet boundaries. Furthermore, little attention has been given to the identification of appropriate outflow boundary conditions that preserve the accuracy of the solution. These issues were resolved by developing a stabilized FE framework that incorporates backflow stabilization for Neumann outlet boundaries; a consistent flux boundary condition that minimally disturbs the local physics of the problem; and front-capturing stabilization to regularize solutions in high Pe number flows. The efficacy of these formulations was investigated for both idealized and patient-specific geometries.

Next, a flexible arbitrary reaction-advection-diffusion (ARAD) interface was implemented that enables prototyping nonlinear biochemical models of thrombin generation. After verifying the ARAD interface, the performance was compared against the original hardcoded FORTRAN implementation for speed and accuracy using a 4-scalar nonlinear reaction model of thrombosis[103]. Three different biochemical models of thrombin generation were investigated in idealized geometries. Finally, we implemented the 18 scalar model in both idealized and patient-specific geometries to determine the effects of complex 3D hemodynamics on thrombin generation.

The computational framework for thrombosis initiation presented in this work has three key features: *i)* non-Newtonian hemodynamics; *ii)* a stabilized numerical framework for scalar RAD problems; and *iii)* a method to rapidly prototype custom reaction models using

Python with negligible associated computational expense.

CHAPTER I

Introduction

1.1 Epidemiology of Thrombosis

Thrombosis is the process of a blood clot, also known as a thrombus, forming in a blood vessel. Thromboembolic conditions, a combination of thrombosis and embolism (blockage of an artery), have been estimated to account for 1 in 4 deaths worldwide in 2010[144]. Thrombosis is the common mechanism of all thromboembolic conditions including myocardial infarction (MI), ischemic stroke, and venous thromboembolism (VTE)[85]. Thrombosis can be broadly classified as either venous thrombosis or arterial thrombosis, according to where the thrombus presents in the body. The leading forms of arterial thrombosis are ischemic heart disease and ischemic stroke, while venous thromboembolism leads to deep-vein thrombosis (DVT) and pulmonary embolism (PE)[144]. Although different in their origin and presentation, both arterial and venous thrombosis are a large burden to both the health care system and the patients they affect.

1.1.1 Arterial Thrombosis

Arterial thrombosis refers to a blood clot forming in one of the major arteries and often coincides with the incidence of a buildup of cholesterol plaque in the walls of the arteries, known as atherosclerosis[68]. The combination of these two diseases is referred to as atherothrombotic disease. Ischemic heart disease (coronary artery disease), stroke, and atrial fibrillation are three groups of arterial diseases all fundamentally linked to arterial thrombosis[144].

In recent years there has been an increase in death and years of life lost (YLL) from ischemic heart disease and ischemic stroke[85], both of which can be attributed to arterial thrombosis. Coronary artery thrombus occurs due to the rupture or erosion of a preexisting coronary artery plaque formed via atherosclerosis, resulting in the artery's complete occlusion, ischemic heart disease, and ultimately myocardial infarction (death of heart tissue)[72]. Coronary thrombus can occur in both symptomatic and asymptomatic patients with significant or less than 50% degree of stenosis and is one of the frequent causes of sudden cardiac death[31,136].

Ischemic stroke is a thrombotic condition similar to ischemic heart disease. Instead of the blood clot or thrombosis blocking blood flow to the heart, the obstruction in circulation is now to the brain[144]. Approximately 85% of all strokes are ischemic stroke because of thromboembolism, and 15% are hemorrhagic stroke[144].

Lastly, atrial fibrillation is an irregular and often rapid heart rate that can increase the risk of strokes, heart failure and other heart-related complications by predisposing the affected patient to thrombus formation and cardioembolism[144]. Atrial fibrillation is a leading preventable cause of ischemic stroke[2] and is associated with a four- to five-fold increased risk of ischemic stroke[124].

Overall, arterial thrombosis presents as a broad disease that can affect multiple organs and regions of the body. Often present with an associated disease such as atherosclerosis or atrial fibrillation, atherothrombotic diseases are responsible for $> 25\%$ of all deaths worldwide[3].

1.1.2 Venous Thrombosis

Venous diseases are typically regarded as long-term disabilities lacking the immediate, fatal consequences associated with arterial diseases. Nevertheless, conditions such as DVT and PE affect an important part of the population and represent a large burden for the health care system. The direct annual cost of VTE events to the US healthcare system alone is seven-ten billion dollars for $375,000-425,000$ newly diagnosed VTE cases[56]. The indirect cost of treatment is also high; six million days of work are lost in the United States because of complications due to chronic venous insufficiency[142]. Furthermore, patients' quality of life is often diminished by the loss of workdays and frequent doctor or nursing visits[126]. Studies have shown that an estimated five to eight percent of the world population suffers from venous disease, and in the United States alone there are approximately five million cases of DVT each year[46,132]. DVT is typically treated through a combination of blood thinners, internal filters, and/or surgical removal. These procedures can be highly invasive and have severe side effects, including hemorrhaging[91]. For this reason it is fundamental to broaden our understanding of this complex disease.

1.2 Thrombus Formation

The factors that contribute to thrombosis can be summarized by Virchow's Triad (Figure 1.1), which describes three broad categories. Alone or in combination, hemodynamics, endothelial damage, and the hypercoagulability of blood all directly contribute to the formation of thrombosis. Thrombosis formation is comprised of two major interacting parts, platelet aggregation and coagulation. These two processes work both independently and together to form a blood clot.

1.2.1 Coagulation Cascade

The coagulation cascade is a series of complex biochemical processes that change blood from a liquid to a gel and results in the formation of a blood clot (thrombus). Enzymes or proteins known as clotting factors and referred to by Roman numerals, see Figure 1.2, undergo a series of nonlinear biochemical reactions to produce the key enzyme thrombin (Factor IIa). Thrombin serves a crucial role in the coagulation cascade by cleaving the polymer fibrinogen into fibrin strands that result in the formation of a "fibrin mesh"[141].

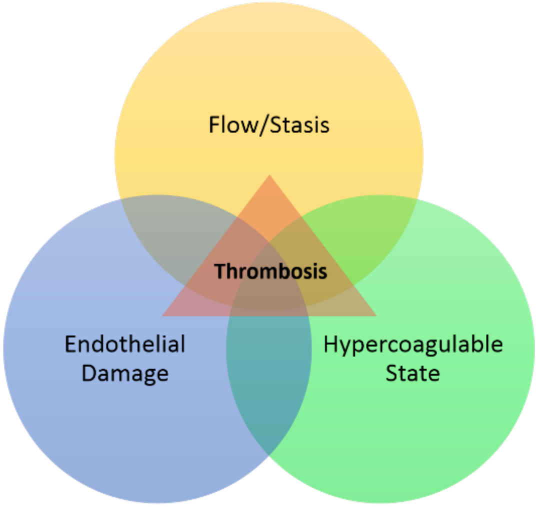

Figure 1.1: Virchow's Triad.

In the process of clotting, many erythrocytes, platelets, and other cells are trapped in the fibrin meshwork formed from fibrinogen. Previous *in vitro* studies have shown the thrombin concentration present during clot formation determines the eventual fibrin structure[148].

The coagulation cascade is comprised of three pathways: extrinsic, intrinsic, and common, see Figure 1.2. The division of the coagulation cascade originates from laboratory tests in which clotting times were measured after the clotting was initiated by glass (or by thromboplastin which is a mixture of tissue factor and phospholipids). Two laboratory tests that are used commonly to evaluate blood coagulation are: Prothrombin Time (PT) which measures the integrity of the extrinsic system and Partial Thromboplastin Time (PTT) which measures the integrity of the intrinsic system.

The extrinsic system, the principle initiating pathway of *in vivo* blood coagulation, involves both blood and vascular elements[89]. The critical component is tissue factor (TF), a glycoprotein embedded in the subendothelium of the vessel wall as well as in various other cells (i.e. leukocytes)[89]. Under physiologic conditions, tissue factor is covered by healthy endothelial cells and is not exposed to blood. When vascular injury occurs due to various reasons (piercing, shear stress, vessel wall weakening etc.) TF becomes exposed and acts in concert with activated Factor VIIa and phospholipid initiate the coagulation cascade and form thrombin.

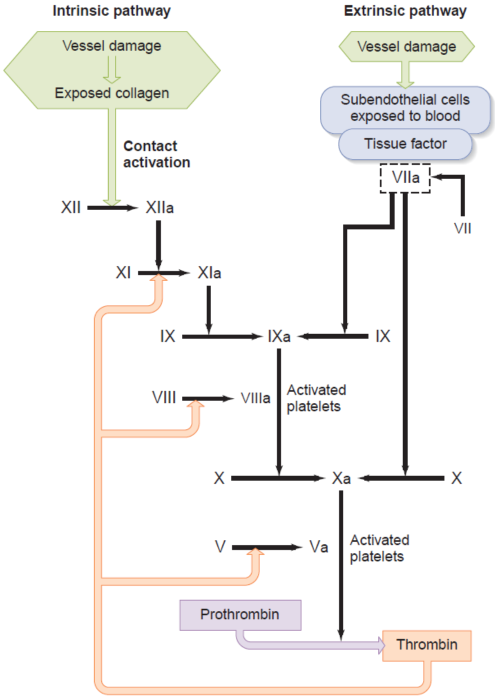

Figure 1.2: Coagulation Cascade[146].

Early reactions in coagulation produce catalysts, known as enzymes, which speed up the rates of other reactions and allow for clotting to occur in a feasible time span. At the same time that the coagulation cascade creates the fibrin mesh, the fibrinolytic system breaks down the fibrin meshwork via the enzyme plasmin. These reactions typically remain in a well-balanced state. In the absence of this balance, clotting disorders occur including thrombosis.

Overall, the coagulation cascade is a complex system of biochemical reactions that results in the formation of a blood clot via thrombin formation and is closely tied to platelet activation and aggregation.

1.2.2 Platelet Aggregation

Platelets are small cells fragments, two to three microns in size, that play an active role in both hemostatic and pathological thrombosis[34]. At a resting state platelets are small disc-like cell fragments that are advected throughout blood. When endothelial damage occurs, platelets come into contact with exposed collagen and von Willebrand factor (VWF), becoming activated. Once activated, platelets change their shape and unveil projections and receptors that allow them to bind to one another and to clotting factors[152]. Once activated platelets adhere to both each other and the vessel's wall to form what is known as platelet plug. In the case of an injury, this prevents more blood from leaving the body as well as prevents any outside contaminants from entering the body.

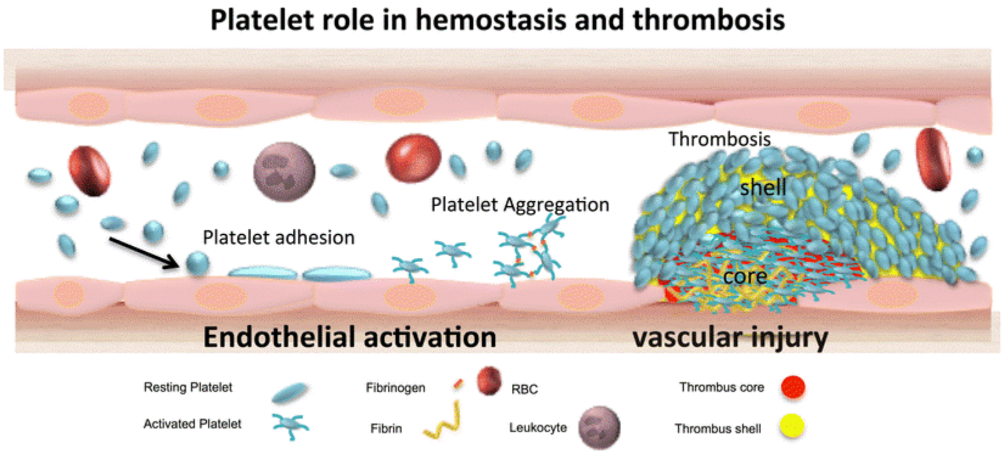

Figure 1.3: Platelet Activation. Taken from M. Holinstat, 2017[63].

Platelets, also serve an important role in the coagulation cascade, in addition to forming a platelet plug. Once activated, platelets display specific plasma membrane receptors that bind several of the clotting factors, and this permits the reactions to take place on the surface of the platelets. The activated platelets also display certain phospholipids, called platelet factors, which function as a cofactor in the steps mediated by the bound clotting factors. After the initial generation of small concentrations of thrombin via the coagulation cascade, thrombin serves an important stimulator of platelet activation and works through positive feedback to activate additional platelets which in turn allow more clotting factors to be activated on their surface.

1.2.2.1 Mechanical Activation of Platelets

It has been previously recognized that platelet activation in the presence of high shear-rate flows contributes to the formation of arterial thrombi. Von Willebrand factor (VWF), the largest protein found in plasma, is involved in hemostasis[53]. VWF has a multimer structure, where each monomer of VWF contains an A1 domain that is capable of binding to the platelet receptor GP-Ib[153]. Through this binding process VWF is able to initiate platelet activation. Typically, at rest VWF does not induce thrombosis because VWF is present in its globular form where platelets are not able to reach the A1 binding sites. In pathophysiologic cases of increased shear rate globular VWF unravels into an elongated form and exposes its A1 binding sites. Therefore, critically high shear rates are capable of inducing platelet activation and promoting thrombosis formation. The value of critical shear rate at which the unfolding of VWF occurs is thought to be between $1000 - 10000$ s^{-1}[153]. The mechanism of VWF induced platelet activation serves as an explanation for the increased rate of thrombosis in arterial geometries where high shear is present, for example aortic stenoses[10].

1.2.3 Hemodynamic Metrics of Thrombosis

Various hemodynamic metrics have been linked to thrombosis formation. Endothelial cells play a large role in the prevention of thrombosis by shielding the blood from TF and collagen, two prothrombotic substances. Various hemodynamic stimuli have been linked to endothelial cell gene expression that leads to either pro-atherosclerotic or pro-thrombogenic phenotypes. For example, both low Wall Shear Stress (WSS) and high oscillatory flow have been correlated to endothelial activation[36]. Biasetti et al. studied how vortex formation and shedding resulting from complex aneurysmal flow leads not only to the activation but the convection, and deposition of platelets distal to the original location[16].

Hemodynamics is also strongly linked to venous thrombosis formation where stasis is one of the leading risk factors in venous thrombosis formation[44], particularly in the venous valve sinus. Endothelial cells that line the venous valve sinus and adjacent valve leaflet exhibit high expression of antithrombotic phenotype, characterized by low levels of prothrombotic proteins (i.e. VWF, P-selectin, ICAM1, etc.) thrombotic inhibitors such as tissue factor pathway inhibitor (TFPI)[143]. The loss of this antithrombotic phenotype in the endothelial cells lining the venous valves is observed following venous stasis[143].

1.3 Computational Models of Thrombosis

Computational models of blood flow are useful tools for gaining insight into the physical behavior of the cardiovascular system in healthy and diseased states. Computational models have advanced to the point that they have been used for surgical planning, medical device design, and drug development.

Computational models can be used to understand the complex mechanisms intertwined in thrombosis initiation such as hemodynamics, biochemistry, and cell dynamics. Among its many advantages, computational modeling provides high spatial and temporal resolution descriptions on metrics which often cannot be measured in humans, such as Walls Shear Stress (WSS), blood velocity and pressure, and the concentration of various coagulation factors. Computational models can help build intuition to interpret clinically available results. The methods used to model thrombosis initiation range from biochemically complex reduced order models of thrombin generation that do not take into account blood flow, to full 3D formulations of image-based geometries and hemodynamics with simple descriptions of the biochemical reactions. In this work we develop a robust, data-driven computational framework that combines imaged-based modeling, non-Newtonian hemodynamics, a stabilized scalar mass formulation, and a complex description of coagulation biochemistry. The framework was implemented within the cardiovascular hemodynamic modeling environment CRIMSON (crimson.software)[6]. We employed this framework to study thrombosis initiation in both idealized and patient-specific geometries and investigate how complex 3D hemodynamics affects thrombin generation and transport in image-based geometries.

1.4 Modeling Non-Newtonian Rheology in the Cardiovascular System

Blood is a heterogeneous multi-phase mixture composed of cells and cell fragments (erythrocytes, leukocytes, and thrombocytes) suspended in blood plasma which is an aqueous solution of proteins, organic molecules and minerals. The viscosity of a fluid (blood) can be viewed as an internal friction that resists flow. It is defined as a ratio of shear stress to shear rate[76]:

$$\text{viscosity} = \frac{\text{shear stress}}{\text{shear rate}} \tag{1.1}$$

Blood has been described as a non-Newtonian fluid, in which viscosity is a function of the shear rate and exhibits a large range of viscosities based on its complex composition of cells suspended in fluid. The non-Newtonian behavior of blood is largely due to the presence of erythrocytes, or red blood cells (RBCs). RBCs are solid but pliable and aggregate to form three-dimensional cell clusters and one-dimensional "rouleaux" stacks[93]. High shear rates disrupt RBC aggregates and deform RBCs to align better with flow and reduce drag. Therefore, the effective viscosity of blood decreases with increasing shear rates until reaching an asymptotic value for shear rates $> 100\text{s}^{-1}$.[9]

The viscosity of blood is nearly constant and independent of shear rate in large vessels with high blood velocity, such as arteries. Here, the shear rate of blood is too high ($> 100\text{s}^{-1}$) for RBC rouleaux formation to occur. In these vessels, blood can be approximated as a Newtonian fluid with constant viscosity. However, in vessels with low shear rates and/or recirculation such as diseased arteries and veins, viscosity increases as shear rate declines due to the presence of RBC aggregates[9]. This behavior is known as "shear-thinning", see Figure 1.4.

Two of the most known and used shear-thinning models are the Power Law and the

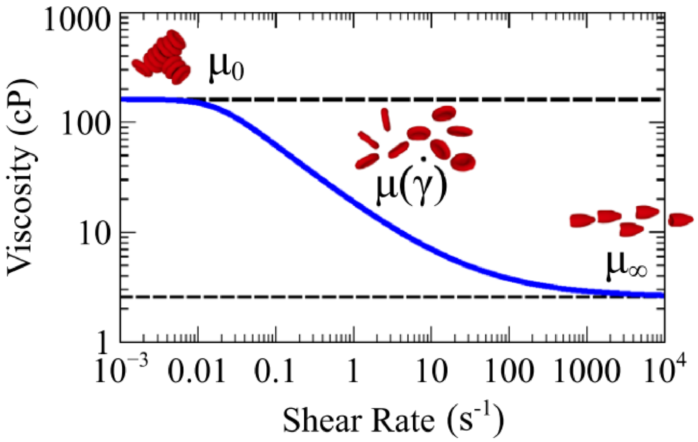

Figure 1.4: Shear rate–viscosity curve for blood with RBC disaggregation and deformation illustrated. Adapted from Aycock et al.[9].

Carreau-Yasuda[67,88]. The Power Law or Ostwald-de Waele Power Law model describes non-Newtonian viscosity as a function that is proportional to the shear rate raised to a power, n:

$$\mu(\dot{\gamma}) = \delta \dot{\gamma}^{n-1} \tag{1.2}$$

Where n and μ_0 are coefficients fit from experimental data. Values of n greater than 1 indicate shear thickening, less than one shear thinning, and equal to 1 indicates Newtonian viscosity (i.e. Poiseuille flow). The Power-Law model begins to fail at both very high and very low shear rates; where the estimated tends to infinity rather than reaching a constant value as observed experimentally[115]. The Carreau-Yasuda model was developed to remedy these problems, offering superior flexibility to fit experimental data. This model is defined as:

$$\mu(\dot{\gamma}) = \mu_\infty + (\mu_0 - \mu_\infty)\left(1 + (\lambda\dot{\gamma})^a\right)^{\frac{n-1}{a}} \tag{1.3}$$

Where n, μ_0, μ_∞, a, and λ are parameters that can be fit from experimental data. Here μ_0 is the zero-shear-rate viscosity, μ_∞ is the infinite-shear-rate viscosity, λ is a time constant for the fluid, n is a power-law-like exponent, and a is a dimensionless parameter. The advantage of the Carreau-Yasuda model is that it can fit most viscosity data over a wide range of shear rates, at the expense of the large number of material parameters. Figure 1.5 provides a comparison between these two non-Newtonian models as well as the Newtonian assumption.

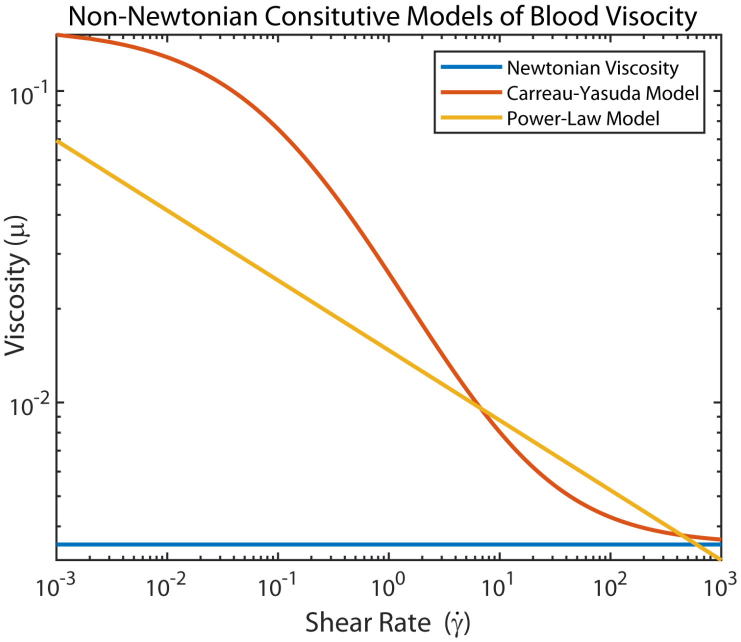

Figure 1.5: Constitutive equations of blood rheology. Newtonian models (blue line), Power-Law model (yellow line), and Carreau-Yasuda model (orange line).

Modeling efforts of both venous or complex arterial hemodynamics should account for this nonlinear dependence between viscosity and shear rate. We aim to incorporate established non-Newtonian constitutive models of blood in our group's Finite Element modeling software CRIMSON[6].

1.4.1 Numerical Challenges of Computational Thrombosis Models

Computational models provide key insights into quantities that are often not possible to measure *in vitro* or *in vivo* and have potential for unveiling key mechanics of thrombosis initiation. To create realistic models of thrombosis initiation that are some key challenges that must first be addressed. Modeling thrombosis via mass transport in cardiovascular systems presents numerical challenges due to: the inherently complex and time-dependent flow patterns and vessel geometries; the large Péclet numbers that arise due to the extremely small diffusivity of platelets and clotting factors; the complex nonlinear reaction models involved in thrombin generation; and the disparities in time scales between cardiac cycles and the coagulation cascade.

1.4.1.1 RAD Problems in Transient Flow

From previous literature it is apparent that transient 3D cardiovascular hemodynamics affects thrombus formation[16,36]. Retrograde flow is often induced during flow deceleration in parts of the cardiovascular system and may persist throughout the cardiac cycle. To model thrombin formation and therefore mass transport in imaged based non-Newtonian models it is necessary to solve the scalar reaction-advection-diffusion equations under conditions of transient flow.

Previous work on scalar transport under flow has been limited to investigations with complex scalar phenomena with relatively simple flow fields[81] or relatively complex flow fields with physiologically inaccurate boundary conditions. For example, previous studies have typically used an assumption of steady parabolic flow which is not true for many sites of disease progression. Furthermore, this assumption negates the effects that complex hemodynamics has on disease initiation and progression[36].

Other researcher groups have gone a step further and formulated innovative models of scalar transport that also include image-based geometries and transient cardiovascular flows. These investigations[8,57] have relied exclusively on Dirichlet mass transport boundary conditions prescribed on outlet faces. While numerically this assumption is valid, biologically an assumption of a set scalar value (typically prescribed to be 0) at an arbitrary point in space is non-physiologic and can affect the conclusions drawn from the aforementioned studies. Alternatively, Neumann boundary conditions, although more physiologically accurate, are known to lead to numerical divergence in boundaries exhibiting partial or complete flow reversal[51,74,97]. It is therefore necessary to develop and implement methods that allow for numerically stable solutions in the presence of backflow at outlets as this is a common phenomena of cardiovascular flows.

1.4.1.2 Consistent Flux Boundary Condition

Arguably the most challenging aspect of numerical modeling is the choice of realistic boundary conditions. Often times researchers employ the use of elongated geometries to ensure that the area of interest is ‘far enough away’ from the boundary to avoid artificial boundary effects. This is an extremely computational expensive task. In thrombosis modeling computational expense becomes a limiting factors as clotting occurs on the order of minutes and often in very large and/or complex geometries. Therefore, developing physiologically relevant boundary conditions that allow for the truncation of large domains is essential to accurately modeling thrombosis. To mitigate this issue it is necessary to develop and implement boundary conditions that maintain the accuracy and reliability of the computed solution without increasing computational cost.

While there have been numerous contributions proposing outflow boundary conditions for cardiovascular flow problems (i.e. the Navier-Stokes equations)[135], little work has been done for the scalar reaction-advection-diffusion problem. Typically, cardiovascular mass transport models have employed either Dirichlet or Neumann conditions prescribing known scalar concentrations[8,57] or diffusive fluxes[81,151] at an outlet face, respectively. An alternative choice of boundary condition, henceforth referred to as “consistent boundary condition” has been shown to provide better error estimates[55]. This approach relies on calculating the consistent diffusive flux (rather than imposing an arbitrary diffusive flux) that satisfies the weak form of the mass transport equation.

1.4.1.3 Stabilization Techniques

The numerical complexity of thrombosis modeling is further compounded by the extremely low diffusivities of clotting factors and platelets which are on the order of 10^{-10} $\mathrm{m}^2 s$[49,81,149]. The Péclet number, is a non-dimensional parameter, that describes the relative role of advective and diffusive transport and is defined as

$$Pe = \frac{Lu}{D}, \tag{1.4}$$

where L is the characteristic length, u the local flow velocity, D the mass diffusion coefficient. Péclet numbers can vary greatly throughout the cardiovascular system based on the size of the vessel, velocity field (i.e. stenosis or diseased flow), and the diffusivity of the species of interest. High Péclet numbers lead to the formation of steep concentration gradients within the flow, causing the presence of spurious oscillations in the numerical solution. In mass transport, and particularly in computational models of thrombosis, due to the low diffusivities and high velocity fields, Péclet numbers can be on the order of $\mathcal{O}(10^8)$. Previous investigations have addressed the numerical challenges associated with high Pe number flows by either limiting their investigation to relatively simple flows (i.e. steady flow without sharp gradients) in over simplified geometries (i.e. cylinder, idealized geometries)[16,96], using unrealistic physical parameters (i.e. artificially increased diffusivities)[16,50], or using inconsistent stabilization methods (i.e. isotropic diffusion)[16] to circumvent the need for these robust and consistent stabilization methods.

To create a numerically accurate and reliable computational model of thrombosis it is necessary to use appropriate stabilization methods to address the presence of spurious oscillations at high Péclet numbers that allow for solving the scalar reaction-advection-diffusion equations in realistic 3D geometries with complex flows.

1.4.2 Flexible Reaction Models

Although the main application of interest in this work is thrombosis initiation, RAD equations can be applied to study numerous biochemical diseases such as atherosclerosis, cholesterol metabolism and lipid-lowering drugs, among others. Furthermore, it is common to focus on a subsection of the coagulation cascade, such as the intrinsic or extrinsic pathway, to investigate a specific biological question. Therefore, there is a need to develop a flexible computational framework that enables rapidly prototype nonlinear reaction models within a stabilized fluid-RAD framework. Until now the majority of thrombosis models have either been hardcoded using in-house codes[81] or implemented in commercialized software[16] that does not offer the flexibility of customized models. In addition, many previous coagulation models have ignored the effects of complex 3D hemodynamics altogether. There remains a need to develop a stabilized 3D models of thrombosis initiation that allows the flexible and rapid prototyping of nonlinear reaction models.

1.4.3 Previous Computational Models of Thrombosis

Various groups have used computational models to investigate thrombus formation. Previous computational models of thrombosis initiation have focused on reduced-order models (0D) that provide a detailed description of the biochemistry of thrombin formation in the absence of flow. Attempts at modeling thrombin formation under flow has been limited to using idealized 3D geometries or 2D models with broad simplifications to the hemodynamics. Currently, few groups have attempted to model thrombosis initiation incorporating image-based 3D geometries, complex hemodynamics, and the complex biochemistry that describes thrombin generation. The development of such a model will be vital to improve our understanding of the role of hemodynamics in thrombus formation.

1.4.3.1 Reduced Order Models

Hockin and Mann developed a mathematical model of blood coagulation that accounts for the biochemical reactions involved in the extrinsic blood coagulation system and includes the stoichiometric anticoagulants TFPI and antithrombin[61]. The model consists of 34 differential equations with 44 rate constants that together describe the 27 independent equilibrium expressions and account for the 34 species[61]. The model simulates an injured state via an initial nonzero value of tissue factor (TF). The initiation of the biochemical cascade leads to the formation of thrombin and a blood clot. This model ignores the influence of platelets, binding sites, and flow. Instead the model assumes a closed, static zero-dimensional system with an infinite amount of lipids present for the coagulation reactions to occur.

Sagar et al.[123] developed a reduced-order model for thrombin generation using a hybrid strategy combining ordinary differential equations (ODEs) and logical rules to model thrombin dynamics. The model shows good performance for thrombin dynamics, but ignores key clotting factors such as Factor V and Factor X. Arumugam et al.[7] proposed a model focused on the interactions between thrombin and antithrombin III with greater connection to the coagulation biochemistry, but failed to include the effect of platelets. Papadopoulos et al.[103] suggested a four-species phenomenological model for thrombin dynamics. The reactions have been shown to match patient specific thrombin generation curves and include dynamics of thrombin, prothrombin, platelets, and activated platelets.

1.4.3.2 Continuum Models of Thrombosis

Leiderman and Fogelson developed a computational model of thrombosis that builds upon Hockin and Mann's description to include fluid dynamics[81] along with platelets and binding sites for clotting factors on platelets in a two-dimensional geometry of an arteriole. The Navier-Stokes equations were combined with the enzymatic equations to create a reaction-advection-diffusion model of thrombus initiation. This model provided key information in regards to diseases such as hemophilia. The strengths of this model are its detailed description of the biochemistry of thrombin formation, biologically informed description of platelet-plug formation, and two-way coupling between flow and the platelet-plug. This model is limited by its simplified hemodynamics including an idealized geometry, steady flow and Newtonian viscosity.

Biasetti et al. described the formation of intraluminal thrombus in abdominal aortic aneurysms (AAAs). In their first investigation they studied the effects of non-Newtonian viscosity in an image-based computational model of an AAA[15]. Subsequently, they implemented their non-Newtonian model in an idealized, axisymmetric, 2D model of an AAA with a biochemical model of blood coagulation[16]. The strengths of this model include: non-Newtonian viscosity and complex enzyme kinematics. However, their thrombosis model was implemented in an idealized 2D geometry that ignores the complex hemodynamic effects resulting from 3D image-based geometries. In addition, the model does not account for the effects of inhibitors such as tissue factor pathway inhibitor (TFPI) and antithrombin-III (AT-III) which were included in the Hockin-Mann model[61]. These inhibitors directly impact the amount of thrombin formed and the time to peak thrombin formation[61]. Furthermore, instead of using physiologic values of diffusivity, Biasetti et al. increased the diffusion coefficients used by over two orders of magnitude to avoid numerical oscillations. This was discussed in more detail in Section 1.4.1.

Three dimensional continuum models of thrombus formation exist in the literature. A hemodynamics-based thrombosis model was developed by Menichini and Xu in 2016[96] and later modified by Menichini et al.[94] and used to investigate lumen thrombosis in aortic dissections following thoracic endovascular repair[95]. This thrombosis model relies on a phenomenological approach of modeling platelet deposition and tracking the concentration of an arbitrary coagulation. Specifically, transport equations for fluid residence time, resting and activated platelets, and an arbitrary coagulant, are solved for approximately 20 cardiac cycles with transient hemodynamics. Here, a growing thrombus is identified through the local concentration of bound platelets. This model is strengthened by its 3D non-Newtonian hemodynamics, but it is limited by the phenomenological approach to modeling thrombosis formation.

Seo et al.[127] developed a 3D model of thrombosis initiation in infarcted left ventricles using the same thrombosis model as Biasetti et al[16]. This 3D model solves for the reaction, advection, and diffusion of 18 scalar species throughout the computational domain. In addition, this study includes a model of the polymerization of the fibrinogen and platelet activation and aggregation. This investigation is strengthened by its complex and biologically relevant biochemical model but is limited by the use of Newtonian viscosity. In addition, simulations were only run for 6 cardiac cycles which is not long enough to capture thrombin formation which occurs on the order of minutes.

The reduced order developed by Papadopoulos et al. was later implemented in a 3D flow model using Newtonian viscosity[104]. To account for the disparity in time scales between a cardiac cycle and the coagulation process a simplified inflow pulse consisting of 9 time instances of the original cardiac pulse was used. This allowed the transport simulations to be run for multiple minutes of physical time. This investigation is again limited by the simplified inflow and phenomenological coagulation model.

Lastly Bodnár and Sequeira developed a Finite Volume Method model of thrombosis initiation and fibrinolysis using a non-Newtonian description of blood flow and a set of twenty-three coupled advection, diffusion, and reaction equations describing the extrinsic pathway of the blood coagulation process and fibrinolysis in quiescent plasma. This model also uses realistic values of diffusion and is strengthened by its complex and accurate biochemical description. This model is limited by its simplified hemodynamic description: simulations are done in an idealized cylinder with steady parabolic flow conditions.

1.4.3.3 Lagrangian Computational Thrombosis Models

The Humphrey group has studied intraluminal thrombus in AAAs in depth. In particular, they have developed a predictor of platelet activation and therefore thrombus formation in

AAAs known as the Platelet Activation Potential (PLAP)[36]. PLAP is a non-dimensional scalar index that represents the magnitude of shear rates that a fluid particle accumulates while traveling through the fluid domain and is defined as:

$$PLAP(\mathbf{x}, t) = \int_{t-2T}^{t} |\mathbf{D}(\mathbf{x}(\tau), \tau)| d\tau, \tag{1.5}$$

where $|\mathbf{D}(\mathbf{x}(\tau), \tau)|$ is the Frobenius norm of the symmetric part of the spatial gradient of the velocity tensor, t is the time of injection of the particle and $2T$ indicates how long the particle has been tracked.

To compute PLAP, after solving for a periodic flow solution, a number of massless tracer particles with prescribed initial positions are released and their Lagrangian trajectories in the Eulerian flow field are integrated using a fourth-order Runge-Kutta scheme. This Lagrangian tracking metric of 'platelet activation potential' has been linked to thrombus formation in thoracic (Figure 1.6) and abdominal aortic flows[36,98]. We remark that owing to the discrete size of the integration time step, a small percentage of particles are erroneously lost through the wall boundaries.

This predictor is physics driven but entirely phenomenological, as it is separated from the biological complexity of the biochemistry of thrombus formation. The production of thrombin is not modeled directly, and mechanical platelet activation is the only stimulus considered, ignoring the influence of clotting factors and inflammation. A more complex and biologically relevant predictor of thrombus formation is necessary to fully describe thrombus potential.

Overall, although several groups have developed computational models of thrombus formation, these have been focused on idealized 1D and 2D geometries, 3D geometries with simplified assumptions made to the flow field, and/or simplified phenomenological description of the coagulation cascade (i.e. thrombin formation). Currently, no model exists to

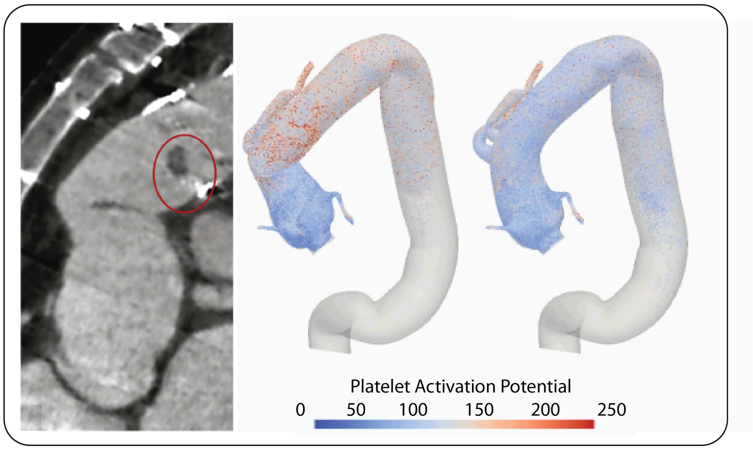

Figure 1.6: (Left) Computed tomography imaging showing the aortic thrombus (red circle). (Right) Simulation of PLAP, a metric generated via Lagrangian advection of large quantities of massless particles. PLAP calculates the history of accumulated shear in each particle. Simulations correspond to two surgical reconstructions of a patient. The CT insert reveals the location of a thrombus which roughly coincides with the predicted region of high PLAP (Actual Surgery)[98]

study thrombosis in a three-dimensional setting that characterizes coagulation in the larger vessels where both venous and arterial thrombosis naturally occurs. Therefore, we propose to develop an image-based computational model of thrombosis initiation. Our model will be the first to include image-based geometries with transient cardiovascular flow, non-linear viscosity, and a complex description of the enzymatic reactions involved in thrombin formation.

1.5 Structure of Thesis

In this work, we first implemented non-Newtonian rheological models into CRIMSON in order to develop an accurate representative of the hemodynamics across the range of physiological shear rates, from arterial to venous (Chapter II). We next developed a stabilized numerical framework of scalar mass transport in CRIMSON to enable the analysis of advection-diffusion transport problems under conditions of cardiovascular hemodynamics and applied the framework to further investigate non-Newtonian viscosity on mass transport. This involved both contributions to boundary conditions as well as numerical stabilization

(Chapter III). After the implementation of non-Newtonian hemodynamics and a stabilized numerical framework scalar mass transport we turned our attention to implementing nonlinear reaction models of thrombosis initiation (Chapter IV). Lastly, we presented preliminary work involving possible mechanisms of venous thrombosis formation in patients with May-Thurner syndrome (Chapter V) and preliminary work applying our mass transport framework to different clinical applications (Chapter VI). The general Discussion of this thesis is presented in Chapter VII. Chapters II, III and IV correspond to journal articles that are either in print or under preparation. The format of the papers has been adjusted to match the rest of the thesis with minimal changes to the content.

CHAPTER II

Effects of non-Newtonian Viscosity on Arterial and Venous Flows

2.1 Introduction

Despite significant progress in clinical research and care, cardiovascular diseases remain the leading cause of death and disability worldwide[92]. Advances in both experimental and computational modeling techniques have led to an improved understanding of basic mechanisms underlying various cardiovascular diseases. In particular, numerous studies have implicated altered local hemodynamic metrics (e.g., vorticity, wall shear stress (WSS), etc.) in the initiation and progression of thrombosis and atherosclerosis[15,36,80]. Moreover, anatomical features such as aneurysms trigger complex local flow patterns, which lead to increases in residence time of biochemical species[118,138]. Therefore, computational models for cardiovascular disease research must account for the altered hemodynamics in image-based geometric models, specifically in recirculation areas likely to experience complex transport phenomena.

An important aspect of a computational model is the constitutive assumption. Blood has been shown to exhibit shear-thinning behavior and has been described via various shear-dependent constitutive models such as the Carreau-Yasuda and Power-Law models[17]. Nevertheless, most computational hemodynamics studies have treated blood as a Newtonian fluid with uniform viscosity[40,129,133]. The use of a Newtonian assumption for blood is typically justified for large arteries with high shear rate flows. However, this assumption is questionable in regions exhibiting low shear rates and local flow recirculation such as aneurysmal vessels and veins. Therefore, it is crucial to incorporate shear rate dependent blood rheology for accurately describing the local hemodynamics in such cases.

Several studies have investigated the effects of non-Newtonian viscosity in diseased arterial models. While some studies concluded that considering the shear thinning behavior of blood is significant[15,28,140], others reported relatively minor differences in hemodynamics[112]. With regards to venous flows, most studies considered a Newtonian assumption for blood[83,119], and only a few contributions considered non-Newtonian behavior[9], albeit under idealized (constant) flow conditions.

In this work, we aimed to increase our understanding of the impact of blood rheology on complex arterial and venous flows, with significant regions of low shear rates. Towards that end, we implemented a Power-Law and Carreau-Yasuda model in the cardiovascular hemodynamics modeling environment CRIMSON[6]. In addition to exploring the impact of constitutive models on traditional hemodynamic metrics such as velocity and wall shear stress, we aimed to examine other metrics such as Lagrangian indices of accumulated shear.

The structure of this Chapter is as follows. In the Materials and Methods, an overview of governing equations, constitutive models, and Lagrangian particle tracking is provided. In the Results section, the implementation of the Power-Law model is first verified in an idealized cylindrical geometry against an analytical solution. Next, the effects of non-Newtonian rheology (using the Carreau-Yasuda model) are investigated in two representative three-dimensional, transient, image-based scenarios: (a) a thoracic aortic aneurysm model, and (b) a venous model of the inferior vena cava and iliac bifurcation. In each case, differences between in-plane velocity, vorticity, WSS, and Lagrangian indices of shear between the Newtonian and Carreau-Yasuda models are studied in detail.

2.2 Materials and Methods

2.2.1 Fluid Dynamics

2.2.1.1 Governing Equations

The strong form of the governing equations for an incompressible fluid in a three-dimensional bounded domain $\Omega \subset \mathbf{R}^3$ is given as

$$\rho\left(\frac{\partial \mathbf{u}}{\partial t} + \mathbf{u}\cdot\nabla\mathbf{u}\right) = -\nabla p + \nabla\cdot\tau(\mathbf{u}) + \mathbf{f}, \tag{2.1}$$

$$\nabla\cdot\mathbf{u} = 0, \tag{2.2}$$

where ρ is the fluid density, t is the time, $\mathbf{u}$ is the fluid velocity, p is pressure, $\mathbf{f}$ is the external body force per unit volume (set to zero), and τ is the viscous stress tensor. For a Newtonian, incompressible fluid, τ is defined as:

$$\tau = 2\mu\mathbf{D}, \tag{2.3}$$

where μ is the Newtonian viscosity and $\mathbf{D}$ is the rate of deformation tensor defined as:

$$\mathbf{D} := \frac{\left(\nabla\mathbf{u} + \nabla\mathbf{u}^T\right)}{2}. \tag{2.4}$$

For a non-Newtonian fluid τ can be written as:

$$\tau = 2\mu_{\text{eff}}(\dot{\gamma})\mathbf{D}, \tag{2.5}$$

where $\dot{\gamma}$ refers to the shear rate defined as

$$\dot{\gamma} = \sqrt{2\mathbf{D}:\mathbf{D}}, \tag{2.6}$$

and $\mu_{\text{eff}}(\dot{\gamma})$ is the constitutive shear rate function which describes the effective viscosity in terms of $\dot{\gamma}$.

2.2.1.2 Constitutive Models of non-Newtonian Viscosity

Various constitutive models have been developed and calibrated against experimental data to describe the shear-thinning behavior of blood. Table 2.1 presents the three constitutive models considered in this study and their associated parameter values, chosen from previous reports[1,15–17]: (a) Newtonian model, (b) Power-Law model, and (c) Carreau-Yasuda model. The Newtonian fluid model employs a constant, shear-independent viscosity (μ_{N}). In contrast, the Power-Law fluid model employs two constants, a flow consistency index δ, and a flow behavior index n, to model the shear dependent blood viscosity. Lastly, the Carreau-Yasuda model employs five coefficients: λ, a relaxation time, power indices n and a, and asymptotic values of the effective viscosity $\mu(\dot{\gamma})$, μ_0 and μ_∞, at zero and infinite shear-rates, respectively.

Constitutive Models	**Form**	**Parameter Values**
Newtonian	$\mu(\dot{\gamma}) = \mu_{\text{N}}$	$\mu_{\text{N}} = 0.0035$
Power-Law	$\mu(\dot{\gamma}) = \delta \dot{\gamma}^{n-1}$	$\delta = 0.0147,\ n = 0.7755$
Carreau-Yasuda	$\mu(\dot{\gamma}) = \mu_\infty + (\mu_0 - \mu_\infty)\left(1 + (\lambda\dot{\gamma})^a\right)^{\frac{n-1}{a}}$	$\mu_\infty = 0.0035,\ \mu_0 = 0.16$ $\lambda = 8.2,\ n = 0.2128$ $a = 0.64$

Table 2.1: Constitutive Models used in this investigation.

Figure 2.1 shows the viscosity-shear rate relationship for the three constitutive models and parameter values considered in this study. The Power-Law model displays a linear response with a constant slope given by the flow behavior index n on a log–log scale. Values of $n > 1$ imply shear thickening behavior while values of $n < 1$ imply shear-thinning behavior. Conversely, the Carreau-Yasuda model is characterized by constant values of viscosity in both the low (μ_0) and high (μ_∞) shear-rate limits. Between these limits, the viscosity varies in a nonlinear manner on the log-log scale.

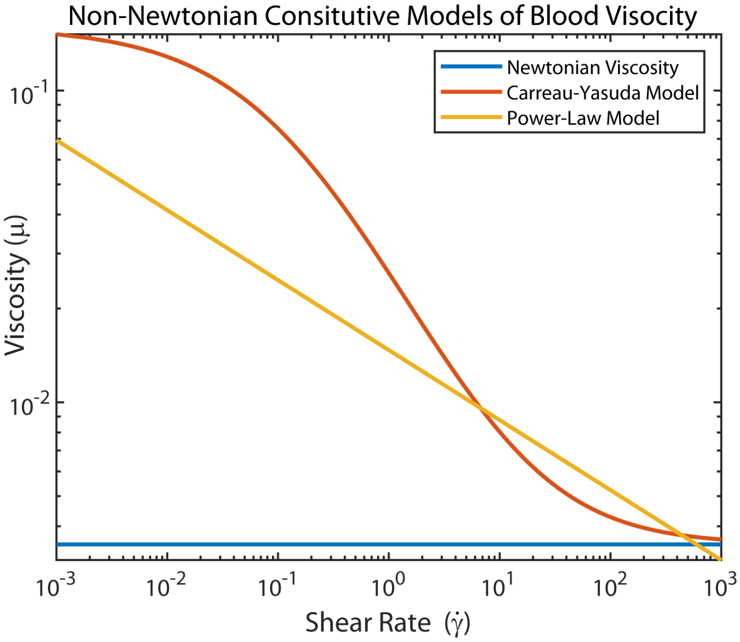

Figure 2.1: Constitutive Models

In this study the Power-Law model and its analytical solution were used to verify our implementation of shear-dependent, non-Newtonian viscosity. For all patient-specific analyses, we employed the Carreau-Yasuda model since it has been shown to better represent the *in vivo* behavior of blood over a wider range of shear rates[139].

2.2.2 Lagrangian Particle Tracking

A significant goal of this work is to understand the impact of non-Newtonian rheology on transport phenomena. Towards that goal, we considered an approach to assess Lagrangian transport within a given flow field.

The Navier-Stokes equations are typically solved in fixed Eulerian formulations. Consequently, the solution fields (velocity and pressure) do not directly provide insights on the path of particles traversing through the flow. Conversely, a Lagrangian representation of a flow field can be used to describe the path, history of hemodynamic stresses, and residence time experienced by a particle in certain parts of the vasculature. In blood flow, constituents such as platelets are small enough in size that can be reasonably approximated by massless particles advected by the flow. The path and the history of stress of these particles are important quantities to study processes such as platelet mechanical activation, a key process in thrombus formation[10,36]. Therefore, in this work we considered a Lagrangian particle tracking method derived from the Eulerian solution fields to assess the cumulative shear experienced by massless particles[36,128]. Specifically, we introduced a number of particles with prescribed initial positions and integrated their Lagrangian trajectories from the Eulerian flow field solution using a fourth-order Runge-Kutta scheme. This Lagrangian tracking allowed us to assess the 'platelet activation potential' (PLAP), a metric that has been linked to thrombus formation in thoracic and abdominal aortic flows[36,98]. PLAP is a non-dimensional scalar index that represents the magnitude of shear rates that a particle accumulates while traveling through the fluid domain and is defined as

$$PLAP(\mathbf{x},t) = \int\limits_{t-T}^{t} |\mathbf{D}(\mathbf{x}(\tau),\tau)| d\tau, \tag{2.7}$$

where $|\mathbf{D}(\mathbf{x}(\tau),\tau)|$ is the Frobenius norm of the symmetric part of the spatial gradient of the velocity tensor, t is the current time, and T indicates how long the particle has been tracked.

2.2.3 Patient-Specific Models and Boundary Conditions

Two patient-specific geometries were considered: a thoracic aortic aneurysm model, and a venous model of the inferior vena cava and iliac veins. To ensure a consistent comparison between the Newtonian and Carreau-Yasuda models, the parameter values listed in Table 2.1 were adopted. Specifically, the parameter μ_∞ was chosen to match the Newtonian viscosity ($\mu_\infty = \mu_{\mathrm{N}} = 0.0035$ Pa $\cdot$ s)[90]. Therefore, both the Newtonian and Carreau-Yasuda models yield the same effective viscosity in the high shear rate limit. At low shear rates, the Newtonian model exhibits lower viscosity. Blood density was 1060 kg/m^3 for both models.

2.2.3.1 Arterial Model

A patient-specific thoracic aortic aneurysm model was generated from computed tomography angiography (CTA) image data using CRIMSON[6]. Figure 2.2 (left panel) shows the computational domain, consisting of the ascending and proximal descending aorta and nine outlet branches, and a schematic of the boundary conditions. An echocardiography-derived periodic flow waveform (time period $T = 0.91\,\mathrm{s}$) was mapped to a parabolic velocity profile, and prescribed as the inflow condition at the inlet face of the aortic model. Three-element Windkessel models[135] were prescribed at the outlet faces (Table A.1)[133]. A zero velocity boundary condition was prescribed on all walls.

Several meshes with increasing levels of refinement were considered. A mesh with 22 million linear tetrahedral elements and 3.9 million nodes was ultimately chosen to adequately capture flow recirculation in the aneurysmal region. Cycle-to-cycle periodicity was achieved after four cardiac cycles.

2.2.3.2 Venous Model

A patient-specific venous model was generated from CTA image data using CRIMSON[6]. Figure 2.2 (right panel) shows the computational domain, consisting of the inferior vena cava (IVC) and left and right common, internal, and external iliac veins (CIV, IIV, EIV), and a schematic of the boundary conditions. The venous geometry was scaled to match literature diameters values of the IVC and iliac veins.

Measurements of velocity were obtained at the IVC, common, and external iliac veins using duplex Doppler ultrasonography. Average flow values were calculated based on the mean velocity and diameter values obtained from the CTA. Internal iliac vein flows were deduced from the difference between the common and external iliac flows. A period of $T = 0.8\,\mathrm{s}$ was utilized for all waveforms, which were mapped to a parabolic velocity profiles prescribed at the four inlet vessel faces of the model (e.g., external and internal iliac veins). A three-element Windkessel model was applied to the IVC outlet face (Table A.2). A zero

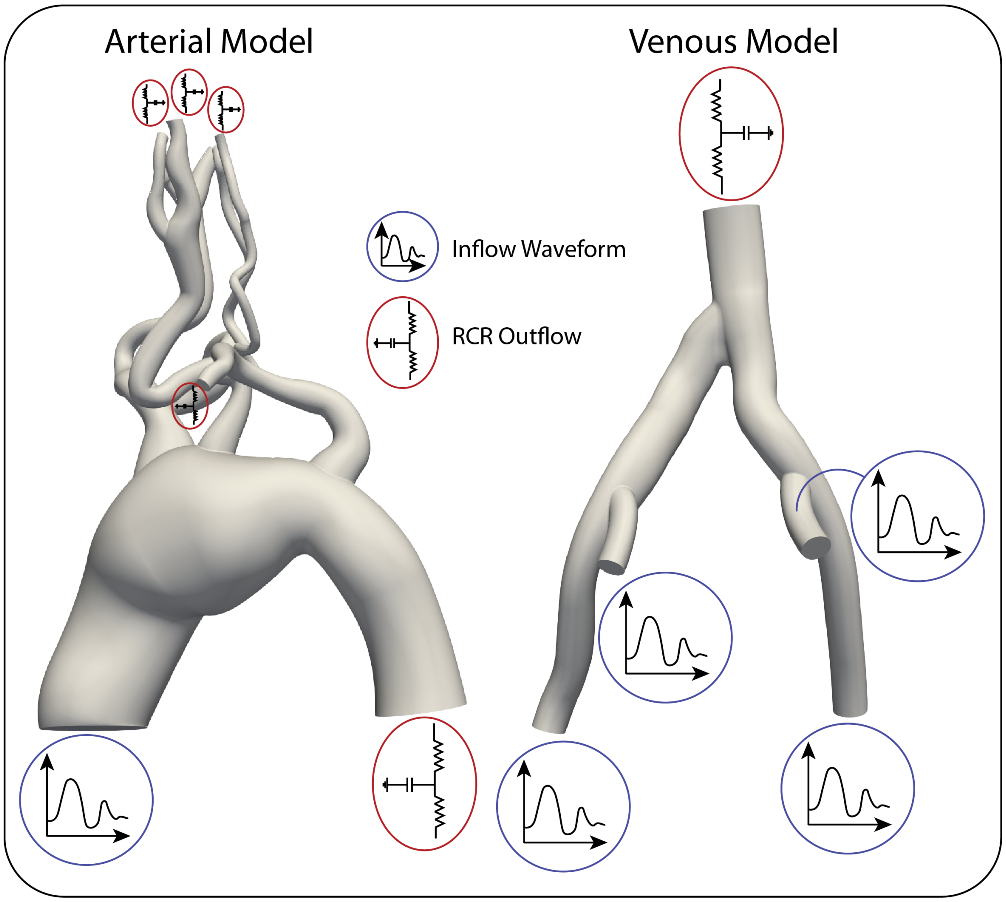

Figure 2.2: Computational domains of the patient-specific arterial model (Left) and venous model (Right). Inflow and outlet boundary conditions are specie as either a prescribed inflow waveform or reduced order Windkessel model.

velocity boundary condition was prescribed on all walls.

Several meshes with increasing levels of refinement were considered. Reported results correspond to a mesh consisting of 2 million nodes and 12.5 million linear tetrahedral elements. Cycle-to-cycle periodicity was achieved after four cardiac cycles.

2.3 Results

2.3.1 Verification of Power-Law Implementation

We considered a cylindrical domain with diameter $d = 40.0$ mm and length $l = 200.0$ mm. Using a Power-Law constitutive model, a steady flow solution was obtained by prescribing a constant flow rate of 833.33 mm^3/s mapped to a Poiseuillle parabolic velocity profile at the inlet, with a maximum centerline velocity v_{max} = 1.3 mm/s and a mean Reynold's number Re_{mean} = 4.0. No-slip and zero traction boundary conditions were prescribed on the lateral wall and the outlet face, respectively.

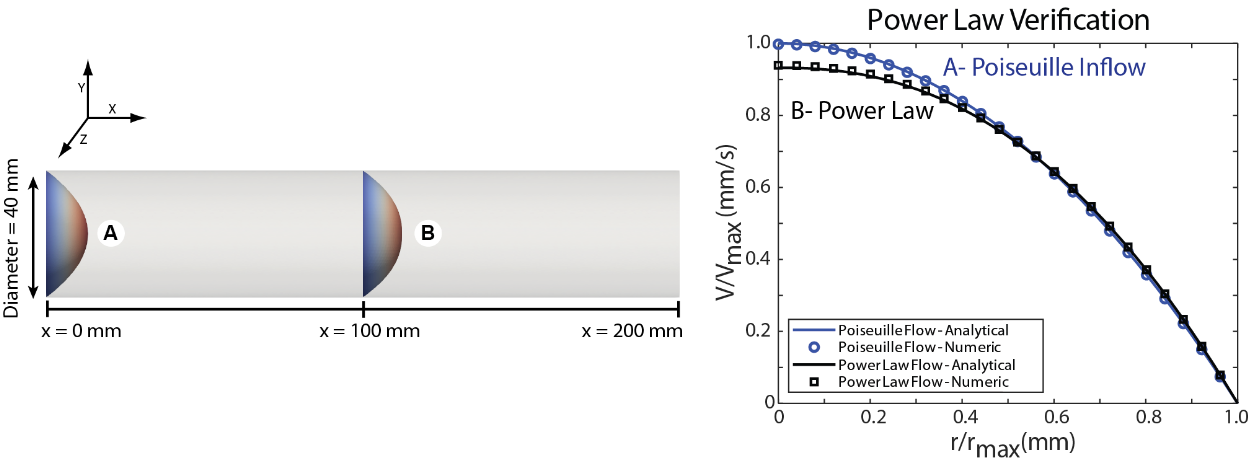

Figure 2.3: Verification of a Power-law model. Left: Cylinder dimensions. The prescribed Poiseuille profile at the inlet (A) develops into a non-Newtonian Power-Law velocity profile at the mid-section of the cylinder (B). 1D plots show good agreement between analytical (black solid line) and numerical (black symbols) solutions at section B (max. error: 0.72%).

Figure 2.3(A) shows 3D warps of the prescribed velocity profile at the inlet (section A) and the numerically obtained velocity profile at the midplane of the domain (section B). Figure 2.3(B) compares the analytical and numerical solution at these two locations. The prescribed Poiseuille profile at the inlet (blue circles) develops into a non-Newtonian profile along the length of the cylinder, and by its mid-section (black solid symbols) shows an excellent agreement (max. error: 0.72%) with the Power-law analytical solution (black solid line).

2.3.2 Patient-Specific Hemodynamic Analysis

In this section, diastolic solutions for velocity, vorticity, and WSS are discussed for both the Newtonian and Carreau-Yasuda constitutive laws, for the arterial and venous models. Vorticity is defined as the curl of the velocity field ($\omega = \nabla \times \mathbf{u}$) and describes the local spinning motion of the fluid. To provide a quantitative comparison between solutions, surface (in-plane velocity and WSS) or volume (vorticity) averages of the solution fields are calculated at four locations: mid-aneurysm (section A) and distal aorta (section B) for the aortic model, and IVC (section C) and left common iliac vein (section D) for the venous model. Furthermore, to study the differences between solutions on a point by point basis, we define a relative difference metric as:

$$\text{Relative Difference} = \frac{\|\text{Newtonian - Carreau Yasuda}\|}{\overline{\|\text{Carreau Yasuda}\|}}, \tag{2.8}$$

where $\|\|$ is the L2 norm of the solution field, and $\overline{\|\quad\|}$ is a reference mean value of the Carreau-Yasuda solution, calculated for each slice of the in-place velocity, and for the shaded regions in the ascending aorta and IVC for the vorticity and WSS (see Figures 2.5 and 2.6). This reference mean value defines a suitable norm to study relative differences for each solution field between Newtonian and Carreau-Yasuda models[36].

2.3.2.1 In-Plane Velocity

Figure 2.4 shows contour plots of the in-plane velocity magnitude and bar plots of mean in-plane velocity. In the arterial model, larger mean values of in-plane velocities are observed in the Newtonian model, with larger discrepancies between models seen in Section B (Section A: 10.6% and Section B: 70.3%). Larger relative differences in in-plane velocity magnitude are also observed in section B with relative differences of up to 7.5. In the venous model, similar patterns are observed: larger mean in-plane velocities are obtained with the Newtonian model (Section C: 56.2% and Section D: 15.5%), and larger relative differences in in-plane velocity magnitude are seen in Section C. (Max. Relative Difference 2). Due to the smaller pulsatility and lower flow in the venous model, smaller values of in-plane velocity are obtained (max. in-plane velocity 27 mm/s) relative to the arterial model (max. in-plane velocity 175 mm/s).

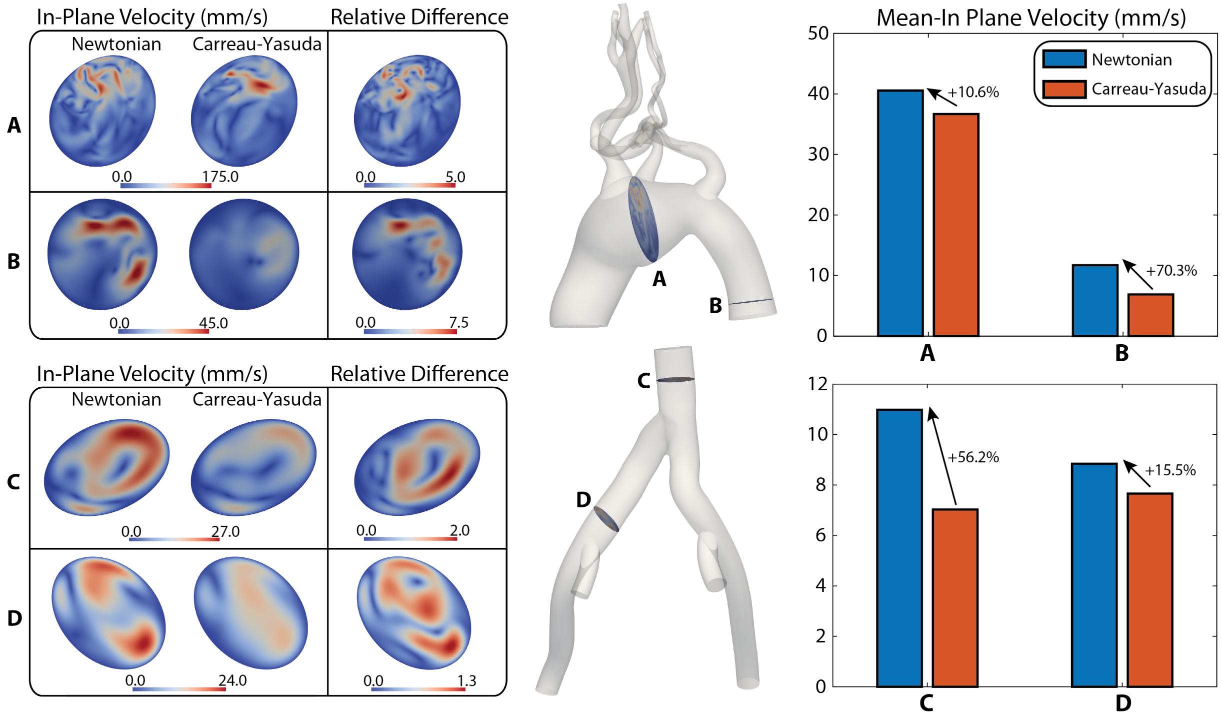

Figure 2.4: Arterial and venous in-plane velocity in diastole. (Left) Contour plots of in-plane velocity magnitude for the Newtonian and Carreau-Yasuda models, and relative difference between the two, at four representative locations. (Right) Bar plots of mean values for each location.

2.3.2.2 Vorticity

Figure 2.5 shows volume rendering plots of vorticity magnitude and bar plots of mean vorticity. More vortical structures are apparent in the Newtonian solution for both the arterial and venous models, with a maximum relative difference of 3.0 in the arterial and 1.0 in the venous model. Mean vorticity is larger in all four locations for the Newtonian model, ranging from 10.5% in the IVC (Section C) to 36.9% in the descending aorta (Section B). Due to the lower pulsatility of the venous flow, smaller values of vorticity are obtained in the venous model (max. vorticity 30 s^{-1}) relative to the arterial model (max. vorticity 50 s^{-1}).

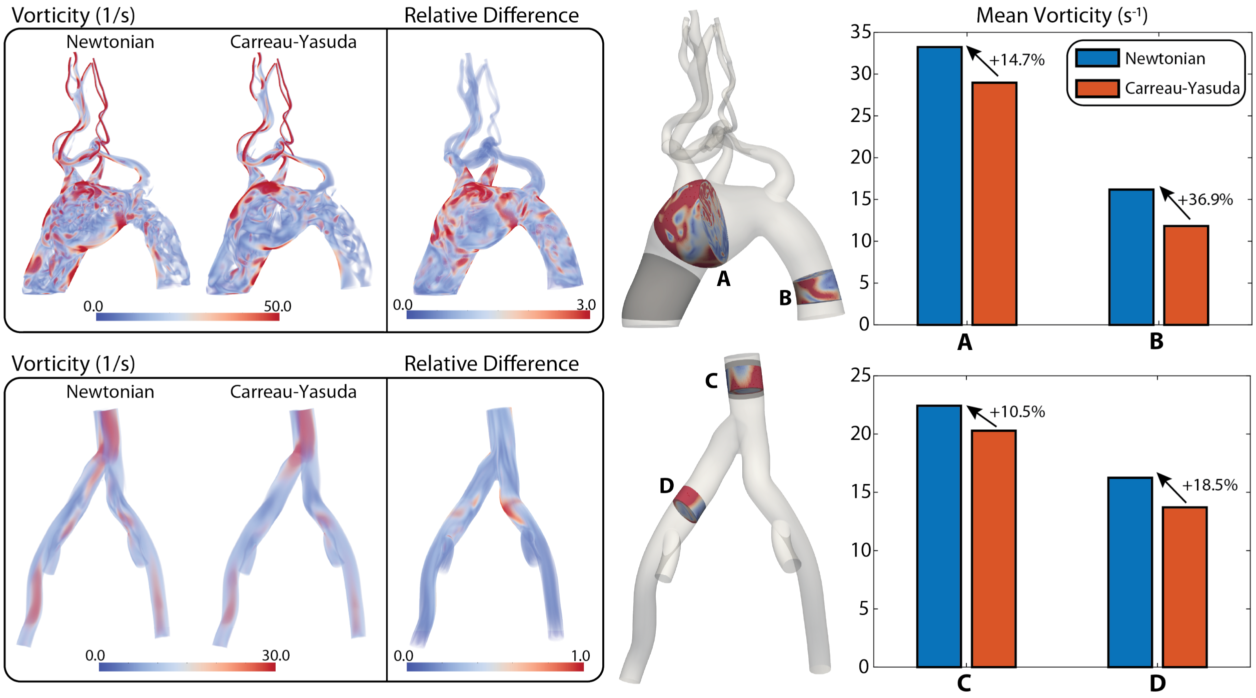

Figure 2.5: Arterial and venous vorticity in diastole. (Left) Volume rendering plots of vorticity magnitude for the Newtonian and Carreau-Yasuda models, and relative difference between the two. (Right) Bar plots of mean values for four representative locations (A-D).

2.3.2.3 Wall Shear Stress

Figure 2.6 shows contour plots of WSS magnitude and bar plots of mean WSS. In the arterial model, mean WSS is smaller in the Newtonian solution (18.4% smaller in the mid-aneurysm and 7.0% smaller in the descending aorta) in both the aneurysm and descending thoracic aorta. For the venous model, smaller values of WSS are also obtained with the Newtonian solution (26.4% smaller in the IVC and 25.6% smaller in the left common iliac vein). Larger relative differences are observed in the arterial model (2.0 for the arterial model vs. 0.6 for the venous model). Due to the smaller pulsatility of the venous flow, smaller values of WSS are obtained in the venous model (max. WSS 0.10 Pa) relative to the arterial model (max. WSS 0.50 Pa).

We remark that the reported trends in in-plane velocity, vorticity, and WSS are consistent

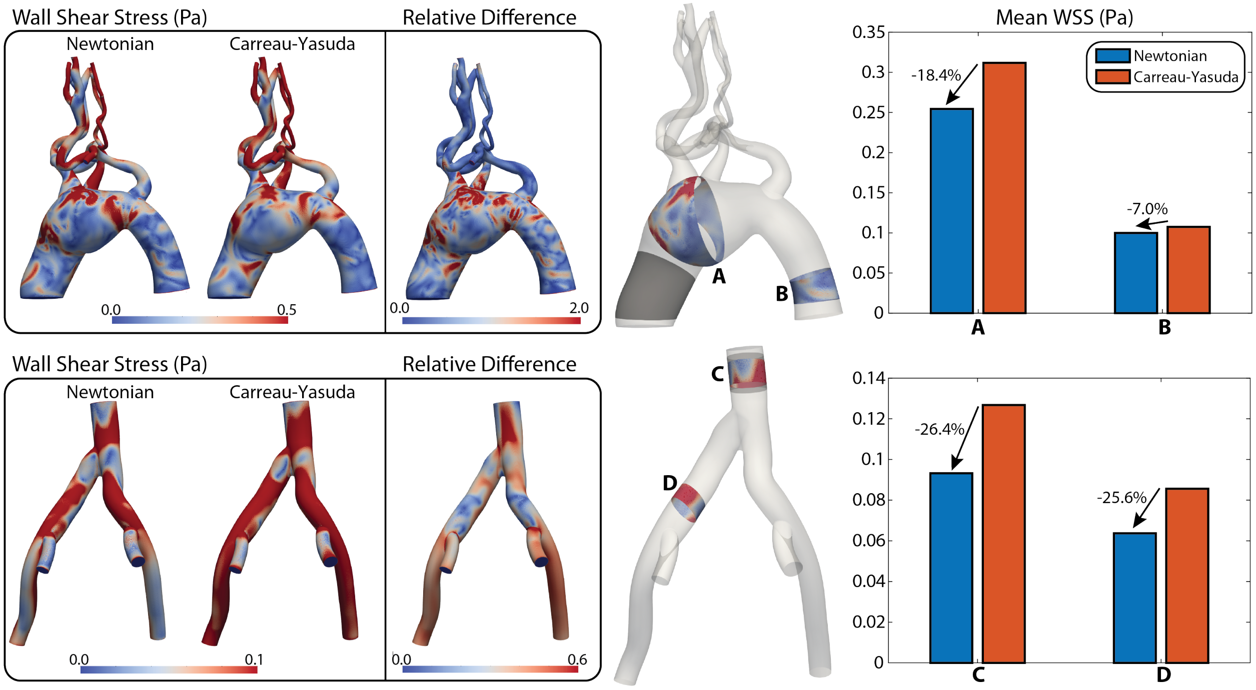

Figure 2.6: Arterial and venous WSS in diastole. (Left) Contour plots of WSS magnitude for the Newtonian and Carreau-Yasuda models, and relative difference between the two. (Right) Bar plots of mean values for four representative locations (A-D).

throughout the cardiac cycle for each model, and not just in diastole.

2.3.2.4 Regions of Critical Shear Rate

Lastly, regions of high viscosity and low shear rate in the Carreau-Yasuda model are identified through an arbitrary threshold of viscosity: ($\mu \geq \mu_{\text{critical}} = 0.01\,\text{Pa.s} = 3\mu_{\text{N}}$), see Figure 2.7, for both the arterial and venous models in diastole. These are the regions where the non-Newtonian effects are most important.

A few areas of increased viscosity can be identified in the aneurysmal and descending aortic regions, as well as in the head and neck vessels of the aortic model. In contrast, the venous model shows extensive regions of elevated viscosity and low shear rate throughout the entire model, except in the near wall regions. In the arterial model, regions of low shear rate

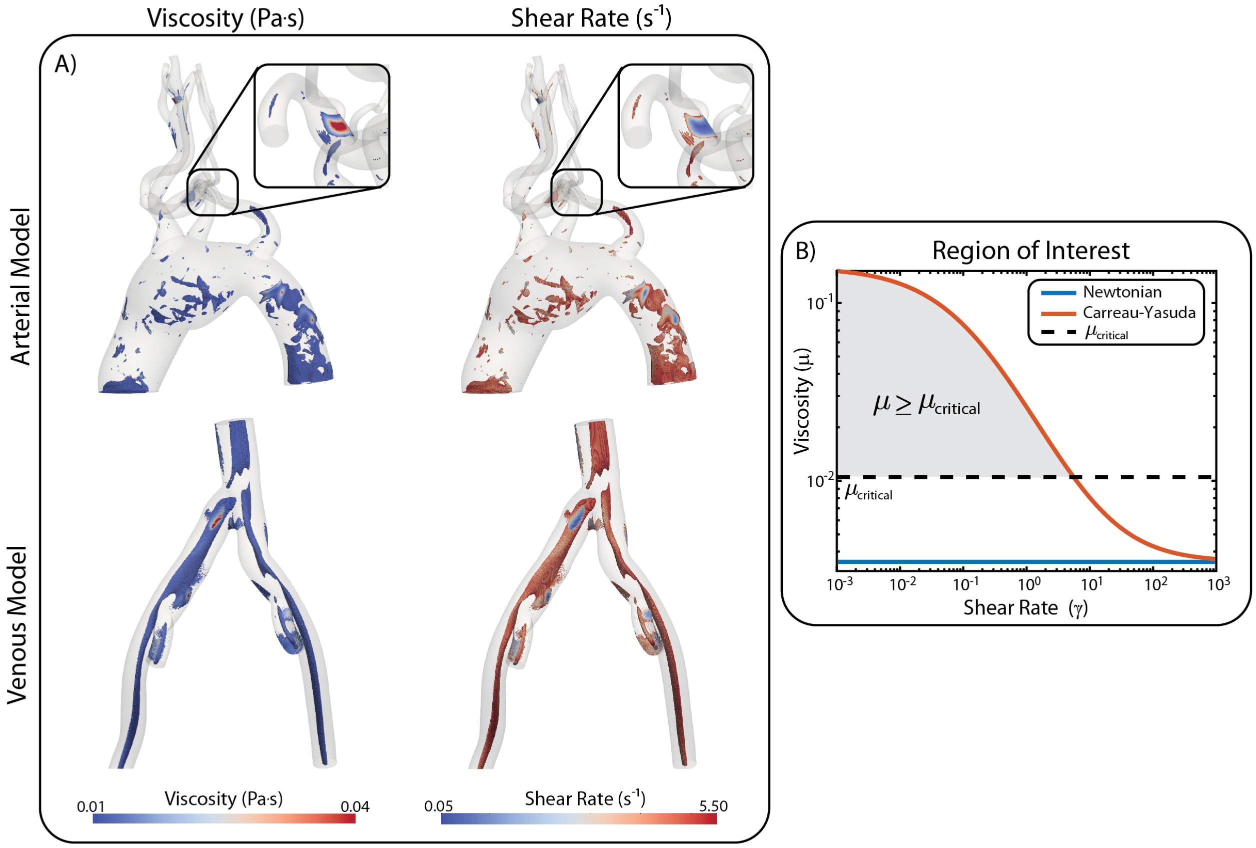

Figure 2.7: (A) Maps of viscosity and shear rate obtained with the Carreau-Yasuda model in the regions of the computational domain where the viscosity is greater than the critical threshold ($\mu \geq \mu_{\text{critical}}$). These are regions where the non-Newtonian effects are most important. (B) Critical viscosity is defined by $\mu_{\text{critical}} = 3 * \mu_{\text{N}}$.

are expected in the aneurysmal region, but it is interesting to also observe those regions in the descending aorta, where the aortic diameter is normal. In the venous model, widespread areas of low shear rate emphasize the need to consider non-Newtonian viscosity models when studying problems on the large veins.

2.3.3 Lagrangian Transport Analysis

The transport of biochemical species such as proteins, platelets and chemical signaling species plays a significant role in the initiation and propagation of various cardiovascular diseases such as thrombosis and atherosclerosis[16,60,130]. We next investigate the effect of viscosity models on Lagrangian transport in the patient-specific models.

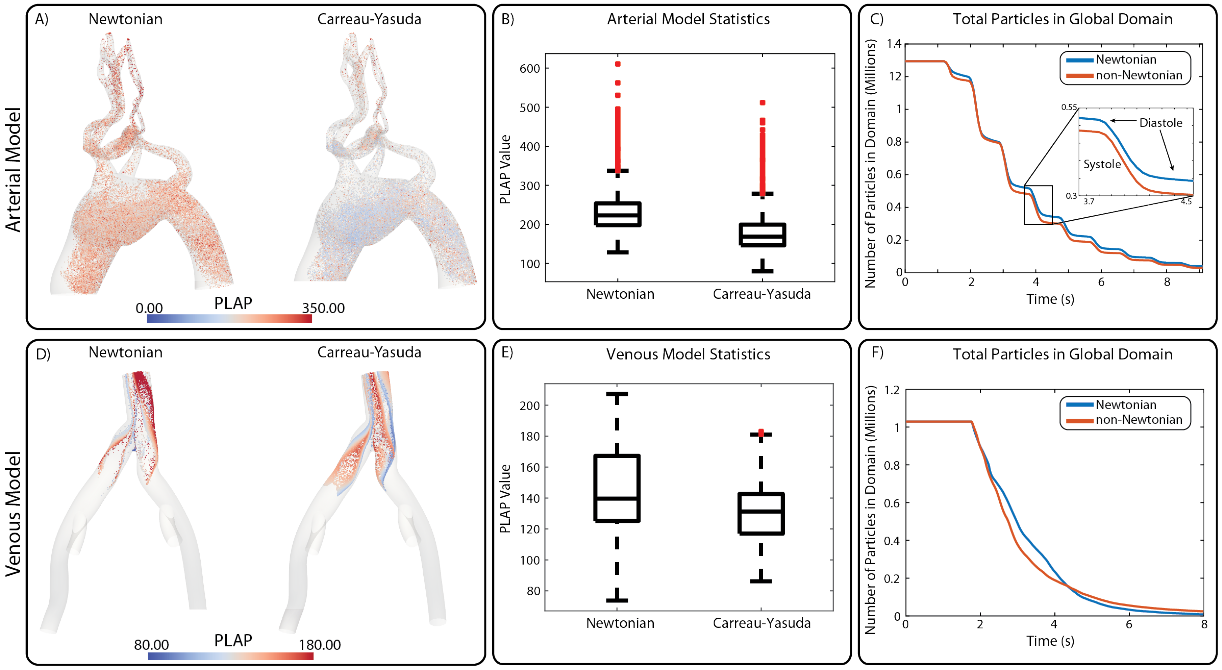

Figure 2.8: (A,D) Particles left in the arterial and venous computational domains for Newtonian and Carreau-Yasuda simulations. (B,E) Box and whisker plot describing the particles left in the domains. (C,F) Line plots describing the number of particles leaving the computational domains over time.

Approximately one million massless particles were injected into the arterial and venous anatomical models and tracked for ten cardiac cycles. For the arterial model, a single bolus was released at the ascending thoracic aorta. In the venous model, four boluses of approximately 250,000 particles each were released at the left EIV, left IIV, right EIV, and right IIV. Particles were tracked as they were passively advected through each computational domain over time and collected at the outflow faces. Statistics on PLAP and the number of particles were recorded.

	Mean PLAP Newtonian	**Mean PLAP Carreau-Yasuda**
Arterial	229.1	177.1
Venous	146.7	130.7

Table 2.2: Mean values of PLAP for the particles left in the arterial and venous domains after ten cardiac cycles.

Figure 2.8(A,D) shows the particles remaining in the arterial and venous models after ten cardiac cycles. Mean PLAP values in both models are larger in the Newtonian analysis compared to the Carreau-Yasuda, see Figure 2.8(B,E) and Table 2.2.

Figure 2.8(C,F) show the total number of particles inside the anatomical domains over time. Particles leave the domains at different rates due to differences in viscosity. Interestingly, particles leave the domains at a slower rate in the Newtonian model. This is likely due to the increased vorticity of the flow in the Newtonian simulation, see Figure 2.5. The pulsatility of the arterial flow is apparent in panel C, where we observe that non-Newtonian viscosity is more important during diastole (flat portions of the curve). After $t = 3.64$ s, the differences between Newtonian and Carreau-Yasuda simulations are apparent throughout the entire cardiac cycle. For the venous model (panel F), particles leave the domain at a relatively constant rate due to the smaller pulsatility of the flow.

2.4 Discussion

Despite the long-standing knowledge of the shear thinning behavior of blood, computational studies have typically assumed a shear-independent Newtonian viscosity model for blood. While this assumption is generally applicable in large arteries characterized by high shear rates, it is difficult to justify in regions of vasculature exhibiting low shear rates such as veins and diseased arteries. Moreover, previous studies which considered non-Newtonian viscosity models often employed idealized vascular geometries, despite the evident role that complex anatomical features have in altered flow patterns[39,125,140]. In this work, we set out to investigate the impact that the choice of constitutive model has on hemodynamic metrics (velocity, vorticity, wall shear stress) as well as Lagrangian transport metrics for arterial and venous anatomies in which low shear and recirculation are expected.

We first implemented two shear-dependent non-Newtonian viscosity models of blood, the Power-Law and Carreau-Yasuda model. To test our implementation of shear-dependent viscosity, we compared the results of the Power-Law model in an idealized cylindrical vessel against the Power-Law analytical solution, obtaining excellent agreement between profiles (Figure 2.3). Our implementation was explicit (e.g., we only accounted for shear-dependent viscosity on the right-hand-side residual and not the left-hand-side linearization matrix). This explicit implementation of shear-dependent viscosity led to minor increments in computational cost compared to solutions obtained with a Newtonian model.

We then studied the effect of blood rheology in two patient-specific models which are expected to exhibit regions of low shear rate: a thoracic aortic aneurysm model, and a venous model of the IVC and iliac veins, see Figure 2.2. In each case, we performed a comparative hemodynamics and transport analysis using Newtonian and Carreau-Yasuda viscosity models.

For the arterial model, our analysis of hemodynamic indices revealed lower in-plane velocities and vorticity and larger WSS in the Carreau-Yasuda solution, see Figures 2.4, 2.5, and 2.6. Lower vorticity in the Carreau-Yasuda solution is expected since non-Newtonian models are characterized by higher viscosity and lower shear rates that result in larger diffusion on the flow vorticity. In the Carreau-Yasuda solution, the viscosity is sufficiently large to result in greater WSS.

The venous model was characterized by lower pulsatility and velocities compared to the arterial model. Our analysis again revealed lower velocities and vorticity (Figures 2.4 and 2.5) and larger WSS (Figure 2.6) in the non-Newtonian case. This observation suggests that the increased viscosity in the non-Newtonian case is sufficiently larger to result in higher WSS, despite the lower velocity gradients.

A Lagrangian particle tracking analysis was then performed in both the arterial and venous models to assess the effect of blood rheology on cardiovascular transport (Figure 2.8). A particle tracking technique was used where massless tracer particles were introduced and tracked as they traverse through the computational domain. This analysis allows us to calculate a metric of accumulated shear termed ‘platelet activation potential’ (PLAP). Our analysis revealed an increase in mean PLAP in the Newtonian case for both the arterial and venous models (Figure 2.8(B,E)). In addition, non-Newtonian viscosity affected the rate at which particles left the computational domain with particles leaving at a slower rate in the Newtonian case (Figure 2.8(C,F)). We hypothesize that this is caused by the increased vorticity (see bar plots in Figure 2.5) which led to particles recirculating longer before exiting the domain. Residence time and PLAP are two metrics that have both been linked to thrombosis formation[94,98] and this suggests that considering accurate blood rheological models can have a significant effect on solutions for computational cardiovascular disease models.

One of the primary limitations of the current study is that both the arterial and venous walls were modeled as rigid. However, owing to the limited availability of vessel wall material properties and their regional variation, such a study demands a separate focused effort and will be the subject of future work.

In this study, we used previously reported values of viscosities in the low and high shear rate limit for the Carreau-Yasuda model. However, there exist numerous other computational studies[11,120,139] that employed different values, making it difficult to compare results across studies. Therefore, better standardization and computational benchmarks are needed, perhaps in idealized geometries, to allow both the validation of new computational frameworks and the study of isolated effects of flow conditions and vessel geometry.

Future studies should investigate shear-dependent rheological models in healthy arterial and/or diseased venous models which may have considerably fewer regions of low shear flow, as well as study other well known constitutive models for blood such as the Casson and Herschel-Bulkley.

CHAPTER III

Numerical Considerations for Advection-Diffusion Problems in Cardiovascular Hemodynamics

3.1 Introduction

Mass transport of biochemical species plays an important role in numerous cardiovascular pathologies including thrombosis and atherosclerosis. Computational models of mass transport offer the unique capability to study various biochemical processes essential to understand the kinetics of disease progression, but which are otherwise difficult to measure *in vivo*. However, cardiovascular mass transport problems are characterized by highly advective flows (with Péclet numbers up to 10^7) that make obtaining an accurate numerical solution challenging. Furthermore, every outlet face of a computational model is an artificial boundary resulting from the arbitrary truncation of a vessel. Therefore, it is necessary to prescribe realistic boundary conditions that result in a stable solution at outlet faces while preserving the accuracy of the solution.

In this work, we present a stabilized finite element framework that incorporates three salient features: (i) a backflow stabilization technique to obtain stable solutions with Neumann outflow boundaries for scalar advection-diffusion problems, (ii) a consistent flux boundary condition that minimally disturbs the local physics of the problem on outflow boundaries resulting from the artificial truncation of vessels; and (iii) a front-capturing stabilization technique to regularize the solution with a concentration front in scenarios of high Péclet numbers.

Backflow Stabilization: Neumann conditions have typically been prescribed for outlet boundaries in cardiovascular flows, either through direct imposition of a known traction (i.e. zero or constant pressure condition)[102,111] or, more recently, through the coupling of reduced order models (i.e. lumped parameter networks) of the distal vasculature, which ultimately results in the specification of a time-varying weak traction on the outlet face[135]. However, Neumann conditions in boundaries exhibiting partial or complete inflow are known to lead to numerical divergence[18,21,22,41–43,48,51,74,77,97,100,114]. Specifically, prescribing a diffusive flux fails to guarantee stable energy estimates due to the unknown velocity profile at these boundaries[54]. To mitigate these difficulties associated with flow modeling, several strategies have been proposed including adding a backflow stabilization term to the boundary nodes[13,18,21,22,41–43,48,54,77,100,114], constraining the velocity to be normal to the outlet[97], or using Lagrange multipliers to constrain the velocity profile at all or some of the outlets[74]. A comparison of these strategies determined that backflow stabilization was the most robust approach with the least impact on both the solution and computational cost[97].

Similar scenarios of numerical instability can arise in scalar advection-diffusion systems[65]. Despite the numerous reports on backflow stabilization for flow problems[12,18,21,22,41–43,48,74,77,97,100,114] and 2D heat mass transfer[27,84,99,108,109], these strategies have not been adopted for 3D cardiovascular scalar advection-diffusion systems. Instead, to circumvent the numerical instability issues in the presence of backflow, mass transport models have resorted to unphysical approaches such as the imposition of arbitrary Dirichlet boundary conditions at the outlet faces[8,57], artificial extensions of the computational domain[47] that seek to regularize the flow profile, or an artificial increase in the diffusivity of the scalar[16,50]. In this work, we propose a stabilization method for outlet Neumann boundaries, following the ideas presented by Hughes and Wells[65].

Consistent Flux Boundary Condition: While there have been numerous contributions proposing outflow boundary conditions for cardiovascular flow problems[135], little work has been done for the scalar advection-diffusion problem. Typically, cardiovascular mass transport models have employed either Dirichlet or Neumann conditions prescribing known scalar concentrations[8,57] or diffusive fluxes[81,151] at the outlet face, respectively. An alternative choice of boundary condition, henceforth referred to as "consistent boundary condition" has been shown to provide better error estimates[55]. This approach relies on calculating the consistent diffusive flux (rather than imposing an arbitrary diffusive flux) that satisfies the weak form of the mass transport equation. To the best of our knowledge, this boundary condition has been thus far unexplored for cardiovascular mass transport problems. In this work, we demonstrate the superior performance of this approach over the traditional zero diffusive flux boundary condition.

Front-Capturing Stabilization Techniques: Another important issue concerning simulation of mass transport in cardiovascular applications is the presence of high Péclet number flows typically found in the large arteries. These advection-dominated flows lead to the development of steep concentration gradients, thereby necessitating the use of stabilization techniques to avoid unphysical oscillations in the numerical solution near the concentration front. To address this issue, several discontinuity capturing methods have been proposed[32,35,64]. In this work, we discuss the performance of the discontinuity capturing (DC) stabilization technique, implemented in the context of a streamline upwind Petrov-Galerkin (SUPG) stabilized finite element formulation.

Numerical results are presented in both idealized and patient-specific geometries to demonstrate the efficacy of the proposed numerical procedures. Lastly, to build on the work of Chapter II the scalar mass transport framework is applied to the arterial and venous models previously used to investigate the effects of non-Newtonian rheology on mass transport.

3.2 Methods

3.2.1 Strong form and boundary conditions

The strong form of the governing equation for mass transport in a three-dimensional bounded domain $\Omega \subset \mathbb{R}^3$ is given as

$$\frac{\partial c}{\partial t} + \mathbf{u} \cdot \nabla c - \nabla \cdot (D \nabla c) = r \qquad \text{in} \quad \Omega, \tag{3.1}$$

where c, D, r, and t denote the concentration of the scalar, diffusion coefficient, source (or reaction) terms and time, respectively and $\mathbf{u}$ is a known, solenoidal velocity field. Ω is a open set with boundary $\Gamma = \partial\Omega$, such that:

$$\Gamma = \overline{\Gamma_D \cup \Gamma_N}, \tag{3.2}$$

$$\Gamma_D \cap \Gamma_N = \emptyset, \tag{3.3}$$

where Γ_D and Γ_N are the Dirichlet and Neumann partitions of the boundary Γ, respectively.

We consider a further partition of $\Gamma = \overline{\Gamma^{\text{in}} \cup \Gamma^{\text{out}}}$, $\Gamma^{\text{in}} \cap \Gamma^{\text{out}} = \emptyset$ such that:

$$\Gamma^{\text{in}}(t) = \{\mathbf{x} \in \Gamma | u_n(\mathbf{x}, t) \leq 0\}, \tag{3.4}$$

$$\Gamma^{\text{out}}(t) = \Gamma - \Gamma^{\text{in}}(t), \tag{3.5}$$

where u_n is the dot product of the velocity with the outward unit normal at the boundary, $\mathbf{x}$ is the position vector, $\Gamma^{\text{in}}(t)$ is the inflow boundary, and $\Gamma^{\text{out}}(t)$ is the outflow boundary. $\Gamma^{\text{in}}(t)$ and $\Gamma^{\text{out}}(t)$ are functions of time owing to the time dependence of the velocity field. In this manuscript, the terms 'outlet' and 'inlet' are used to refer to spatially fixed positions of boundary faces, while the terms 'inflow boundary' and 'outflow boundary' are used to refer to regions of the boundary that exhibit inflow and outflow at a given time instant, respectively. Given these definitions, a total of four distinct boundaries can be defined for mass transport problems[65]:

$$\Gamma^{\alpha}_{\beta}(t) = \Gamma_{\beta} \cap \Gamma^{\alpha}(t), \qquad \alpha = \{\text{in}, \text{out}\}, \quad \beta = \{\text{D}, \text{N}\} \tag{3.6}$$

Typically, finite element simulations of mass transport have considered Dirichlet boundary conditions on inlet faces and Neumann boundary conditions on outlet faces. However, this strategy often shows numerical divergence if backflow occurs on the Neumann boundary (e.g., if $\Gamma^{\text{in}}_{N}(t) \neq \emptyset$). Indeed, it has been shown that the prescription of diffusive flux on a $\Gamma^{\text{in}}_{N}(t)$ boundary fails to guarantee stable energy estimates and therefore leads to numerical divergence[54]. Prescribing the total flux on inflow Neumann boundaries $\Gamma^{\text{in}}_{N}(t)$ mitigates this issue, whereas the diffusive flux can be safely prescribed on outflow Neumann boundaries $\Gamma^{\text{out}}_{N}(t)$[65], viz:

$$D\nabla c \cdot \mathbf{n} = h^{\text{out}} \qquad \text{on} \qquad \Gamma^{\text{out}}_{N}(t), \tag{3.7}$$

$$-c\mathbf{u} \cdot \mathbf{n} + D\nabla c \cdot \mathbf{n} = h^{\text{in}} \qquad \text{on} \qquad \Gamma^{\text{in}}_{N}(t). \tag{3.8}$$

Here, h^{out} and h^{in} denote the diffusive and total (i.e., advective plus diffusive) flux data, respectively.

3.2.2 Weak form

The Galerkin weak form for the scalar advection-diffusion problem governed by Eq. 3.1 is as follows: find $c \in H^1(\Omega)$ such that

$$\int_{\Omega} \left[\delta_c \frac{\partial c}{\partial t} + \delta_c \mathbf{u} \cdot \nabla c + \nabla \delta_c \cdot D\nabla c\right] \mathrm{d}V - \int_{\Gamma_N} \delta_c \left(D\nabla c\right) \cdot \mathbf{n} \mathrm{d}A = \int_{\Omega} \delta_c r \mathrm{d}V \qquad \forall \delta_c \in H^1_0(\Omega) \tag{3.9}$$

where δ_c is a weighting function, $H^1(\Omega)$ is a (solution) space of once-differentiable functions satisfying the Dirichlet boundary conditions on Γ_D, and $H_0^1(\Omega)$ is a (weighting) space of once-differentiable functions vanishing on the Dirichlet boundary Γ_D. Since cardiovascular mass transport problems are characterized by high Péclet number flows, we utilize a SUPG stabilized finite element formulation[19], resulting in the following discrete weak form:

$$\begin{aligned}\int_{\Omega} \left[\delta_c \frac{\partial c}{\partial t} + \delta_c \mathbf{u} \cdot \nabla c + \nabla \delta_c \cdot D \nabla c\right] \mathrm{d}V - \int_{\Gamma_N} \delta_c \left(D \nabla c\right) \cdot \mathbf{n} \mathrm{d}A \\ + \sum_{i=1}^{n_{\mathrm{el}}} \int_{\Omega_i} \nabla \delta_c \cdot \mathbf{u} \tau \mathcal{R} \mathrm{d}V = \int_{\Omega} \delta_c r \mathrm{d}V \qquad \forall \delta_c \in H_0^1(\Omega)\end{aligned} \tag{3.10}$$

where n_{el} denotes the total number of elements in the discretized domain, Ω_i is the domain of the i-th element, τ is the stabilization parameter, and $\mathcal{R}$ is the residual given as

$$\mathcal{R} = \frac{\partial c}{\partial t} + \mathbf{u} \cdot \nabla c - D \nabla^2 c - r. \tag{3.11}$$

The stabilization parameter τ is given as

$$\tau^{-2} = \tau_1^{-2} + \tau_2^{-2} + \tau_3^{-2}, \tag{3.12}$$

$$\tau_1^{-2} = \left(\frac{\Delta t}{2}\right)^{-2}, \qquad \tau_2^{-2} = \mathbf{u} \cdot \mathbf{g} \mathbf{u}, \qquad \tau_3^{-2} = 9 D^2 \mathbf{g} : \mathbf{g}, \qquad \mathbf{g} = \left(\frac{\partial \xi}{\partial \mathbf{x}}\right)^T \frac{\partial \xi}{\partial \mathbf{x}}, \tag{3.13}$$

where Δt is the time step size, $:$ is the Frobenius inner product, and $\mathbf{g}$ is the metric tensor based on the Jacobian of the mapping between the element coordinates ξ and the physical coordinates $\mathbf{x}$ (e.g. in 1D, $g = 4/h^2$). We remark that, without loss of generality, the examples shown in this article all use a zero reaction term and hence no contributions from the reaction terms appear in the above-mentioned stabilization terms.

3.2.3 Backflow stabilization and total flux

Using Eqs. 3.7 and 3.8, the Neumann boundary term in Eq. 3.10 becomes

$$\begin{aligned}\int\limits_{\Gamma_N} \delta_c \left(D\nabla c\right) \cdot \mathbf{n} \mathrm{d}A &= \int\limits_{\Gamma_N^{\mathrm{out}}(t)} \delta_c \left(D\nabla c\right) \cdot \mathbf{n} \mathrm{d}A + \int\limits_{\Gamma_N^{\mathrm{in}}(t)} \delta_c \left(D\nabla c\right) \cdot \mathbf{n} \mathrm{d}A, \\ &= \int\limits_{\Gamma_N^{\mathrm{out}}(t)} \delta_c h^{\mathrm{out}} \mathrm{d}A + \int\limits_{\Gamma_N^{\mathrm{in}}(t)} \delta_c \left(D\nabla c - c\mathbf{u}\right) \cdot \mathbf{n} \mathrm{d}A + \int\limits_{\Gamma_N^{\mathrm{in}}(t)} \delta_c c\mathbf{u} \cdot \mathbf{n} \mathrm{d}\mathbf{A}, \\ &= \int\limits_{\Gamma_N^{\mathrm{out}}(t)} \delta_c h^{\mathrm{out}} \mathrm{d}A + \int\limits_{\Gamma_N^{\mathrm{in}}(t)} \delta_c h^{\mathrm{in}} \mathrm{d}A + \int\limits_{\Gamma_N^{\mathrm{in}}(t)} \delta_c c\mathbf{u} \cdot \mathbf{n} \mathrm{d}A. \end{aligned} \tag{3.14}$$

As indicated earlier, diffusive flux Neumann boundary conditions are typically prescribed at outlet faces $\Gamma_N^{\mathrm{out}}(t)$. In this scenario, the last term of Eq.3.14 (i.e., advective flux) vanishes since $\Gamma_N^{\mathrm{in}}(t) = \emptyset$. However, in cases where $\Gamma_N^{\mathrm{in}}(t) \neq \emptyset$, the total flux must be prescribed and therefore the advective flux term in Eq. 3.14 is non-trivial and must be included in Eq. 3.10 to obtain a stable solution. Previous publications on backflow stabilization for Navier-Stokes problems have introduced a parameter β scaling the advective flux contribution[13,54,97]. However, owing to the lack of mathematical rigor justifying the introduction and choice of such a scaling factor, we do not consider it for the scalar advection-diffusion problem.

3.2.4 Consistent flux boundary condition

The boundary conditions imposed at artificial boundaries generated due to the truncation of a physical domain form a crucial component of the computational model. Since the downstream physics for mass transport applications is often unknown at such artificial boundaries, the task of identifying appropriate conditions that preserve the accuracy of the solution remains challenging.

While there have been numerous contributions proposing conditions for artificial boundaries in cardiovascular flow problems, little work has been done for the scalar advection-diffusion problem. Typically, cardiovascular mass transport models have employed either

Dirichlet or Neumann conditions prescribing scalar concentrations[8,57] or diffusive fluxes[81,151] at the outlet face as in Eq. 3.7, respectively. Neither of these approaches is ideal, since they assume knowledge of a physical quantity which is typically unknown. While imposing an arbitrary Dirichlet outlet boundary condition renders a stable solution, it severely affects the scalar solution field and has resulted in approaches relying on extending the outflow branches to minimize the impact of such conditions in the region of interest[8,57]. These approaches also increase the computational cost due to the larger domain. Conversely, a zero diffusive flux condition has been used more sporadically (likely due to the numerical instabilities associated with backflow, as noted above), and, while seemingly less intrusive than a Dirichlet condition, it still fundamentally prescribes an unknown property of the solution field.

An alternative to this zero diffusive flux condition, proposed in the context of the Navier-Stokes equations by Papanastasiou and Malamataris[106], is to calculate the diffusive flux that satisfies the weak form of the mass transport equation and iteratively impose it as a boundary condition. This approach amounts to treating the boundary integral in the weak form given by Eq. 3.9 as unknown and is particularly useful when analytic or asymptotic techniques cannot predict the physics downstream from the artificial outlets, making it challenging to formulate appropriate boundary conditions at these faces. The strategy of leaving an undefined boundary integral could lead to an ill-posed variational form, particularly in diffusion-dominated problems which are more elliptical in nature and thus necessitate specification of conditions on every boundary. Conversely, advection-dominated problems have a stronger hyperbolic behavior and are less likely to be affected by the ill-posedness of this strategy. For a more detailed discussion on the mathematical implications of this approach, we refer the reader to the work of Griffiths[55] and Renardy[121].

In the context of the Navier-Stokes equations, these boundary conditions have been referred to using different terminologies such as “no boundary condition” or “free boundary condition”[55,106]. However, here we will refer to them as “consistent flux boundary condition”. In this work, we employ both the zero diffusive flux (see Eq. 3.7), and the consistent flux boundary conditions for the scalar advection-diffusion problem and compare their performance in preserving the local physics of the computed solution.

3.2.5 Discontinuity capturing operator

In the context of high Péclet number flows, SUPG stabilized formulations for scalar advection-diffusion problems fail to resolve the steep gradients in the solution, resulting in numerical undershoot/overshoot in concentrations near the scalar front. Therefore, in addition to SUPG stabilization, we implemented a discontinuity capturing (DC) operator to resolve steep gradients in the solution[79]. This approach introduces an additional term for each element of the form $\nabla\delta_c \cdot \nu_{DC}\nabla c$ in Eq. 3.10 similar to the last term on the LHS. ν_{DC} is defined as

$$\nu_{DC} = \max[0, \omega_{DC}]\,\tilde{\mathbf{g}}, \tag{3.15}$$

where $\tilde{\mathbf{g}}$ is the contravariant counterpart of the metric tensor introduced in Eq. 3.13 and

$$\omega_{DC} = f_{DC}\sqrt{\frac{\mathcal{R}^2}{\nabla c \cdot \tilde{\mathbf{g}}\nabla c}} - \tau\frac{\mathcal{R}^2}{\nabla c \cdot \tilde{\mathbf{g}}\nabla c}, \tag{3.16}$$

where $f_{DC} = 1$ for linear finite elements and τ is the stabilization parameter defined in Eq. 3.12. We want to make two remarks on the DC term: 1) it involves gradients of the weighting function and thus, conservative properties of the semi-discrete form are unchanged[65], and 2) it makes the weak form of the scalar advection-diffusion problem nonlinear. Therefore, the resolution of gradients near the concentration front is obtained at an increased computational expense. For nonlinear scalar problems, however, the increase in computational cost due to the use of DC operator is not high (as discussed later).

3.3 Numerical Examples

In this section, we present numerical results to illustrate the suitability of the proposed computational framework. The following applies to all the numerical examples presented in this section:

- A flow solution is first obtained by solving the stabilized Navier-Stokes equations using the cardiovascular hemodynamics modeling environment, CRIMSON[6]. All walls are modeled as rigid (i.e., homogeneous Dirichlet boundary conditions for the velocity field) and blood is modeled with a density of 1060 kg/m^3.
- In Sections 3.3.1 and 3.3.2 blood is modeled as a Newtonian fluid with a dynamic viscosity of 0.004 Pa $\cdot$ s. In Section 3.3.3 blood is modeled as both a Newtonian fluid with a dynamic viscosity of 0.0035 Pa $\cdot$ s and as a Carreau-Yasuda fluid based on parameters described in Table 2.1.
- For all flow solutions backflow stabilization was used when solving the Navier-Stokes equations.
- For the mass transport problems, a constant concentration of $c = 10$ mol/mm^3 is prescribed at the inlet face(s) and a zero concentration flux boundary condition is applied to all walls. An initial concentration of $c = 0$ mol/mm^3 is assumed for all mass transport problems.

3.3.1 Idealized geometries

To provide a better understanding of specific numerical challenges, we first present results for cases where idealized geometries and problem parameters are chosen to isolate specific numerical challenges. Here, we present results for three specific cases that highlight the effectiveness of the different components of the proposed computational framework.

3.3.1.1 Backflow stabilization

To illustrate the numerical issues caused by $\Gamma_N^{\text{in}}(t)$ boundaries, we consider a T-shaped bifurcation as shown in Figure 3.1. The choice of geometry and boundary conditions of this problem leads to partial backflow at the outlet faces even under steady flow conditions. A velocity field was obtained by prescribing a constant inlet flow of 196 mm^3/s, mapped to a parabolic velocity profile, resulting in a maximum velocity of $\text{v}_{\text{max}} = 2000$ mm/s, a mean velocity of $\text{v}_{\text{mean}} = 1000$ mm/s, and a Reynolds number $\text{Re}_{\text{mean}} = 66.25$, based on the mean velocity and the inlet radius. A zero traction boundary condition was applied at both outlet faces. For the scalar advection-diffusion problem, a zero diffusive flux condition was prescribed at the outlet faces. The diffusion coefficient was set to $D = 10^{-2}$ mm^2/s, resulting in a Péclet number of $\text{Pe}_{\text{mean}} = 2.5 \times 10^4$. The domain was discretized using linear tetrahedral elements with characteristic length of 10^{-2} mm, resulting in a total mesh size of 11.3 million elements. Simulations were run using a constant time-step size of $\Delta t = 10^{-5}$ s

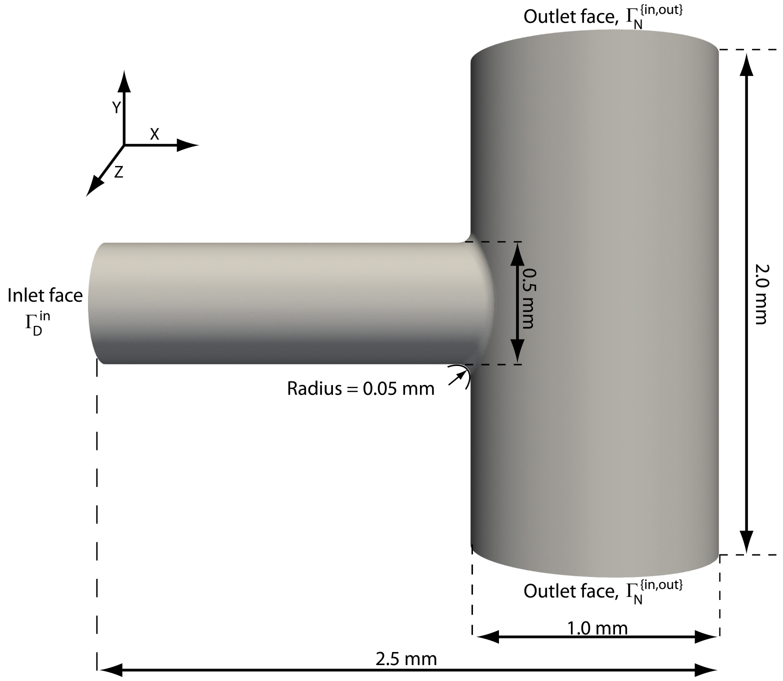

Figure 3.1: 3D T-shaped bifurcation model.

for 8000 time steps.

Figure 3.2(A) shows the velocity field plotted at the mid-plane of the T-shaped bifurcation perpendicular to the Z direction. The velocity profiles at the outlet faces exhibit backflow, Figure 3.2(B). Figure 3.3(A) shows the solution for the scalar concentration at $t = 0.036$ s, obtained without backflow stabilization. The solution presents strong numerical artifacts on the top outlet boundary, corresponding to the $\Gamma_N^{\text{in}}(t)$ region of the outlet boundary. These numerical artifacts eventually lead to divergence of the simulation and also appear in the bottom outlet boundary over time. In contrast, the proposed backflow stabilization technique yields a stable solution as shown in Figure 3.3(B). We would like to point out that the two numerical solutions in Figure 3.3(A) and Figure 3.3(B) exhibit spurious oscillations in the interior of the domain, these will be addressed in Section 3.3.1.3.

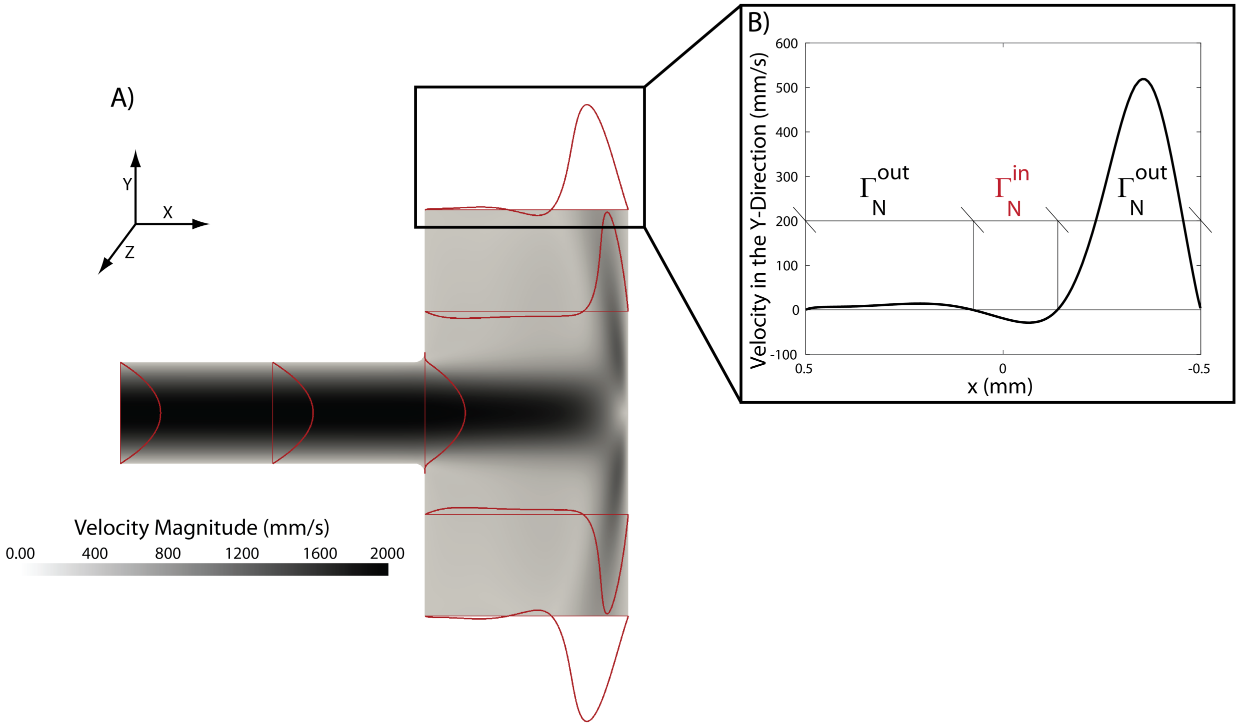

Figure 3.2: A) Velocity contours in the mid-plane of the T-shaped bifurcation. Red lines indicate velocity profiles at discrete number of locations. B) Close-up view of the velocity at the outlets, illustrating backflow in a small segment of the outlet face.

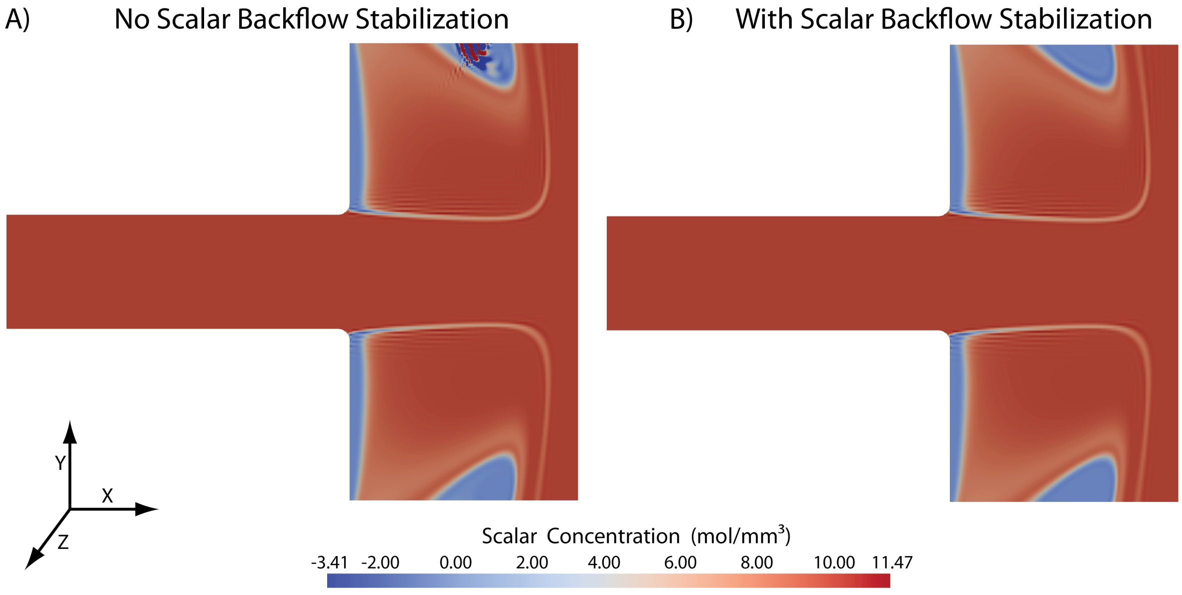

Figure 3.3: Scalar contours at time t = 0.036s in the T-Bifurcation. A) No backflow stabilization resulting in an unstable solution, and B) With backflow stabilization resulting in a stable solution in the presence of backflow.

3.3.1.2 Consistent flux boundary condition

In this example, we compare the behavior of the consistent flux and the zero diffusive flux boundary conditions. We consider two cylindrical domains of diameter $d = 1.0$ mm and lengths $l_1 = 10$ mm and $l_2 = 5$ mm, respectively. For each cylindrical domain, we apply both types of boundary conditions, rendering a total of four different scenarios. The ultimate goal of this test is to examine the impact of the boundary conditions on the scalar field, specifically by comparing solutions at the outlet of the shorter cylinder with solutions at the mid-section of the longer cylinder, which are taken as the "reference solution". A desirable feature of the boundary condition is to minimize the impact on the scalar field, given that these conditions are typically prescribed on "artificial" boundaries (i.e., arbitrary truncations of a branch).

Steady flow field solutions were obtained by prescribing a constant flow rate of 196 mm^3/s, mapped to a parabolic velocity profile resulting in a maximum velocity of $\mathrm{v}_{\mathrm{max}} = 500$ mm/s, a mean velocity of $\mathrm{v}_{\mathrm{mean}} = 250$ mm/s and a Reynolds number of $\mathrm{Re}_{\mathrm{mean}} = 33.125$. A zero traction boundary condition was applied at the outlet face. For the mass transport problem, a constant value of diffusivity was adopted, $D = 10^2$ mm^2/s, resulting in Péclet number of $\mathrm{Pe}_{\mathrm{mean}} = 1.25$. This relatively low Péclet number was chosen because it amplifies the differences between zero diffusive and consistent flux boundary conditions. Simulations were run using a constant time-step size of $\Delta t = 10^{-4}$ s for 8000 time steps.

Figure 3.4(A) shows scalar concentration contours at $t = 0.042$ s. for the long (i-ii) and short (iii-iv) cylinders, respectively. Figure 3.4(B) shows scalar concentration profiles at the mid-section of the long cylinder (i-ii) and the outlet face of the short cylinder (iii-iv). For the long cylinder, the solutions overlap each other, indicating that at this location far away from the boundary, and this point in time, there is no noticeable difference between solutions obtained with either boundary condition. For the short cylinder, however, there is a noticeable difference between the solutions obtained with the zero diffusive and consistent flux boundary conditions. Taking the solution in the long cylinder as the "reference solution", it can be observed that the zero diffusive flux condition renders 10% larger scalar concentration values. In contrast, the consistent flux boundary condition yields scalar values much closer to the true solution, overestimated by just 0.015%. These results illustrate the superior performance of the consistent flux boundary condition in preserving the local physics of the numerical solution near artificial boundaries.

3.3.1.3 Discontinuity capturing operator

Having addressed numerical issues concerning outlet boundaries, we now focus our attention to spurious oscillations in the numerical solution around the concentration front within the computational domain. We consider the flow solution for the shorter cylindrical domain ($l_2 = 5$ mm) described in the previous section. A smaller diffusion coefficient $D = 10^{-2}$ mm^2/s was adopted, resulting in a higher Péclet number of $\mathrm{Pe} = 1.25 \times 10^4$, that is of practical interest and exhibits spurious oscillations. A consistent flux boundary condition was prescribed at the outlet face. Same mesh and time step size were used as in

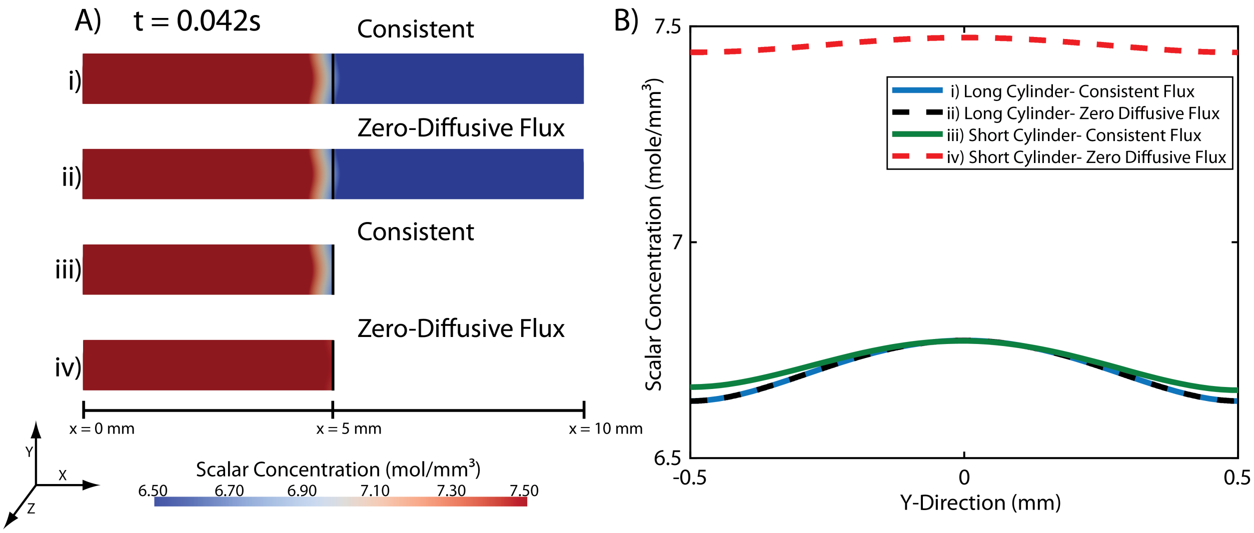

Figure 3.4: A) Scalar contours for four different cylinders. From top to bottom: (i) 10 mm cylinder with the consistent flux outflow boundary condition, (ii) 10 mm cylinder with a zero Neumann outflow boundary condition, (iii) 5 mm cylinder with the consistent flux boundary condition, and (iv) 5 mm cylinder with a zero Neumann boundary condition. B) Line plot showing scalar concentration across the cylinder at X = 5 mm for cases i-iv.

the previous section.

Figures 3.5(A) and Figure 3.5(B) show concentration contours obtained without and with the DC operator, respectively. Undershoot/overshoot in the numerical solution is apparent near the wavefront of the scalar field when no DC operator is used. These oscillations result in unphysical negative scalar concentrations ($-0.98\,\mathrm{mol/mm^3}$) as well as in values higher than those imposed at the inlet ($11.92\,\mathrm{mol/mm^3}$). Figure 3.5(C) shows plots of the scalar concentration along the centerline of the cylinder at different times. It can be observed that spurious oscillations begin in the numerical solution without the DC operator (red line) within the first five time steps ($t = 0.0005$ s) and increase in magnitude with time. In contrast, the use of the DC operator (black line) results in smooth solution profiles for all times.

3.3.2 Patient-specific geometry

Having demonstrated the capabilities of the stabilized computational framework in idealized geometries under steady flows, we now shift our focus to a patient-specific geometry

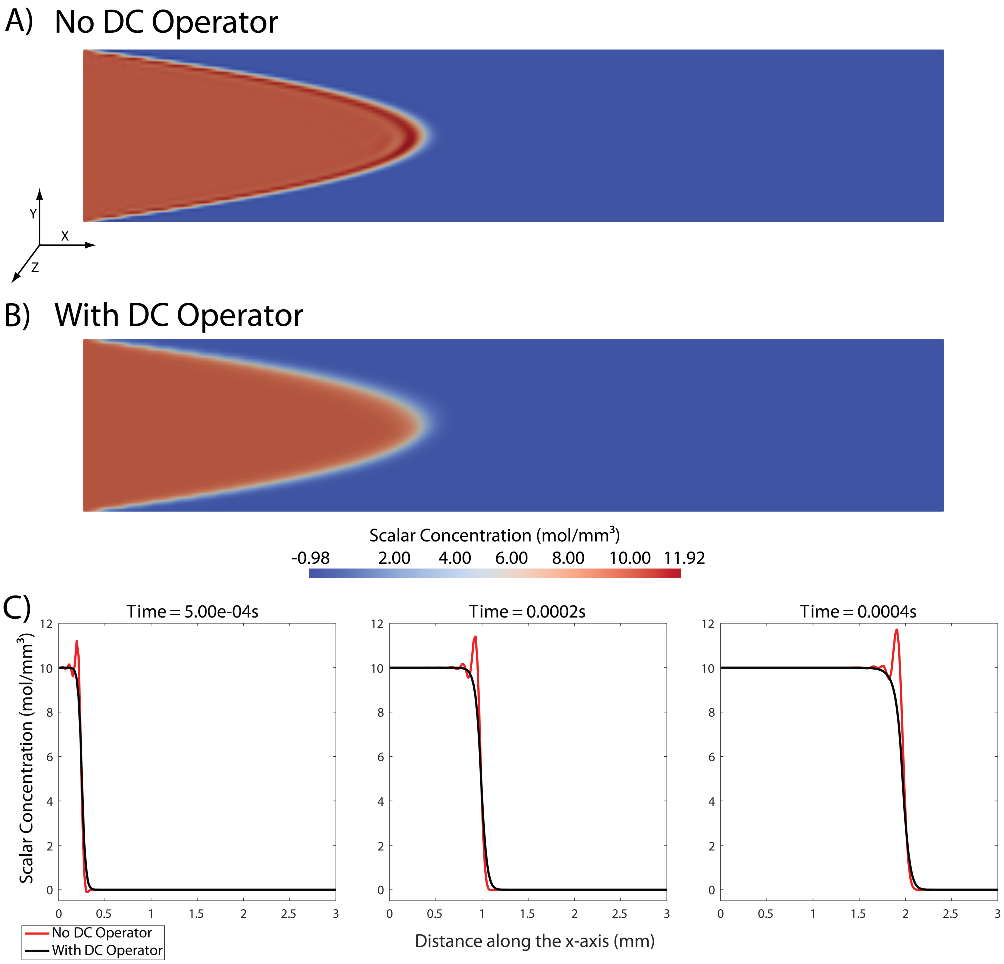

Figure 3.5: A) Scalar contours of 5mm cylinder without the DC Operator at $t = 4 \times 10^{-3}$ s. B) Scalar contours with the DC Operator at $t = 4 \times 10^{-3}$ s. C) Scalar concentration along the center of the cylinder with and without DC Operator at three instances in time: $t = 5 \times 10^{-4}$ s, $t = 2 \times 10^{-3}$ s and $t = 4 \times 10^{-3}$ s.

of a human thoracic aortic aneurysm under periodic flow conditions[133]. The aortic geometry was built from computed tomography angiography (CTA) image data using the cardiovascular hemodynamic modeling environment CRIMSON[6]. Figure 3.6 shows the computational domain comprised of the ascending aorta and nine outlet branches. The aortic geometry was discretized into 6.2 million linear tetrahedral elements and 1.1 million nodes. An echocardiography-derived periodic flow waveform (with time period $T = 0.91\,\mathrm{s}$) mapped to a parabolic velocity profile was imposed at the aortic inflow, resulting in a maximum Reynolds number of approximately $\mathrm{Re}_{\max} = 2.1x10^3$. Three-element Windkessel models[135] were prescribed at each outlet face, representing the behavior of the distal vascular beds (numerical values given in Appendix A)[133]. Cycle-to-cycle periodicity was achieved after running the flow problem under rigid wall assumptions for four cardiac cycles, corresponding to a physical time of $t = 3.64\,\text{s}$. Subsequently, the scalar advection-diffusion equation was solved, assuming a zero concentration initial condition, a constant Dirichlet inlet boundary condition of $c = 10\ \text{mol/mm}^3$, and zero total flux boundary conditions at the vessel walls for $t > 3.64\,\text{s}$. Simulations were run using a constant time step size of $\Delta t = 10^{-4}\,\text{s}$.

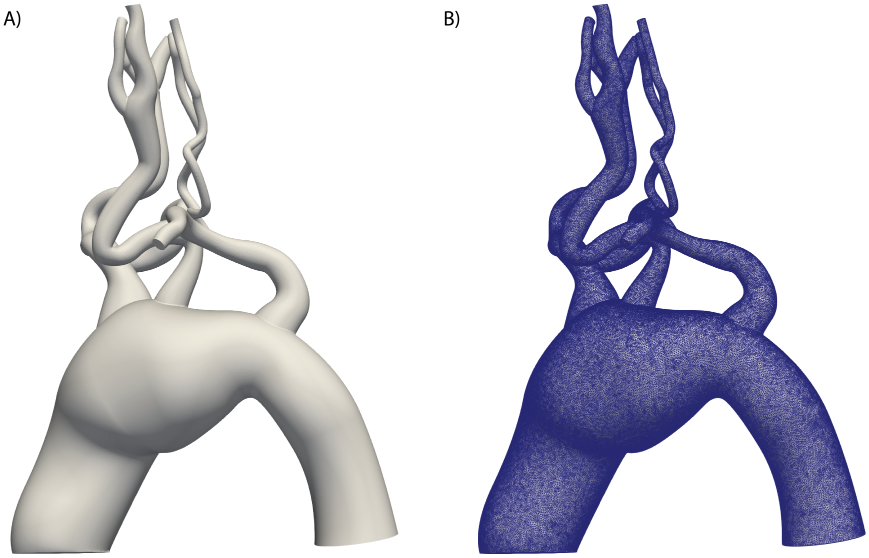

Figure 3.6: A) 3D geometric model reconstructed from CTA image data. B) Computational mesh used in all patient-specific simulations. Both the geometric model and computational mesh were created using CRIMSON.

3.3.2.1 Backflow stabilization

We first studied the issue of numerical instabilities on inflow Neumann boundaries (Γ_N^{in}). A constant diffusion coefficient, $D = 1.0\,\text{mm}^2/\text{s}$ was used, resulting in a maximum Péclet number of $\text{Pe}_{\text{max}} = 8.0x10^3$ at the inlet face. Zero diffusive flux boundary conditions were prescribed on each outlet face. Figure 3.7(A) shows a 3D warp of the velocity profile at the aortic outlet boundary in mid-diastole ($t = 4.39\,\text{s}$). Flow reversal is apparent on this boundary at this point in time. Using the standard zero diffusive flux boundary condition without backflow stabilization leads to instabilities in the numerical solution and eventual divergence, see Figure 3.7(B). Figure 3.7(C) shows the corresponding stable scalar concentration solution obtained with the inclusion of backflow stabilization. There was no significant difference in computational cost between solutions obtained with and without backflow stabilization.

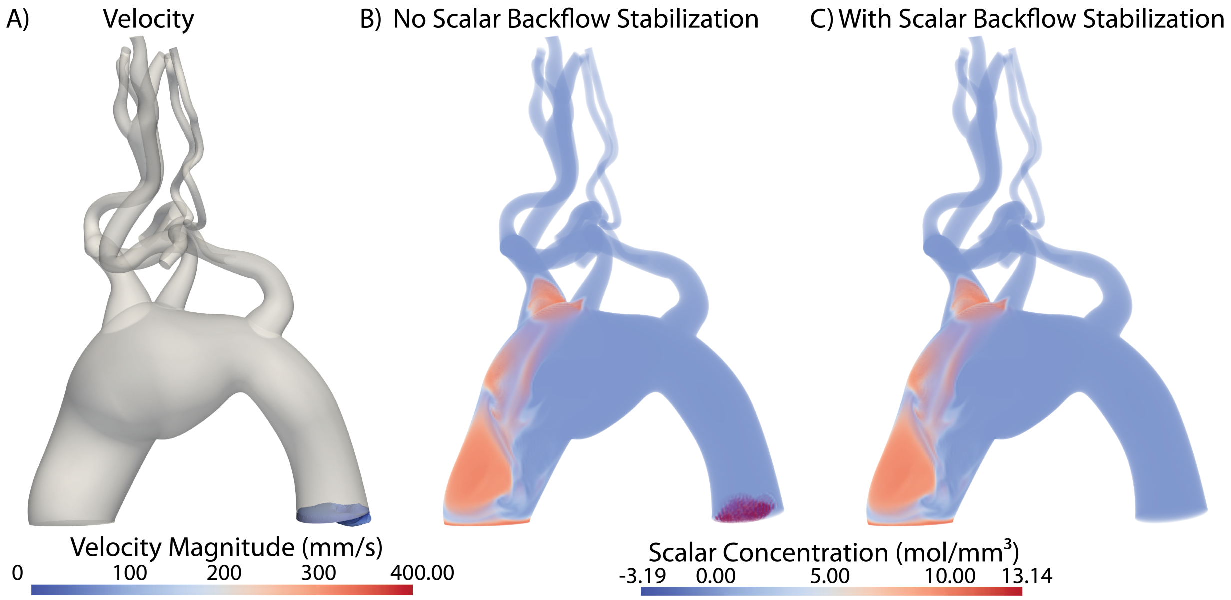

Figure 3.7: A) Computational domain with thoracic aortic aneurysm showing flow reversal at the descending thoracic aorta outlet. Surface contours of scalar concentration at time $t = 4.39\,\mathrm{s}$. B) Without scalar backflow stabilization numerical instability is observed at the thoracic aorta outlet that proceeds to pollute the scalar domain. C) With backflow stabilization a stable scalar solution is obtained in the presence of backflow at an outlet.

3.3.2.2 Consistent flux boundary condition

We next studied the performance of the consistent flux versus the zero diffusive flux boundary condition. In both cases, backflow stabilization and a constant value of diffusion coefficient $D = 10^2\,\mathrm{mm}^2/\mathrm{s}$ were used resulting in a maximum Péclet number of $\mathrm{Pe}_{\max} = 80$ at the inlet face. Figure 3.8 shows the geometric model with four arbitrary locations A-D along the aorta. Scalar concentration profiles obtained with both boundary conditions at $t = 6.55\,\mathrm{s}$ for locations A-D are given. The concentration profiles show substantial variations along the cross section of the vessel for each location, highlighting the contribution of the advection to the concentration profile. For instance, panels A and B show larger values of concentration along the outer curvature of the aorta, where the velocity field is larger. Panels A and B also show close agreement between the solutions obtained with each boundary condition. In contrast, panels C and D show clear differences between the scalar concentration profiles, with discrepancies between solutions increasing in locations closer to the outlet boundary. Location D shows substantial differences in numerical values and concentration profiles between the two solutions. These results highlight the intrusiveness of the zero diffusive flux boundary condition, particularly in regions of the computational domain near the outlet boundaries. There was no significant difference in computational cost between solutions obtained with the zero diffusive or consistent flux boundary conditions.

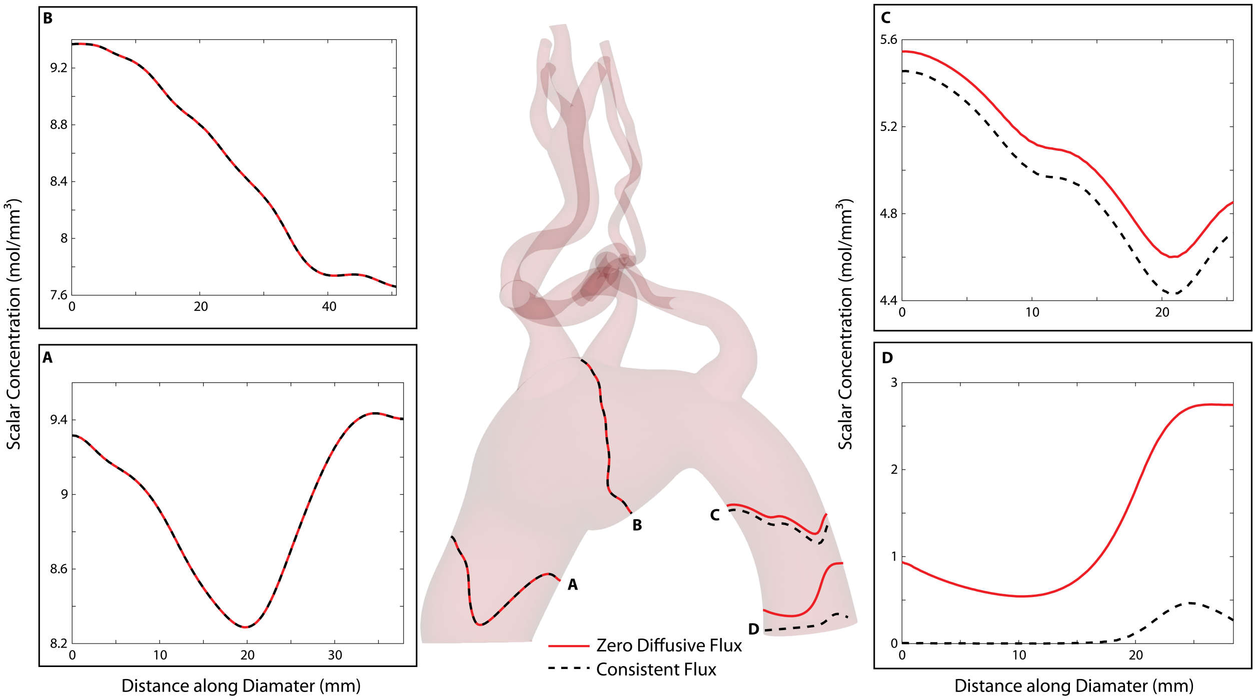

Figure 3.8: Patient-specific simulations in a human thoracic aneurysm were run with both a zero diffusive flux boundary condition (solid red line) and a consistent flux boundary condition (dashed black line). Comparisons of the scalar profile across the diameter of the model is shown at four locations (A-D). Results show that close to the inflow the scalar profile across the aorta is the same for both boundary conditions at outlet faces. After the thoracic aneurysm the scalar profiles begin to differ and the greatest differences are observed near the primary outlet face.

3.3.2.3 Discontinuity capturing operator

In this last example, we demonstrate the efficacy of the DC operator in resolving spurious oscillations in the scalar concentration solution. A constant diffusion coefficient, $D = 1.0\,\mathrm{mm}^2/\mathrm{s}$ was used, resulting in a maximum Péclet number of $\mathrm{Pe}_{\mathrm{max}} = 8.0x10^3$ at the inlet face. Consistent flux boundary conditions were prescribed on each outlet face and backflow stabilization was used. Figures 3.9(A) and (B) shows the concentration contours at $t = 4.04\,\mathrm{s}$ obtained without and with the DC operator, respectively. Numerical undershoot/overshoot is observed near the wavefront of the scalar field when no DC operator is used. Figure 3.9(C) shows a comparison between the two scalar concentration solutions, plotted along an arbitrary line passing through the concentration wavefront. It can be observed that the solution without the inclusion of the DC operator is characterized by spurious oscillations near the concentration wavefront. These oscillations result in unphysical (negative) minimum ($-1.43\,\mathrm{mol/mm}^3$) and maximum ($12.39\,\mathrm{mol/mm}^3$) values of concentration. In contrast, the solution obtained with the inclusion of the DC operator shows always positive, smoothly varying scalar concentrations across the wavefront, devoid of any spurious oscillations.

3.3.3 Effects of non-Newtonian Viscosity on Mass Transport

To further investigate the impact of non-Newtonian rheology on transport in patient-specific arterial and venous flows the stabilized mass transport framework, developed in this work, was applied to the both the arterial and venous models discussed in Chapter II. We prescribed concentrations of species through the inlet face(s) of the computational models under two different viscosity constitutive assumptions (Newtonian and Carreau-Yasuda), and solved the spatio-temporal concentration fields, to study potential discrepancies in mass transport in the lumen and near the vessel wall. For both models, scalar backflow stabilization and discontinuity capturing were used. A zero total flux boundary condition was prescribed at all walls while a consistent-flux boundary condition was prescribed at the outlet

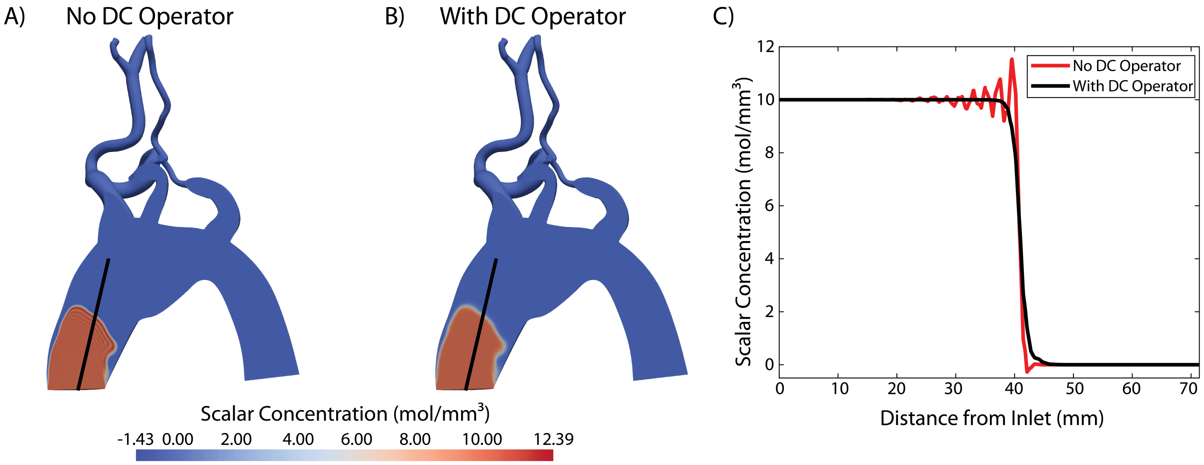

Figure 3.9: Scalar concentration contours at $t = 4.04\,\mathrm{s}$ obtained without (A) and with the DC operator (B), respectively. Oscillations in the scalar solution can be seen near the wavefront in (A); a smooth concentration solution can be seen in (B). The lines (in A and B) indicate the location where the scalar concentration profiles are shown in (C). The use of the DC operator effectively avoids the overshoot/undershoot phenomena seen in the simulation with no DC.

face(s). A constant diffusion coefficient $D = 1.0\,\mathrm{mm}^2/\mathrm{s}$ was used for all species.

Figure 3.10(A) shows the aortic computational domain with four locations (i)-(iv) highlighted along the aorta. Figure 3.10(B) shows volume rendered plots of scalar concentration for the Newtonian and Carreau-Yasuda cases during diastole. Consistent with the differences observed in the hemodynamic flow analysis from Chapter II, see Figs. 2.4, 2.5, and 2.6, the scalar concentration fields also differ significantly in Newtonian vs. Carreau-Yasuda case, particularly in the aneurysmal region. To further investigate these differences, Figure 3.10(C) shows warped scalar concentration profiles at the four locations (i)-(iv) along the aorta, as indicated in Figure 3.10(A). It can be observed that while the mean concentration values in the Newtonian and Carreau-Yasuda cases are similar, there are significant differences in the spatial distribution of the concentration, both in the domain as well as near the wall. Since the initiation and propagation of numerous cardiovascular diseases (e.g., thrombosis, atherosclerosis, etc.) is dictated by near-wall transport[58,60,130], we next investigate the scalar concentration profiles at the wall boundary. Figure 3.10(D) compares the scalar concentration along the wall for Newtonian and Carreau-Yasuda cases at the same four locations, as considered in Figure 3.10(C). Again, significant differences are observed in the concentration profiles, highlighting the importance of considering accurate blood rheological models to assess mass transport in cardiovascular pathologies.

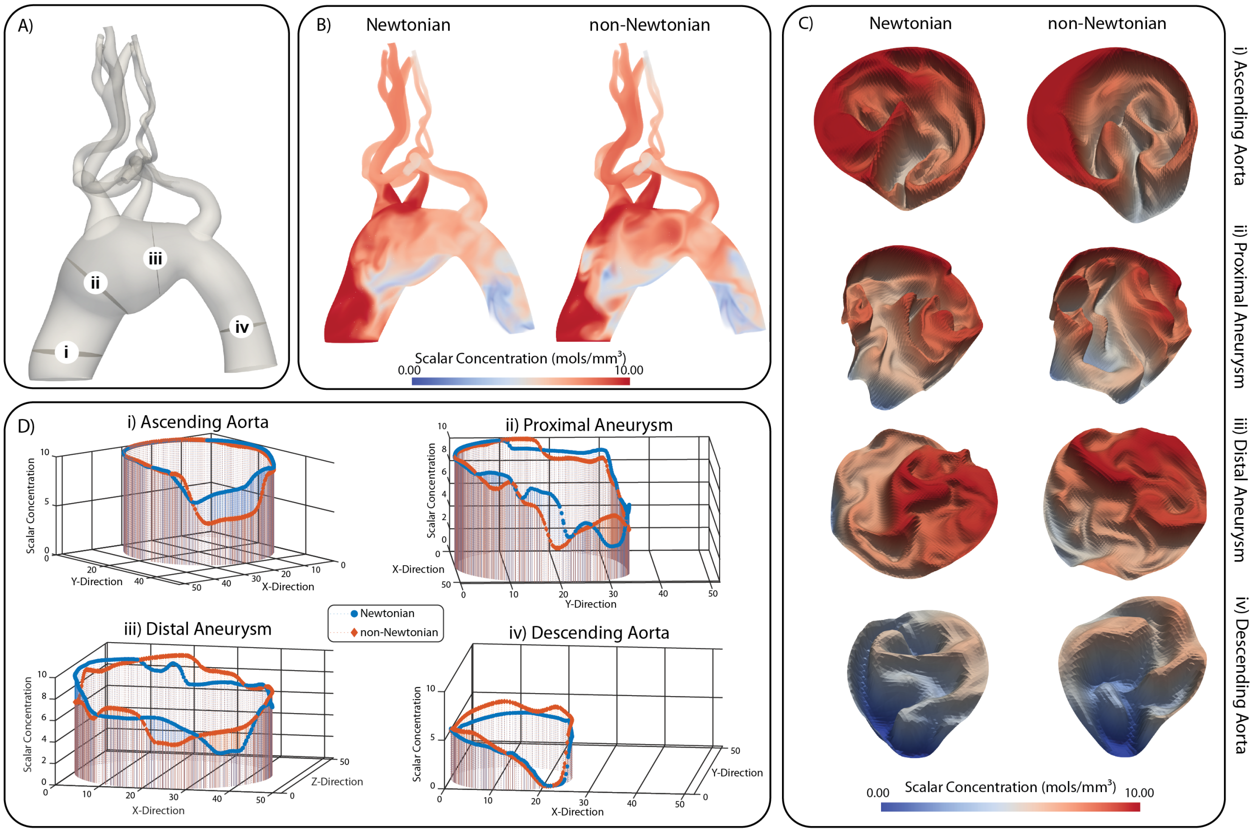

Figure 3.10: (A) Computational domain highlighting four locations (i-iv) along the aortic arch. (B) Volume rendering of the scalar field for the Newtonian and Carreau-Yasuda simulations at time $t = 3.64$s. (C) Warp of the scalar field at locations i-iv. (D) Scalar concentration along the aortic wall at locations i-iv for Newtonian and Carreau-Yasuda simulations.

Next, we perform the scalar mass transport analysis in the venous model from Chapter II. Details on the computational domain, mesh, and boundary conditions for the venous model can be found in Chapter II. In contrast to the arterial model, the venous model has four inlet faces. To separately track the mass transport corresponding to the flow from each of these inlet faces, we consider four distinct scalar species entering the computational domain through these faces. Figure 3.11(A) shows the venous computational domain with three locations highlighted at (i) IVC, (ii) left external iliac, and (iii) external iliac. Figure 3.11(B) shows volume rendered plots of scalar concentration for the Newtonian and Carreau-Yasuda cases at a representative time during the cardiac cycle ($t = 2.4\,\mathrm{s}$). Again, consistent with the differences observed in the hemodynamic flow analysis (Figs. 2.4, 2.5, and 2.6), the scalar concentration fields show significant differences in the Newtonian vs. Carreau-Yasuda case, particularly in the IVC region where the four scalars begin to mix.

Figure 3.11(C) shows contour plots of the concentration of 4 scalars at the three locations, highlighted in Figure 3.11(A). The concentration plot at location (i) shows the mixing of all four scalars with significant qualitative differences between the Newtonian and Carreau-Yasuda case. It is observed that the Carreau-Yasuda case is characterized by smaller gradients in the concentration fields, resulting in smoother concentration profiles. This finding is consistent with the higher viscosity in the Carreau-Yasuda case at lower shear rates that tends to diffuse the gradients in the flow field. The concentration plots at locations (ii) and (iii) show the mixing of scalars entering through the two left and right inlets of the model, respectively. The concentration profiles at these locations show subtle qualitative differences - an interesting finding given the largely unidirectional flow profiles with low vorticity at these locations.

Lastly, Figure 3.11(D) compares the scalar concentration along the wall of the IVC for the Newtonian and Carreau-Yasuda case. Each of the four scalar concentrations is compared between Newtonian and Carreau-Yasuda case and is plotted separately in individual panels. Significant differences are observed in the concentration profiles at the wall, again illustrating the importance of incorporating Carreau-Yasuda viscosity models for accurate assessment of mass transport in cardiovascular disease research.

3.4 Discussion

Transport problems are of paramount importance in studying cardiovascular pathologies. Diseases such as intimal hyperplasia, atherosclerosis and thrombosis are all directly affected by complex transient hemodynamics as well as the transport of numerous chem-

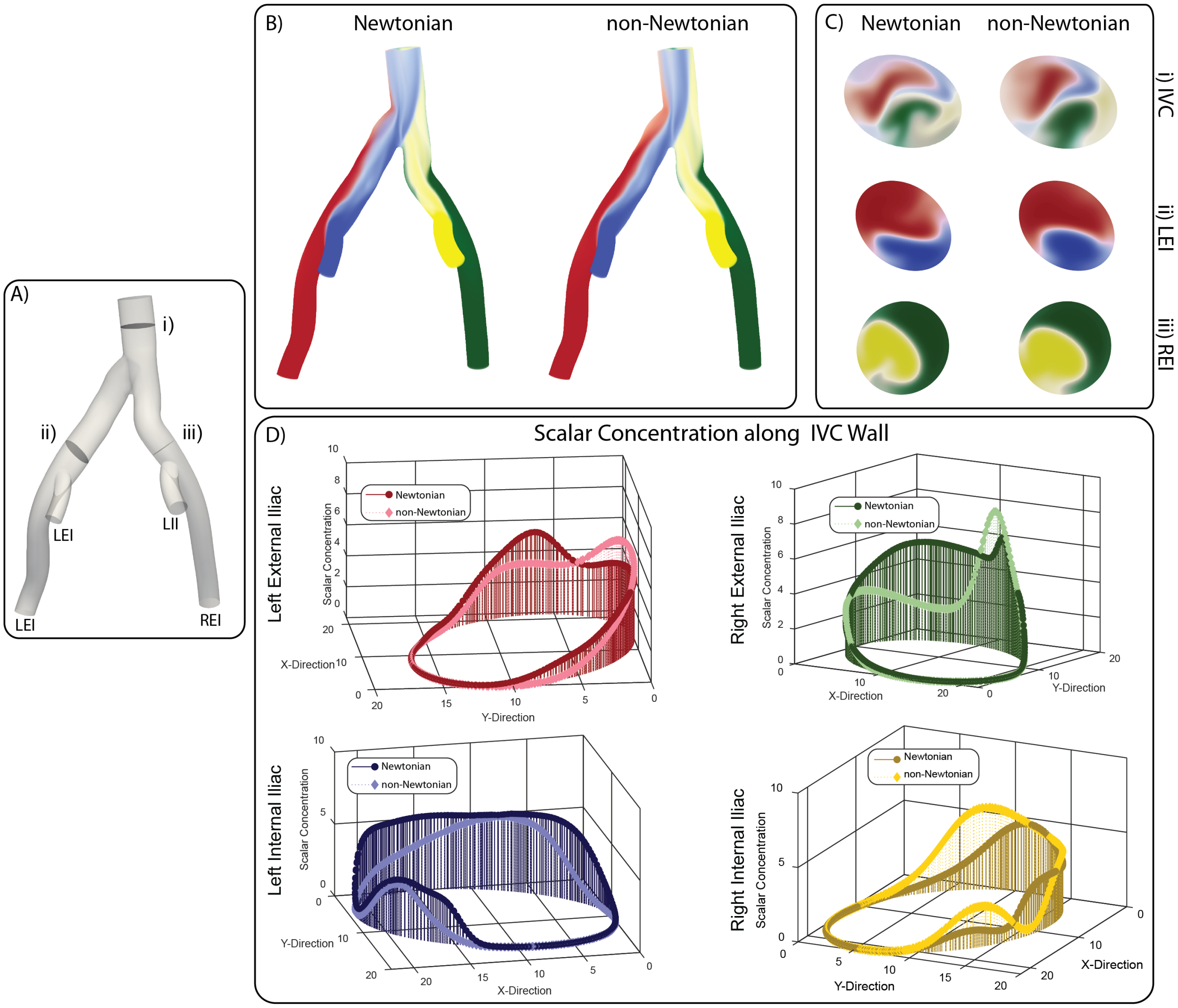

Figure 3.11: (A) Computational domain highlighting three locations (i-iii). (B) Volume rendering of the four scalar scalar fields for the Newtonian and Carreau-Yasuda simulations. (C) Concentration contours of the four scalar fields at locations i-iii. (D) Scalar concentration along the IVC wall for Newtonian and Carreau-Yasuda simulations for each scalar species. All results are shown for time $t = 3.2$s.

ical species and proteins[33,60,71,110,130]. Modeling mass transport in cardiovascular systems presents numerical challenges due to the inherently complex and time-dependent flow patterns and vessel geometries. This complexity is further compounded by the large range of Péclet numbers found in cardiovascular flows. The primary aim of this work is to present a stabilized computational framework to study 3D, transient cardiovascular mass transport problems. This includes the identification of appropriate boundary conditions that allow for physiologic flow reversal as well as use of stabilization techniques to avoid spurious numerical oscillations in the computed concentration field.

A number of previous computational studies have employed modeling assumptions or simplifications that are difficult to justify in cardiovascular mass transport problems. These have included unphysiologically large values of diffusion coefficients to lower the Péclet number[16,50]; unrealistic extension of model branches to regularize velocity profiles near outlet faces[8,57]; and the prescription of arbitrary concentration or flux values at outlet boundaries[8,57] with a significant influence on the computed solution in regions of interest. These simplifications, always resulting from limitations in the numerical approach, severely limit the applicability of such models for general cardiovascular mass transport studies.

The computational framework for cardiovascular mass transport presented in this work has three salient features. Firstly, we have presented a backflow stabilization strategy to obtain stable numerical solutions in the presence of flow reversal at outlet boundaries. Secondly, we have introduced a 'consistent flux boundary condition' and have demonstrated its superiority over the typically used zero diffusive flux boundary condition in preserving the local physics of the numerical solution, particularly in cases of low Péclet numbers. Lastly, this framework employs SUPG and DC formulations to resolve steep concentration gradients in mass transport characterized by high Péclet numbers.

We have demonstrated the application of this framework in two different sets of geometries. Firstly, we chose idealized geometries with steady flow conditions to allow for a clear interpretation of different numerical challenges and to illustrate the efficacy of the various stabilization techniques reported in this work. The second set of application examples considered a patient-specific model of a human aortic aneurysm under pulsatile flow conditions. This example illustrates the applicability of the framework to complex cardiovascular mass transport problems.

Figure 3.3(A) demonstrates the issue of numerical divergence in simulations with backflow at Neumann boundaries. The problem was set up in such a way that even under steady flow conditions, flow reversal occurred on some fraction of the outlet boundaries (Γ_N^{in}). For a diffusion coefficient $D = 10^{-2}$ mm^2/s and Péclet number of $\text{Pe}_{\text{mean}} = 2.5 \times 10^4$, simulations diverged if no backflow stabilization was utilized. Following concepts used for stabilization of outlet boundaries in flow problems, the backflow stabilization condition adds an advective component to the diffusive boundary flux. When running experiments with lower Péclet numbers (i.e., with larger diffusion coefficients), stable solutions can be obtained even without any backflow stabilization. This is expected since the contribution of the advective flux to the total flux decreases with smaller Péclet numbers. This observation explains that previous studies could report stable solutions without using stabilized outlet boundary conditions for mass transport problems[16,50]. However, an artificial increase in diffusion coefficient changes the physics of the problem entirely.

In Section 3.3.1.2, we studied the performance of the "consistent flux" versus standard zero diffusive flux boundary conditions in a short cylindrical geometry, and compared the results against reference solutions obtained in an extended cylindrical geometry. Simulations demonstrated the superiority of the consistent flux boundary condition in preserving the local accuracy of the solution near the outlet boundary (Figure 3.4), albeit a marginal difference relative to the reference truth solution are still noticeable. Important to note, the diffusion coefficient used in this example was increased to $D = 10^2$ mm^2/s, leading to a smaller Péclet number of $\text{Pe}_{\text{mean}} = 10$. Simulations run with larger Péclet numbers show smaller differences between consistent and zero flux boundary condition results.

In Section 3.3.1.3, the performance of the DC operator to stabilize oscillations in the wavefront of the scalar field for high Péclet numbers was studied. A diffusion coefficient $D = 10^{-2}$ mm^2/s, rendering a Péclet number $\text{Pe} = 10^4$ was considered. Figure 3.5 illustrates that without the DC operator, overshoot/undershoot in the numerical solution occurs at the wavefront, resulting in unphysical negative scalar concentrations ($-0.98\,\text{mol/mm}^3$) as well as in concentration values higher than those imposed at the inlet ($11.92\,\text{mol/mm}^3$). The DC operator eliminates the spurious oscillations, rendering a smooth solution without unphysical negative concentrations.

Lastly, in Section 3.3.3 we applied computational framework for cardiovascular mass transport to further study the effects on non-Newtonian rheology on cardiovascular transport. A comparative scalar mass transport analysis was performed using scalar backflow stabilization, the consistent flux boundary condition, and Discontinuity-Capturing in both the arterial and venous model for both Newtonian and Carreau-Yasuda viscosity. Here, biochemical scalar species of interest were represented via respective Eulerian concentration fields governed by the scalar advection-diffusion equations. In our analyses, we injected scalar species with prescribed concentrations through the inlet(s) of our computational domain and solved scalar mass transport equations to obtain the spatio-temporal distribution of these species. Our analyses revealed significant differences in the concentration fields between the Newtonian and Carreau-Yasuda case for both the arterial and the venous models. These differences were observed both in the bulk domain and perhaps more importantly, in the near-wall region, again highlighting the importance of considering accurate blood rheological models to obtain accurate assessment of mass transport via computational cardiovascular analyses.

The performance of the three formulations was then tested in a patient-specific aortic aneurysm geometry under pulsatile conditions, see Section 3.3.2. The backflow stabilization produced stable results in the presence of significant flow reversal (Figure 3.7). The consistent flux boundary condition showed substantial differences in scalar concentration profiles compared to the zero diffusive flux boundary condition, specifically in regions near the outlet boundary, see Figure 3.8. Lastly, the DC operator rendered smooth concentration profiles near the wavefront of the solution for high Péclet number transport, see Figure 3.9.

While the different formulations presented in this work provide a set of robust tools to enable simulation of cardiovascular mass transport under realistic geometries, flow, and Péclet number conditions, further developments are needed. Future work includes validation of the proposed framework with *in vitro* dye perfusion experiments and *in vivo* patient-specific angiography studies. Similarly to the reduced-order models widely adopted for cardiovascular flow problems[5,134,135], it is critically important to develop reduced-order models of mass transport for the proximal and distal portions of the vascular system not included in the 3D geometric model. This is particularly important when dealing with closed-loop models and simulations involving reaction.

The DC scheme introduces a non-linear term in the weak form of the problem. Although an increase in computational cost was expected, no increase was observed in simulations run with the DC operator. This expense can be mitigated by the use of a time-lagging DC scheme[26]. We remark, however, that in the presence of nonlinearity (e.g. in source terms), the scalar advection-diffusion problem would be nonlinear regardless of the DC scheme and computational cost will not be significantly different with and without the DC operator.

CHAPTER IV

Arbitrary Scalar Reaction-Advection-Diffusion (ARAD) Framework for the Computational Modeling of Thrombosis in Cardiovascular Hemodynamics

4.1 Introduction

Thrombosis is a process whereby a blood clot forms *in situ* within a vessel and impedes flow. Although necessary to maintain hemostasis, often the human thrombotic system becomes unstable leading to scenarios of thrombosis and subsequent diseases such as myocardial infarction, stroke, pulmonary embolism, and deep vein thrombosis (DVT). Thrombosis initiation involves the complex interplay between hemodynamics and biochemical reactions that lead to the formation of a blood clot.

The development of multiscale computational models integrating both complex hemodynamics and complex biochemical reactions may provide valuable tools for thrombosis research[150]. However, prior computational models have focused on either the complex biochemistry[23,61] or flow dynamics[36] involved in thrombosis formation, thereby limiting the ability to investigate their interplay. This limitation is primarily due to the numerical challenges associated with modeling thrombosis. In particular, thrombosis initiation involves: highly nonlinear biochemical reactions, high Péclet number flows resulting from the extremely low diffusivities of coagulation factors and platelets (10^{-10} m^2/s), complex 3-D hemodynamics, and near wall transport. Furthermore, it has often been considered computationally cost prohibitive to run the full coagulation cascade in patient-specific 3D models with realistic cardiovascular hemodynamics[103].

To circumvent these numerical challenges various groups have resorted to non-physiologic simplifications. For example, groups have employed highly complex nonlinear reaction models but either simplified geometries (i.e. 2D or 3D cylindrical domains)[15,81] or simplified flow fields (i.e. steady and/or parabolic flow)[81]. Other groups have modeled thrombin formation in complex 2 or 3D geometries but with either reduced or phenomenological reaction models[103,104] or with non-physiologic changes to the reaction parameters[15]. Examples include increasing the diffusivity values of the coagulation factors by multiple orders of magnitude[15,127] or using inconsistent stabilization methods such as additional isotropic diffusion to avoid spurious oscillations[15] in the solution field (i.e. negative concentration values). Therefore, there is a need to develop a flexible computational interface that integrates state of the art patient-specific hemodynamics with sophisticated biochemical reaction models, and appropriate numeric stabilization.

In this work, an arbitrary reaction-advection-diffusion (ARAD) interface was developed for the rapid prototyping of nonlinear reaction models in cardiovascular mass transport simulations. A novel aspect of the ARAD framework is the ability to run large parallel patient-specific mass transport simulations with an arbitrary number of scalar species (i.e. up to 20) with arbitrary nonlinear reaction terms. The ARAD framework takes advantage of a Python interface for easy prototyping of the reaction models, without having to alter the underlying C++/FORTRAN finite element (FE) flow solver.

The proposed ARAD framework leverages previous advancements in both hemodynamic modeling via the open-source hemodynamics software CRIMSON (www.crimson.software)[6] and methods for stabilization of scalar mass transport problems[87] presented in Chapter III. CRIMSON has an active community of users which is substantial and constantly growing and has been widely tested by both members of the research group and outside users.

The structure of this Chapter is as follows. In the Materials and Methods section, an overview of the governing equations, nonlinear reaction models, methods of reaction model implementation, and best practices for thrombosis modeling are provided. In the Results section a comparison of the performance of the hardcoded and ARAD implementations are first compared. The flexibility of this framework is next illustrated by prototyping established coagulation models ($4-, 7-$, and 18-species models) within a 3D cylindrical domain. Finally, the 18-species coagulation model is investigated in both an idealized and patient-specific model of an aortic abdominal aneurysm (AAA).

4.2 Materials and methods

4.2.1 Fluid Dynamics Model

4.2.1.1 Strong Form

The strong form of the governing equations for an incompressible fluid in a 3D bounded domain $\Omega \subset \mathbf{R}^3$ is given as

$$\rho\left(\frac{\partial \mathbf{u}}{\partial t} + \mathbf{u} \cdot \nabla \mathbf{u}\right) = -\nabla p + \nabla \cdot \tau(\mathbf{u}) + \mathbf{f}, \tag{4.1}$$

$$\nabla \cdot \mathbf{u} = 0, \tag{4.2}$$

where ρ is the fluid density, t is the time, $\mathbf{u}$ is the solenoidal velocity field, p is pressure, $\mathbf{f}$ is the external body force per unit volume (set to zero), and τ is the viscous stress tensor. For a Newtonian, incompressible fluid, τ is defined as:

$$\tau = \mu\left(\nabla \mathbf{u} + \nabla \mathbf{u}^T\right), \tag{4.3}$$

where μ is the Newtonian viscosity.

4.2.1.2 Weak Form

For the solution and test function spaces $S,\ W,$ and P, Eqs. 2.1 and 2.2 yield the following weak form:

$$\int\limits_{\Omega}\{\mathbf{w}\cdot(\rho\mathbf{u}_{,t}+\rho\mathbf{u}\cdot\nabla\mathbf{u}-\mathbf{f})+\nabla\mathbf{w}:(-p\mathbf{I}+\tau)-\nabla q\cdot\mathbf{u}\}d\mathbf{V}$$

$$+\int\limits_{\Gamma_g} q\mathbf{u}\cdot\mathbf{n}dA-\int\limits_{\Gamma_h}\{\mathbf{w}\cdot\mathbf{t}^h\}dA+\int\limits_{\Gamma_h} q\mathbf{u}\cdot\mathbf{n}dA+\text{Stab}=0 \tag{4.4}$$

$$\forall\boldsymbol{x}\in\Omega,\forall t\in[0,T], \tag{4.5}$$

where $w\in\mathcal{W}$ and $q\in\mathcal{P}$ are test functions for the momentum and mass conservation equations, respectively. Ω represents the 3-dimensional computational domain, Γ_g is a Dirichlet boundary (typically the inflow) where the test function $\mathbf{w}$ vanishes and Γ_h is a Neumann boundary where a traction

$$\mathbf{t}^h=(-p\mathbf{I}+\tau)\cdot\mathbf{n}=\mathbf{h}\left(\mathbf{u},p,\boldsymbol{x},t\right) \tag{4.6}$$

is prescribed. The standard Galerkin method exhibits instabilities for advection dominated flows and in the diffusion dominated limit for equal order interpolation of velocity and pressure. The term “Stab” refers to the stabilization terms[131,145] of the Streamline upwind Petrov–Galerkin (SUPG) formulation utilized in our in-house software CRIMSON (www.crimson.software)[6]. This stabilization allows us to employ equal order interpolation for velocity and pressure. In the current work, we employ tetrahedral elements supporting Lagrange polynomial basis functions of order one for both velocity and pressure. For time integration, we employ the generalized-α method[29].

4.2.2 Reaction-Advection-Diffusion (RAD) Model

4.2.2.1 Strong Form

The strong form of the governing equation for mass transport in a 3D bounded domain $\Omega \subset \mathbb{R}^3$ is given as

$$\frac{\partial c_i}{\partial t} + \mathbf{u} \cdot \nabla c_i - \nabla \cdot (D_i \nabla c_i) = r_i \qquad \text{in} \quad \Omega \qquad \text{for } i = 1, ..., \text{number of scalars}, \tag{4.7}$$

where $i = 1,\ ...,$ number of scalars and c_i, D_i, and r_i refer to the concentration, diffusion coefficient, reaction term(s) for the scalar i.

4.2.2.2 Weak Form

The Galerkin weak form for the scalar advection-diffusion problem governed by Eq. 4.7: is as follows: find $c \in H^1(\Omega)$ such that

$$\int\limits_{\Omega} \left[\delta_c \frac{\partial c_i}{\partial t} + \delta_c \mathbf{u} \cdot \nabla c_i + \nabla \delta_c \cdot D_i \nabla c_i\right] \mathrm{d}V - \int\limits_{\Gamma_N} \delta_c \left(D_i \nabla c_i\right) \cdot \mathbf{n} \mathrm{d}A = \int\limits_{\Omega} \delta_c r_i \mathrm{d}V \qquad \forall \delta_c \in H_0^1(\Omega) \tag{4.8}$$

where δ_c is a weighting function, $H^1(\Omega)$ is a (solution) space of once-differentiable functions satisfying the Dirichlet boundary conditions on Γ_D, and $H_0^1(\Omega)$ is a (weighting) space of once-differentiable functions vanishing on the Dirichlet boundary Γ_D. Since cardiovascular mass transport problems are characterized by high Péclet number flows, we utilize a SUPG and Discontinuity-Capturing (DC) stabilized finite element formulation[20].

Details of the scalar RAD formulation used in this paper, including background on stabilization and boundary conditions, can be found in Chapter III.

4.2.3 Reaction Terms for Biochemical Models

The RAD equations (Eq. 4.7) model the transport of any number of scalar species via advection, diffusion, and reaction. Various cardiovascular diseases exist that involve the reaction of a number biochemical species such as atherosclerosis, thrombosis, or oxidation. These biochemical reactions can be modeled using the well-mixed assumption where the effects of spatial transport are ignored (i.e. "batch reactor"). In well-mixed systems chemical concentrations are considered as a function of time only can be described mathematically by a system of ordinary differential equations (ODEs)[16,61] as in Eq. 4.9,

$$\begin{aligned}
\frac{dc_1}{dt} &= k_1 c_1 c_2 c_3 + k_2 c_2 - k_5 c_3 \\
\frac{dc_2}{dt} &= -k_1 c_1 c_2 c_3 - k_2 c_1 c_2 - k_4 c_1 \\
\frac{dc_3}{dt} &= k_3 c_2 c_3 + k_4 c_1 - k_5 c_3,
\end{aligned} \tag{4.9}$$

where c_i represents a scalar species involved in the chemical pathway and the coefficients k_i can be either positive (production) or negative (depletion).

Conversely, in cardiovascular flows, including flows in abdominal aortic aneurysms (AAAs), the concentration of chemical species vary in both time and space, leading to a 3-dimensional and time dependent problem. This can be solved by coupling the Navier-Stokes equations (Eq. 4.1) to the time-dependent RAD equations (Eq. 4.7) where i refers to the number of scalar species of interest. R_i represents the reaction term for each scalar species and can take the form of the experimentally obtained ordinary differential equation models (see Eq. 4.9). For systems where there is more than one scalar species ($i > 1$) the system of RAD equations will be solved using a "staggered" finite element modeling (FEM) approach.

Although the RAD equations can be applied to study numerous biochemical diseases such as atherosclerosis, cholesterol metabolism and lipid-lowering drugs, among others, the main application of interest in this work is thrombosis initiation. The coagulation cascade is a series of subsequent biochemical reactions, where enzymes or proteins known as clotting factors undergo a series of nonlinear biochemical reactions leading to thrombin generation. The coagulation cascade is triggered at sites of endothelial damage, i.e., when extravascular tissue factor (TF), which is present under the endothelial layer, binds to blood-borne factor VIIa. In this investigation, our numerical examples will focus on modeling thrombin formation via the coagulation cascade in both idealized and patient-specific cardiovascular models.

4.2.4 Thrombin Generation Models

Numerous models of thrombin generation exist, varying from highly phenomenological to mechanistic. In this investigation three models of thrombin generation were implemented varying in complexity and size, see Fig. 4.1.

The simplest model, developed by Papadopoulos et al.[103], consists of 4 scalar species: resting platelets (RP), activated platelets (AP), prothrombin (II) and thrombin (IIa) and 5 rate constants (k coefficients), see Fig. 4.1(A) where the concentration of prothrombin and thrombin is shown over time. This 4-ODE model is entirely phenomenological but able to match patient-specific laboratory data for thrombin generation[103]. The model is strengthened by its low computational cost and ease of implementation. Limitations include ignoring key clotting factors, such as factors V, X, VIIa, etc., and the use of a step-function for the rate constant describing platelet activation by thrombin $k_{\mathrm{AP}}^{\mathrm{IIa}}$.

The next thrombin generation modeled considered, Fig. 4.1(B), was developed by Hansen et al.[59] and consists of 7 scalar species and 4 rate constants. Hansen and others introduced an automated framework to generate reduced-order models of blood coagulation and compared their performance to a benchmark 34-species model[61] for a range of tissue factor concentrations, including those not included in the optimization process[59]. This model balances computational cost and inclusion of species of interest but it still limited by its over-simplicity.

The last ODE model examined, Fig. 4.1(C), was developed by Jones and Mann[70], empir-

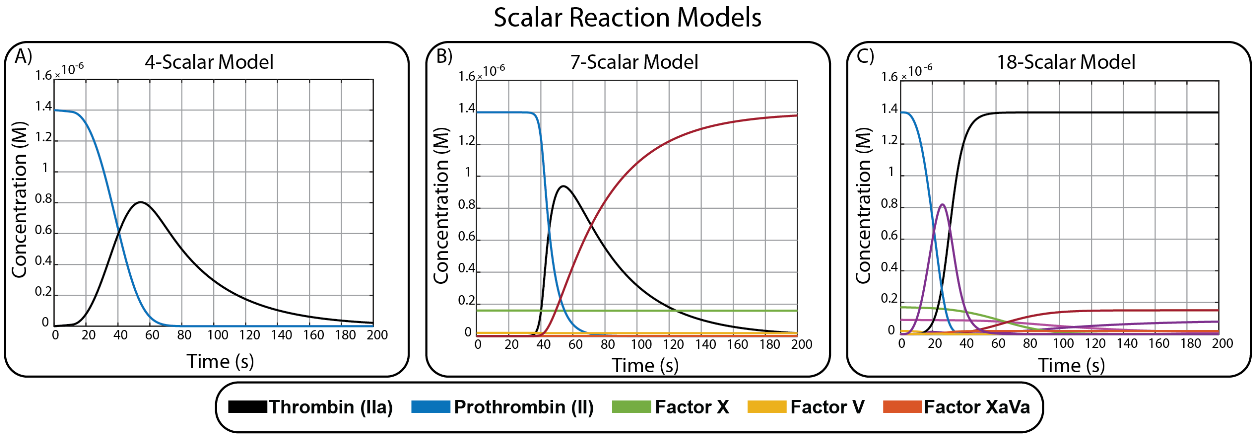

Figure 4.1: ODE Thrombin Generation Models

ically supported by Lawson and team[78], and used extensively thereafter[16,127]. It consists of 18 scalar species, 19 rate constants and 16 total chemical reactions. The model involves both plasma-phase and surface-bound enzymes and zymogens. This model allows for a detailed analysis of the coagulation cascade at the expense of higher computational cost.

A notable difference between the 18-species reaction model compared to the 4- and 7-species model is the lack of inhibitors in the reaction model. In Fig. 4.1(A-C) thrombin concentration is denoted by the black curves. For the 18-species model, Fig. 4.1(C), the thrombin concentration curve peaks at approximately 40s and plateaus to a constant value as opposed to Fig. 4.1(A,B) where thrombin peaks around 50s and then falls back to a zero-concentration (i.e. bell curve shape). Despite more recent models including thrombin inhibitors (i.e. tissue factor pathway inhibitor), it has been accepted that these inhibitors do not function in AAAs and can therefore be ignored[16].

The ordinary differential equations, rate constants, and initial conditions used for the 4, 7, and 18-species reactions models can be found in Appendix B.

4.2.5 Implementation of nonlinear Reaction Terms

The scalar reaction-advection-diffusion equations were implemented within the finite element solver CRIMSON[6] using two separate approaches for the reactive transport models. The simplest 4-scalar ODE model was implemented using both a hardcoded FORTRAN approach for the nonlinear reaction terms and using the proposed ARAD framework.

4.2.5.1 Hardcoded FORTRAN Implementation

The conventional FORTRAN implementation corresponds to the previously reported scalar advection-diffusion formulation[87]. This involves a standard finite element implementation where contributions to the stiffness matrix and residual vector are assembled within a Gaussian quadrature loop. This necessitates the implementation of the reaction terms and their gradients for each scalar species. Consequently, a change in the reaction model requires modifications to the relevant code sections (corresponding to the calculation of contributions to the stiffness matrix and residual vector), followed by compilation of the entire CRIMSON source code. While this approach is robust and is typical in finite element codes, it requires user familiarity with coding and compiling of source codes.

4.2.5.2 Arbitrary Reaction-Advection-Diffusion (ARAD) Framework

Figure 4.2 describes the developed ARAD framework that enables flexible run time specification of nonlinear reaction models for an arbitrary number of scalars species. Currently, the number of scalar species can be anywhere from $1 - 20$ scalar species.

Under the finite element framework, reactions between scalar species are realized via the computation of reaction term relationships between scalar concentrations at every node of the finite element mesh. The ARAD system has been developed to allow for run-time specification of such reaction terms (our *Flexibility Goal*) without adding significant computational cost when compared to an inflexible implementation in pure FORTRAN or C++ (our *Performance Goal*). These goals are addressed as follows. 1) The reaction terms (and their derivatives, which are required for insertion in the Jacobian matrix for the nonlinear finite element problem) are specified in Python, in a user-editable Python file included in the simulation working directory, read by the CRIMSON flowsolver at run-time. This leverages the fact that Python is interpreted rather than compiled. This addresses the *Flexibility Goal.*

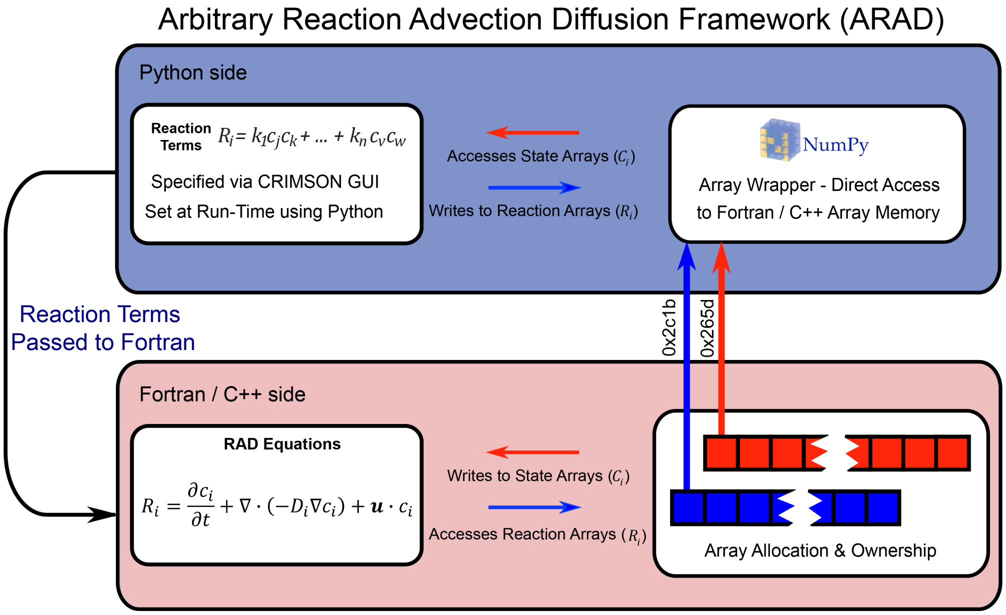

Figure 4.2: ARAD Framework

Secondly, data arrays comprising the scalar concentrations at the mesh nodes are created and managed by FORTRAN, but pointers to these arrays, contiguous in memory, are passed to Python, where they are wrapped into standard Python NumPy arrays. This is done in-place, avoiding costly in-memory copies on every time-step; from here they can be manipulated by the user-specified Python code. A similar pointer-wrapping mechanism is used to return the computed reaction terms from Python to FORTRAN, via a FORTRAN-owned return value array. Manipulations within Python are performed using NumPy array operations, which are typically wrappers for underlying efficient C implementations. This addresses the *Performance Goal*.

In addition to these goals, a number of descriptors for the scalar problem - including scalar diffusivities and the order in which each scalar RAD problem should be solved relative to the others - are specified in the same Python file as the reaction terms. This avoids spreading the specification of a particular scalar problem across multiple files, and makes such specifications easily interchangeable.

Ultimately, this ARAD design enables run-time specification of arbitrary reaction models that can be used to describe a broad range of biochemical cardiovascular diseases or additional applications, at minimal additional computational cost.

4.2.6 Reaction-Advection-Diffusion Modeling Best Practices

Often times the important physics of various cardiovascular biochemical diseases, such as atherosclerosis or thrombosis, are confined to thin near-wall concentration boundary layers[45,58]. These problems are typically characterized by high Péclet numbers, low diffusivities, and small nanomolar concentration values often leading to numerical instabilities. In this investigation we propose a set of practices to enable the appropriate and accurate modeling of biochemical reactions and transport from the vessel wall.

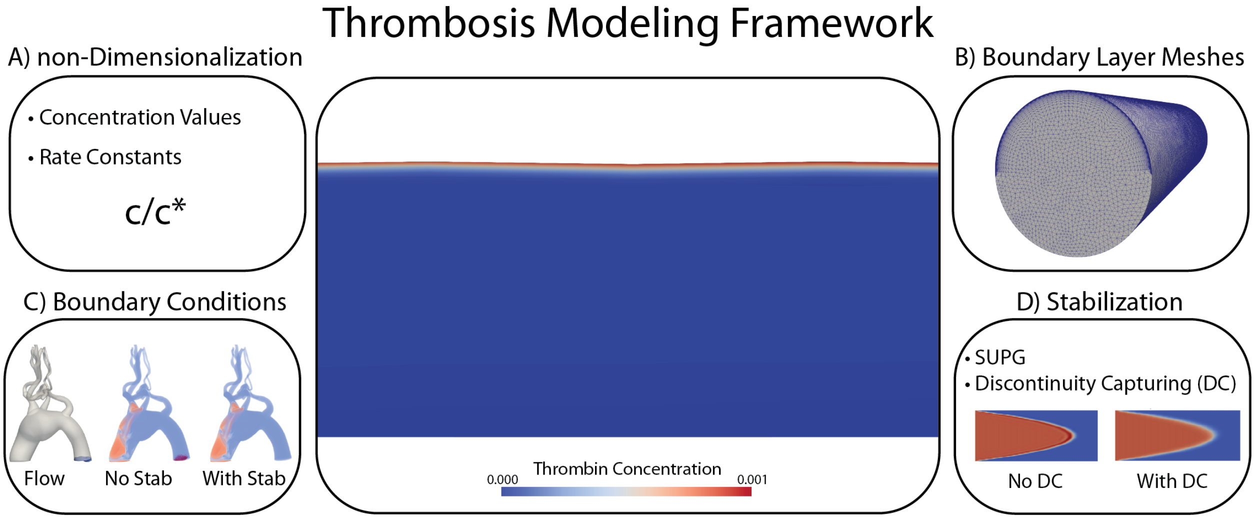

Figure 4.3: The proposed methods of best practices used in the developed ARAD Framework. A) Nondimensionalization, B) boundary layer meshes, C) outflow boundary conditions that enable the investigation of mass transport in transient flows, and D) numerical stabilization of high Péclet number flows

Figure 4.2 outlines the methods of best practice used in this investigation. Briefly, boundary layer meshes were used to capture the near-wall transport at the site of thrombin generation. The meshes consisted of boundary layer elements near the cylinder wall and isotropic elements in the cylinder interior, see Figure 4.2(B). In all cases a sufficient number of boundary-layers were added to ensure the boundary elements smoothly transitioned into the interior elements. SUPG and DC stabilization of the scalar problem were used to prevent spurious oscillations in the scalar field which often results from high Péclet numbers. In addition, backflow stabilization was applied to enable solving scalar reaction-advection-diffusion problems in transient cardiovascular flows. Lastly, thrombin formation in particular, involves extremely small concentration values on the order of 10^{-9}. Numerically it can be challenging to solve problems on such small scales. Similarly to previous investigations[4], nondimensionalization was used to aid the numerical scheme.

Overall, these four practices enabled the simulation of realistic values of diffusion, coagulation factors, and hemodynamic metrics such as Reynolds number within the ARAD framework.

4.3 Results

In this section, we present numerical results to illustrate the suitability of the proposed computational framework. The following applies to all the numerical examples presented in this section:

- A flow solution is first obtained by solving the stabilized Navier-Stokes equations using the cardiovascular hemodynamics modeling environment, CRIMSON (www.crimson.software)[6].
- Blood is modeled as a Newtonian fluid with a density of 1060 $\mathrm{kg/m^3}$ and a dynamic viscosity of 0.004 $\mathrm{Pa \cdot s}$.
- All walls are modeled as rigid (i.e., homogeneous Dirichlet boundary conditions for the velocity field).

4.3.1 Scalability Tests

In this example, we compare the scalability of the FORTRAN and ARAD nonlinear reaction implementations for the 4-scalar reaction model in an idealized cylindrical domain with a diameter $d = 1.0$ mm and length $l_1 = 10$ mm. Steady flow field solutions were first obtained by prescribing a constant flow rate of 2.0 L/min, mapped to a parabolic velocity profile resulting in a mean velocity of $v_{max} = 500$ mm/s and a mean Reynolds number of $Re_{mean} = 33.125$. A zero traction boundary condition was applied at the outlet face.

For the RAD transport problem, a constant value of diffusivity (D) was adopted, $D = 1.0$ mm^2/s, resulting in a Péclet number of $Pe_{mean} = 1.25$. A patch on the cylinder wall with a uniform Dirichlet concentration of activated platelets was used to initiate thrombin formation. Simulations were run using a constant time-step size of $\Delta t = 10^{-4}$ s for both the flow and transport problems. After obtaining a constant flow field, the scalar reaction-advection-diffusion transport problems were run for $10,000$ time steps, corresponding to 1.0 s of physical run time.

Mesh size (millions of elements)	**Number of Cores**	**Elements/Core**
1.0	20	50,000
1.0	40	25,000
1.0	60	16,667
1.0	80	12,500
1.0	100	10,000
1.0	120	8,333

Table 4.1: Strong Scalability.

All scalability tests were run using the High-Performance Computer (HPC) cluster 'ConFlux' at the University of Michigan. Tables 4.1 and 4.2 outline the scalability tests performed.

Briefly, for the strong scaling tests the cylindrical domain was discretized uniformly using linear tetrahedral elements with a total mesh size of 1.0 million elements and 0.18 million nodes, the mesh size was held constant for all simulations. The number of cores varied from 20 to 120 cores for a total of 6 meshes and 12 simulations: 6 with the FORTRAN implementation and 6 with the ARAD implementation.

Fig. 4.4(A) shows results for the strong scalability tests. Both the FORTRAN and ARAD implementations performed well over the range of HPC cores tested, with the slopes

Mesh size (millions of elements)	**Number of Cores**	**Elements/Core**
0.25	5	50,000
0.5	10	50,000
1.0	20	50,000
2.0	40	50,000
4.0	80	50,000
8.0	160	50,000

Table 4.2: Weak Scalability.

of approximately −1.0 for both implementations (FORTRAN and ARAD).

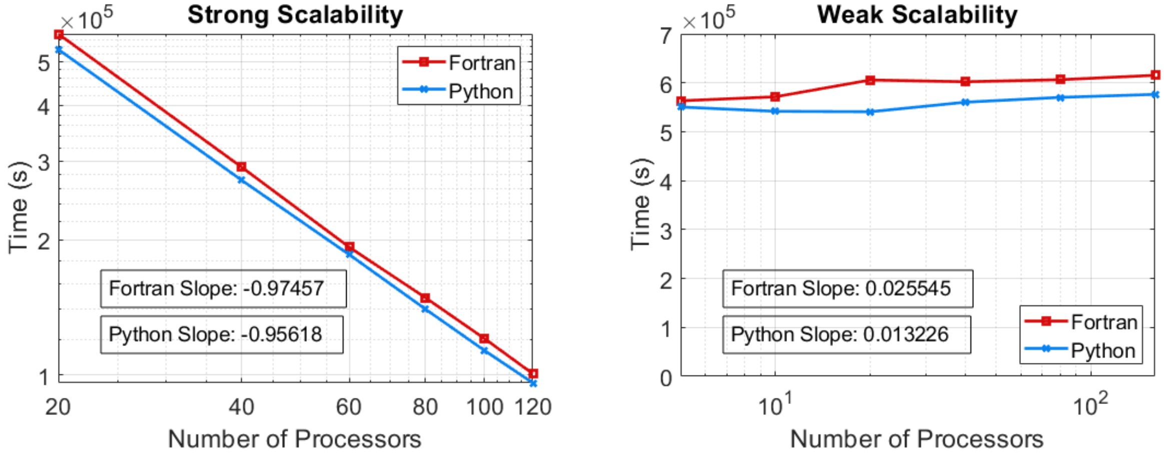

Figure 4.4: (A) Strong scalability and (B) weak scalability for FORTRAN (red) and ARAD Python (blue) implementations

The same cylindrical domain was used for the weak scalability tests. Both the mesh size ($250,000 - 8,000,000$ cores) and the number of cores ($5 - 160$ elements) were varied to maintain the same constant ratio of elements per core (elements/core $= 50,000$). Again 12 simulations were performed: 6 with the FORTRAN implementation and 6 with the ARAD implementation.

Fig. 4.4(B) shows results from the weak scalability tests. A slope of zero would indicate ideal performance, corresponding to no increase in computational cost despite the increase in the number of cores and communication time. For both the FORTRAN and ARAD implementations the slopes are approximately zero (FORTRAN slope ≈ 0.03 and ARAD slope ≈ 0.01).

Overall, both strong and weak scalability tests indicated good performance for both the FORTRAN and ARAD implementations despite Python being an interpreted language.

4.3.2 Prototyping reaction models in a cylinder

To illustrate the overall flexibility of the developed ARAD framework the three reaction models of thrombin generation previously discussed (see Figure 4.1) were implemented in a cylindrical domain. The idealized cylindrical domain considered has a diameter $d = 13.4$ mm and length $l_1 = 50$ mm. Steady flow field solutions were obtained by prescribing a constant flow rate of 0.395 L/min, mapped to a parabolic velocity profile at the inlet face, resulting in a mean velocity of $\mathrm{v}_{\mathrm{max}} = 49$ mm/s and a mean Reynolds number of $\mathrm{Re}_{\mathrm{mean}} = 175.15$. A zero traction boundary condition was applied at the outlet face.

For the scalar reaction-advection-diffusion transport problem, constant values of diffusivity were adopted for all scalar species. $D = 2.5 \text{ x } 10^{-5}$ mm^2/s was prescribed for both resting and activated platelets and $D = 5 \text{ x } 10^{-5}$ mm^2/s was prescribed for all coagulation factors[81]. For each reaction model (4, 7, and 18) chemical species' concentrations at the inlet were set equal to the initial values taken from literature (see Appendix B for parameters values and reaction terms). The exception for the 4 scalar model was activated platelets. At the site of subendothelial exposure (red wall patch) 5% of platelets were assigned to be activated to initiate thrombin formation. The exception for the 7- and 18-species models was TF and TF:VIIa, respectively. Both were set to 1.0 nM on the wall patch to simulate subendothelial exposure.

Simulations were run using a constant time-step size of $\Delta t = 2 \text{ x } 10^{-4}$ s for both the flow and transport equations. After obtaining a constant flow field, the scalar reaction-advection-diffusion transport problems were run for $220,000$ time steps corresponding to

44 s of physical time.

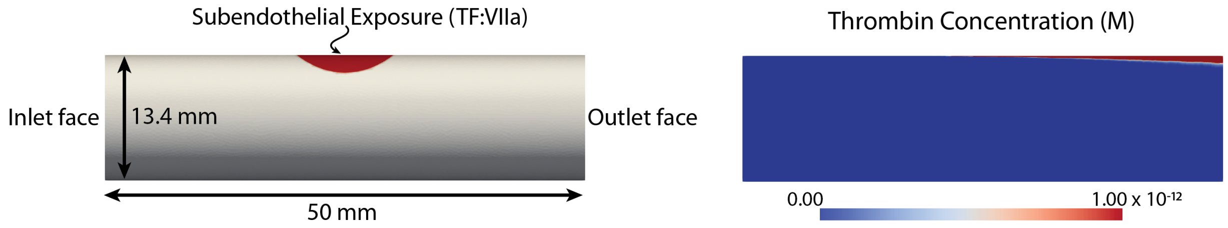

Figure 4.5: (Left) Idealized cylindrical geometry with exposed TF:VIIa representing subendothelial exposure highlighted in red. (Right) Thrombin concentration at t = 44 s in the cylindrical domain.

Figure 4.5(left) shows the computational domain with the associated dimensions. For brevity, results for the scalar reaction-advection-diffusion transport equations are presented only for the 18-species reaction model only. The red patch in the center of the domain (l = 25 mm) represents the site of thrombosis initiation by TF:VIIa, see Figure 4.5(left). The mean Péclet number is $\mathrm{Pe}_{\mathrm{mean}} = 1.32 \text{ x } 10^7$ for all coagulation factors. Figure 4.5(right) shows concentration contours for thrombin after 44 s. After the initial lag time, a thin boundary layer of thrombin forms at the patch and is transported, mainly via advection, along the wall and eventually, outside of the domain. Over the length of the cylinder the height of the thrombin boundary layer increases slightly due to the increased amount of diffusion over time. Virtually no thrombin is transported to the center of the domain or far from the wall due to the steady parabolic flow profile used in this example.

4.3.3 Idealized AAA

To investigate the effects of transient hemodynamics on thrombin generation and transport the same 18-species reaction model from Jones and Mann[70] was implemented in an idealized abdominal aortic aneurysm geometry. A 3D domain representing an idealized fusiform AAA was created in SolidWorks, see Figure 4.6. Dimensions were chosen according to the 2D axisymmetric AAA from Biasetti et al.[16] and boundary conditions were applied to match Biasetti et al.[14,16]. A periodic flow waveform mapped to a parabolic velocity profile was imposed at the inlet face. At the outlet a prescribed pressure waveform was applied, where $p = p(t)$. Often intraluminal thrombus forms in AAAs along the diseased arterial wall. Therefore, in accordance with Biasetti et al.[16], thrombin generation (subendothelial exposure of TF:VIIa) was modeled at the site of aneurysmal wall expansion.

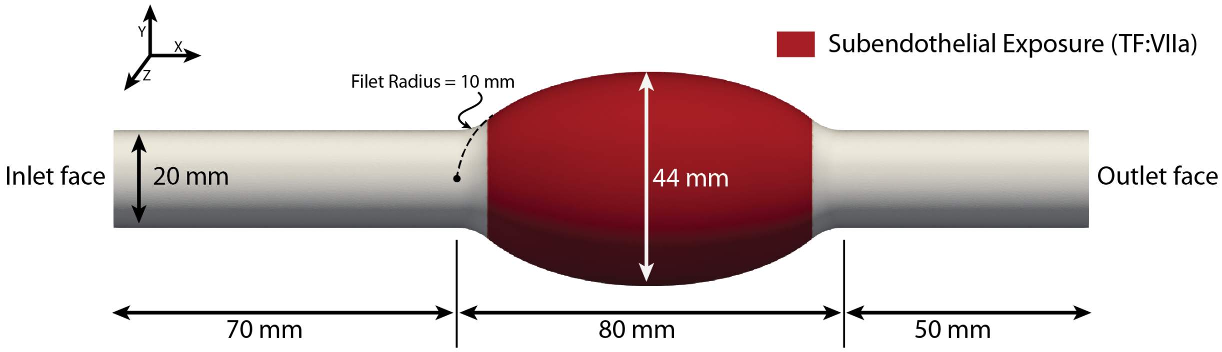

Figure 4.6: Idealized axisymmetric fusiform abdominal aortic aneurysm matching the model reported in Biasetti et al.[16]. The exposed TF:VIIa representing subendothelial exposure is highlighted in red.

Figure 4.6 shows the computational domain with the region of subendothelial exposure (TF:VIIa = 1.0 nM) highlighted in red. The same scalar reaction-advection-diffusion transport boundary and initial conditions and values of diffusivity ($D = 5 \text{ x } 10^{-5}$ mm^2/s) were used as prescribed in the cylindrical example for the 18-species reaction model. Simulations were run using a constant time step size of $\Delta t = 5 \text{ x } 10^{-4}$ s.

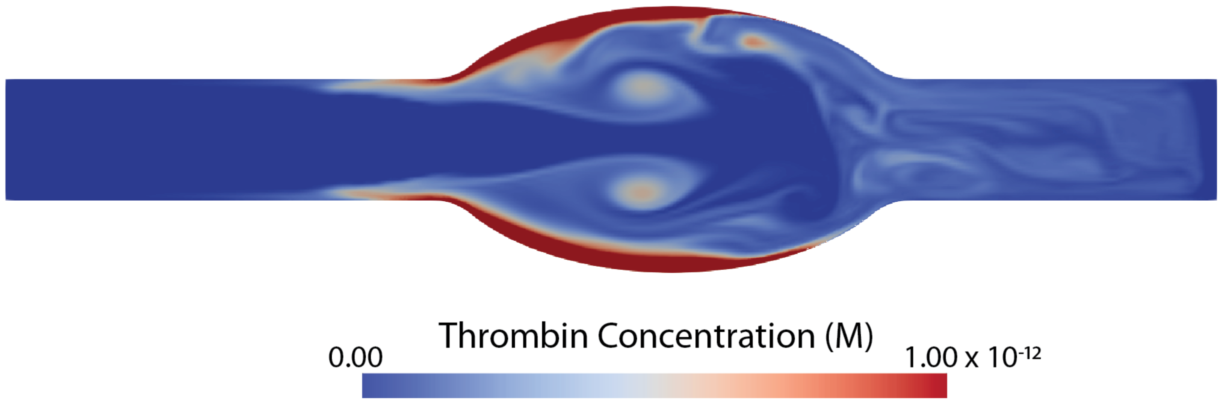

Figure 4.7: Thrombin concentration in the idealized AAA after 19.5 s.

Figure 4.7 shows the thrombin concentration field plotted at the mid-plane of the idealized AAA perpendicular to the Z-direction at time $t = 19.5$ s. The maximum Péclet number at time $t = 19.5$ s is 3.5 x 10^8 for all scalar species. Results illustrate thrombin generation begins at the site of TF:VIIa exposure on the aneurysmal wall. Thrombin is then transported by advection and diffusion to the interior of the domain and recirculates due to the complex periodic flow patterns before leaving the domain. Figure 4.7 shows two vortical structures carrying increased levels of thrombin concentration. These results contrast to the overall simple boundary layer of thrombin formed in the idealized cylinder where both complex geometries and flow patterns are ignored.

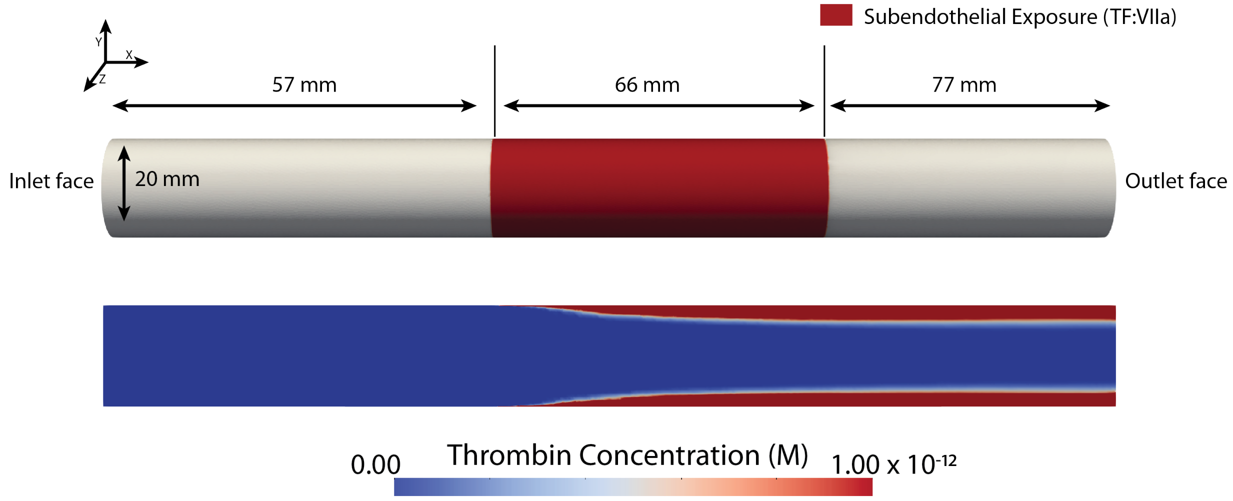

Figure 4.8: (Top) Idealized cylindrical geometry with exposed TF:VIIa representing subendothelial exposure highlighted in red. (Bottom) Thrombin concentration at $t = 20.0$ s in the cylindrical domain.

To compare the effects of complex geometry and hemodynamics on thrombin generation a long cylinder with steady flow was compared to the idealized AAA. Steady flow conditions with a mean Reynolds number corresponding to the idealized AAA simulation were used. The same 18-scalar reaction model, boundary conditions, and diffusivity values were also prescribed. Thrombin formation was initiated using a similar region on the wall as in Figure 4.6. Figure 4.8 shows results at time $t = 20.0$ s. Similar to Figure 4.5, a thin boundary layer is formed on the cylinder wall at the site of subendothelial exposure. Unlike the results in Figure 4.6, the generated thrombin does not recirculate within the domain due to the simple geometry and flow conditions. Due to the larger area of subendothelial exposure, a larger boundary layer of thrombin is formed compared to Figure 4.5. Similar to Figure 4.5 the thrombin that is generated stays near the domain wall before being washed out.

4.3.4 Patient-Specific AAA

Having investigated thrombin formation in three idealized geometries (cylinder and AAA) we now shift our focus to a patient-specific geometry of a human abdominal aortic aneurysm under periodic flow conditions[82]. The AAA geometry was built from magnetic resonance angiography (MRA) image data using custom software[147]. Figure 4.9(A) shows the maximum intensity projection (MIP) of the MRA and Figure 4.9(B) shows the reconstructed computational domain, comprised of the abdominal aorta, the hepatic and splenic arteries, the superior mesenteric artery, the left and right renal arteries, and the left and right internal and external iliac arteries.

The aortic geometry was discretized into 6.5 million linear tetrahedral elements and 1.1 million nodes. A PC-MRI derived periodic flow waveform (with time period $T = 0.769\,\mathrm{s}$) mapped to a parabolic velocity profile was imposed at the aortic inlet. Three-element Windkessel models[135] were prescribed at each outlet face, representing the behavior of the distal vascular beds.

Velocity fields were obtained with a stabilized finite element method using the cardiovascular hemodynamic modeling environment CRIMSON[6]. Cycle-to-cycle periodicity was achieved after running the flow problem under rigid wall assumptions for two cardiac cycles. The same 18-species reaction model was investigated.

Figure 4.6 shows the computational domain with the region of subendothelial exposure

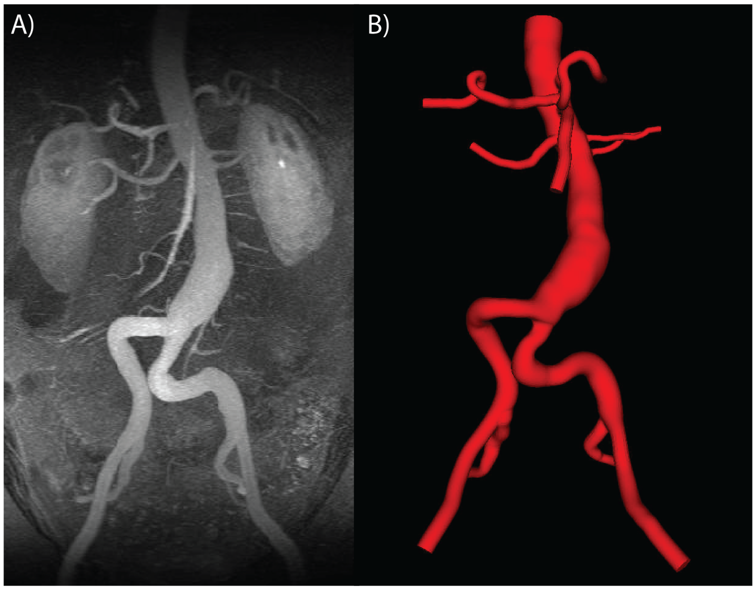

Figure 4.9: The maximum intensity projection (MIP) of the MRA (A) is compared to the 3D computer model (B)[82].

highlighted in red. The same scalar reaction-advection-diffusion transport boundary and initial conditions and values of diffusivity ($D = 5 \text{ x } 10^{-5}$ mm^2/s) were used as prescribed in the cylindrical example for the 18-species reaction model. Simulations were run using a constant time step size of $\Delta t = 2 \text{ x } 10^{-4}$ s.

Figure 4.11 shows a volume rendering of the thrombin concentration field at time $t =$ 16.7 s. The maximum Péclet number is to 1.5x 10^8 for all scalar species. Results illustrate thrombin generation begins at the site of TF:VIIa exposure on the aneurysmal wall is then transported by predominately advection to the interior of the domain. This serves as a proof of concept study to highlight the ability to study patient-specific models of thrombosis using the developed ARAD framework.

4.4 Discussion

RAD problems are of paramount importance in studying cardiovascular pathologies. Diseases such as thrombosis, atherosclerosis, lipid metabolism, and drug delivery are all directly affected by complex biochemical reactions and transient cardiovascular hemodynam-

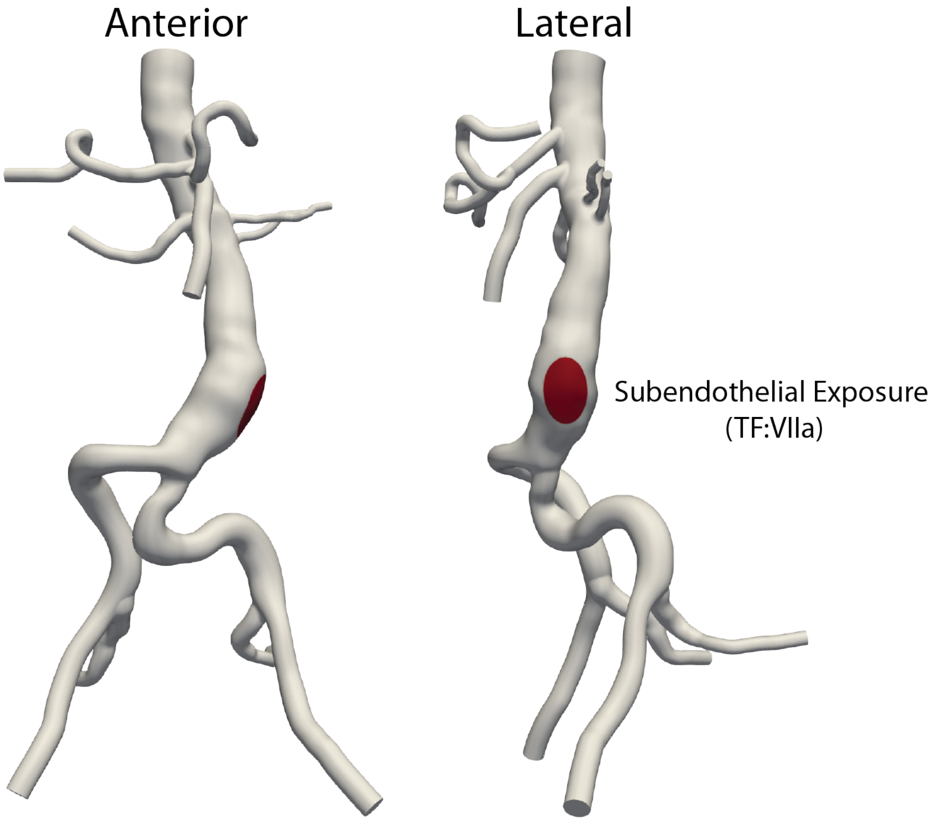

Figure 4.10: Patient-specific abdominal aortic aneurysm model. The exposed TF:VIIa representing subendothelial exposure is highlighted in red.

ics[33,60,130]. Modeling RAD transport in the cardiovascular system presents inherent numerical challenges due to the large nonlinear reaction models involved in biochemical diseases and the complex and time-dependent flow patterns and vessel geometries. These complexities are further compounded by the small diffusivities and large Péclet numbers found in cardiovascular flows[58]. In this work, an arbitrary reaction-advection-diffusion (ARAD) interface was developed for the rapid prototyping of nonlinear reaction models in cardiovascular RAD transport simulations. Figure 4.2 outlines the structure of the ARAD framework which relies heavily on Python to communicate to the FORTRAN/C++ FE flowsolver. A novel aspect of the ARAD framework is the ability to run large parallel patient-specific RAD transport simulations with an arbitrary number of scalar species (i.e. up to 20) and nonlinear reaction terms. The ARAD framework takes advantage of a Python interface for easy prototyping of

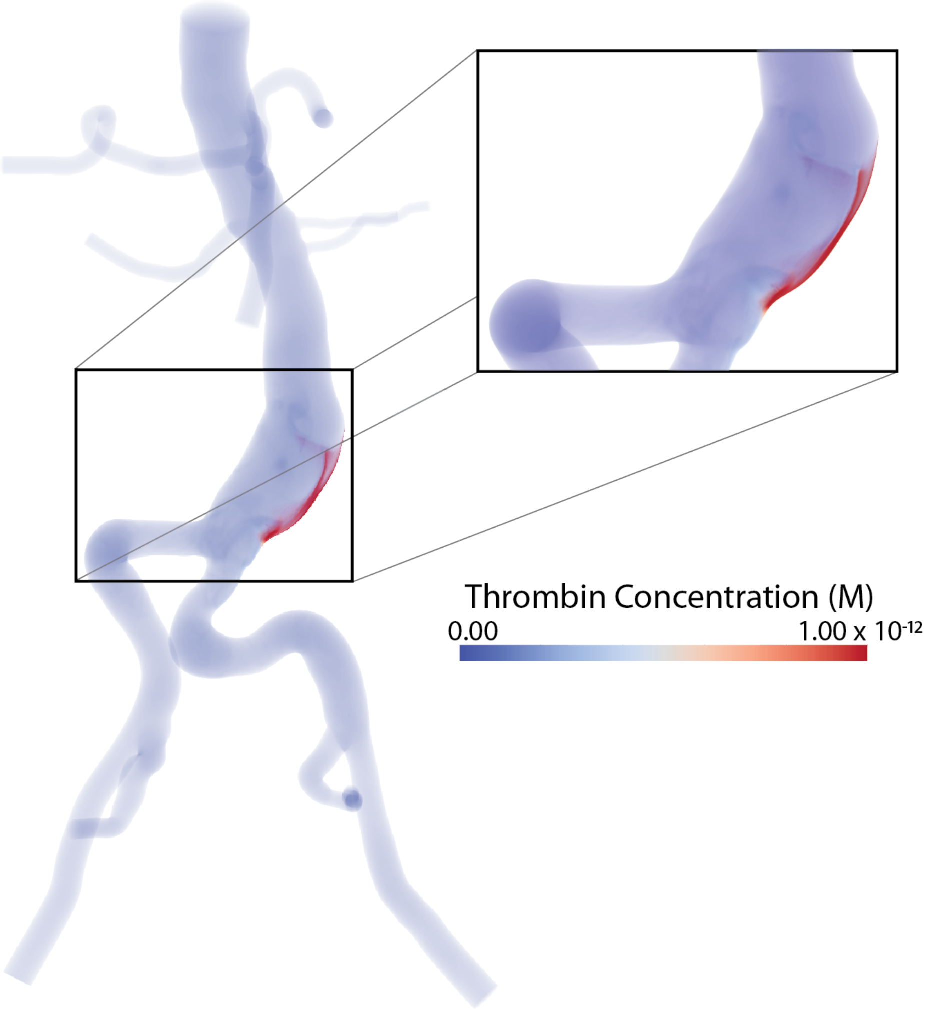

Figure 4.11: Patient-specific abdominal aortic aneurysm model with thrombin concentration generated from the TF:VIIa patch on the aneurysm wall at time $t = 16.7$ s.

the reaction models, without having to alter the underlying C++/FORTRAN finite element flow solver.

Various groups have used computational models to investigate thrombus formation. Previous computational models of thrombosis initiation have focused on reduced-order models (OD) that provide a detailed description of the biochemistry of thrombin formation in the absence of flow[23,61]. Attempts at modeling thrombin formation under flow have been limited to using idealized 3D or 2D models with broad simplifications to the hemodynamics[16,81,104]. Currently, few groups have attempted to model thrombosis initiation incorporating image-based 3D geometries, complex hemodynamics, and the complex biochemistry that describes thrombin generation. The development of such a model will be vital to improve our understanding of the role of hemodynamics in thrombus formation. Often the challenge in creating these models is the lack of methods that permit rapid prototyping of nonlinear reaction pathways in the presence of complex hemodynamics. Furthermore, it has often been considered cost prohibitive to run the full coagulation cascade in a patient-specific 3D model with realistic hemodynamics including pulsatile flow.

We first introduced a set of guidelines in Figure 4.3 that were adopted for investigating thrombosis initiation. This includes using boundary layer meshes, nondimensionalization, and appropriate stabilization techniques. Next, the scalability of the ARAD interface was compared to the FORTRAN implementation under steady flow conditions in an idealized cylinder, see Figure 4.4. Both implementations scaled well over a large range of cores with the ARAD implementation having slightly faster run times. This initial investigation illustrated the robustness of the ARAD implementation despite being Python based.

We next demonstrated the applicability of the developed ARAD interface to study thrombosis initiation in three different models: (1) an idealized geometry with steady flow, (2) an idealized geometry with periodic flow, and (3) a patient-specific geometry with periodic flow. The ability to rapidly prototype various nonlinear reaction models of thrombin generation was investigated in a idealized cylinder. Three different reactions models of increasing complexity (Figure 4.1) were investigated and results were presented for the 18-species model (Figure 4.5). In this example a thin boundary layer of thrombin was generated along the cylinder wall, beginning at the site of initiation.

The next examples considered both an idealized and a patient-specific model of a human abdominal aortic aneurysm under pulsatile flow conditions. Figure 4.7 shows thrombin generation and transport after 19.5s in an idealized AAA model. Here, the complex hemodynamics transport thrombin away from the wall, as compared to the cylindrical example where relatively no thrombin was seen in the center of the domain. In addition, Figure 4.11

illustrates the feasibility of solving thrombin generation in patient-specific cardiovascular geometries.

Currently, the ARAD interface allows for up to 20 scalar species. Future work should address this limitation to allow for 34 or more scalar species. In addition, the current application of the ARAD interface to thrombosis ignores the effects of both red and white blood cells in thrombosis initiation. Future work may aim at incorporating platelet and cellular binding sites into our thrombosis model, but this is out of the scope of the current investigation.

Future work should address implementing a model for two-way coupling between the flow and transport equations. This will be vital in enabling the model to accurately describe not only thrombosis initiation but platelet plug formation and propagation. Other groups have implemented two-way coupling between the flow and RAD equations by treating the bound platelet mass as a porous media and using Darcy's Law to describe flow through the platelet plug[81]. We plan to follow a similar approach by adding a forcing term to the Navier-Stokes equations to describe the force of the growing thrombus on the fluid field.

Lastly, in the current investigation we have presented the application of the proposed ARAD interface to study thrombosis initiation. The ARAD framework has been developed in a flexible and arbitrary manner that enables the studying of numerous biochemical diseases. In the future, the ARAD framework will be applied to study additional topics such as atherosclerosis and drug delivery.

CHAPTER V

May-Thurner Syndrome and Venous Thrombosis

To further investigate venous thrombosis, a patient with May-Thurner syndrome was studied from a hemodynamic perspective and compared to a healthy venous model. The goal of this investigation was to better understand the hemodynamic forces that contribute to thrombosis formation in patients with May-Thurner syndrome and to provide input to possible treatments and therapies.

5.1 Introduction

May-Thurner syndrome is a rarely diagnosed condition that occurs due to an anatomical variant where the right common iliac artery overlays and compresses the left common iliac vein against the lumbar spine[113]. Compression of the left iliac vein against the lumbar vertebrae combined with trauma caused by arterial pulsation can, overtime, lead to accumulation of elastin and collagen with intimal proliferation in May-Thurner patients[101]. Histologic analyses of veins with May-Thurner syndrome have demonstrated that normal/healthy vein intima and media are replaced with connective tissue covered by endothelium[116] and can create a mechanical obstruction to blood flow and increases the risk of left-sided iliofemoral thrombosis[116]. This may explain why left-sided iliofemoral deep vein thrombosis is nearly five times more frequent than right-sided thrombosis[116] and why May-Thurner syndrome is often associated with development of deep vein thrombosis and chronic venous insufficiency[75].

Many patients with May-Thurner syndrome are asymptomatic or never develop complications[73], while other patients present with left leg edema, pain, deep vein thrombosis, or pulmonary embolism[75]. Typically May-Thurner syndrome is only diagnosed and treated for symptomatic patients presenting with DVT or PE[25]. Anticoagulation alone is typically ineffective for treatment[75], suggesting that hemodynamics play a large role in thrombus formation in May-Thurner patients. The goal of May-Thurner surgical repairs (open or endovascular) is to restore normal hemodynamics by increasing the luminal size of the compressed vein. Treatment strategies have evolved from predominately open surgical techniques towards endovascular therapy including catheter-directed thrombolysis, mechanical thrombectomy, self-expanding stent placement, or a combination[86]. Previous reports have shown that anticoagulation alone and thrombectomy combined with prospective anticoagulation have a rethrombosis rate of up to 73% in patients with May-Thurner syndrome[24], further indicating that hemodynamics plays a significant role in the pathophysiology of May-Thurner syndrome.

Currently it is not completely understood why some people with May-Thurner syndrome present with DVT or PE and why others remain asymptomatic. This may be due the presence of co-morbidities. Regardless, there remains a need to better understand the pathophysiology of May-Thurner syndrome and how the unique venous hemodynamics in these patients contributes to the formation of venous thrombosis. The goal of this investigation is to compare hemodynamic metrics between a patient-specific model of a patient with May-Thurner syndrome compared to a patient with normal venous anatomy and hemodynamics.

5.2 Methods

In this study, we compared hemodynamic metrics of flow and Lagrangian transport in two patient-specific venous geometries: (a) a May-Thurner venous anatomy, and (b) a normal venous anatomy. First, we describe the computational domain and the associated boundary conditions for each model. Subsequently, we perform a comparative hemodynamic and transport analysis for each model.

Initially, a patient was treated at the University of Michigan hospital for pulmonary embolism and after further investigation the patient was diagnosed with deep vein thrombosis and May-Thurner syndrome from ultrasound and CTA imaging. A patient-specific computational model of the iliac bifurcation and inferior vena cava of a patient with May-Thurner anatomy was obtained from computed tomography angiography (CTA) image data and segmented using the cardiovascular hemodynamic modeling environment CRIMSON[6].

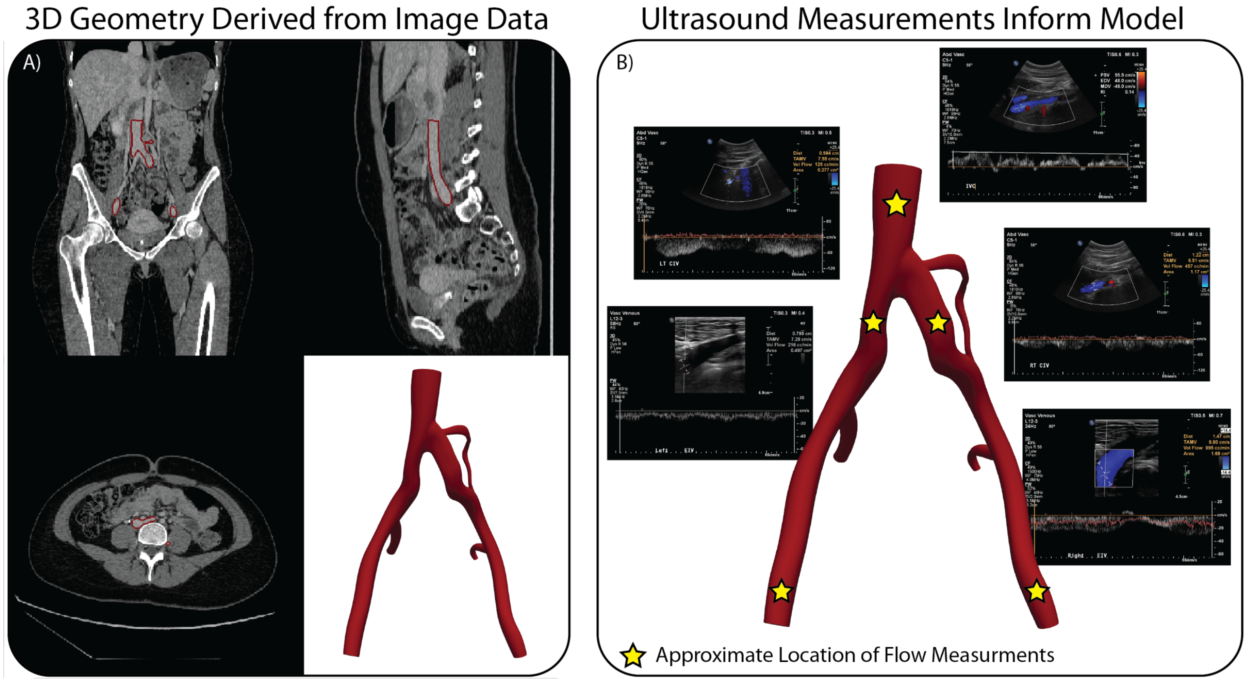

Figure 5.1: Data collected from patient treated at the University of Michigan hospital for thrombosis and pulmonary embolism with a May-Thurner anatomy. (Left) CTA imaging and reconstructed computational model (Right) ultrasound data collected at 5 locations (approximate location shown on the computational model)

The computational domain consists of the inferior vena cava (IVC) and the left and right internal iliac (II) and external iliac veins (EI). For the flow analysis, duplex Doppler ultrasonography-derived periodic flow data mapped to parabolic velocity profiles were prescribed at the 4 inlet vessel faces (external and internal iliac veins). A three-element Windkessel model was applied to the IVC outlet face. The vessel walls were assumed to be rigid and were prescribed a homogeneous Dirichlet boundary condition for the velocity field.

Figure 5.1 shows the CTA and ultrasound imaging and corresponding computational model.

The healthy (normal) venous model from Chapter II was used as a control and compared to the May-Thurner simulation. For the current investigation, blood is modeled as a Newtonian fluid with a density of 1060 kg/m^3. Differences between velocity magnitude, shear rate, wall shear stress (WSS), and Lagrangian indices of shear (PLAP, see Chapter II) were studied between the May-Thurner and healthy venous models.

5.3 Results

5.3.1 Hemodynamic Analysis

We first performed a comparative analysis between the May-Thurner and normal hemodynamics. For the comparative hemodynamic analysis, we consider the velocity solution field as well as derived quantities (shear rate, vorticity and WSS). Increased shear rates have been linked to VWF unfolding and platelet activation[153]. Vorticity is obtained as the curl of the velocity field ($\omega = \nabla \times \mathbf{u}$) and provides information about the local spinning motion of the fluid in the domain. Vortical motion has been linked to various cardiovascular pathologies, such as atherosclerosis and thrombosis[15,16,36]. In contrast, WSS is a surface quantity that provides an assessment of the shear forces imposed by the fluid on the vessel wall. Alterations in WSS have been linked to local alterations in endothelial mechanobiology that leads to either pro-atherosclerotic or pro-thrombogenic phenotypes[36,105].

Figure 5.2(A,B) show volume rendered plots of the magnitude of velocity for the May-Thurner and healthy venous models. It can be observed that the velocity magnitude is increased in the May-Thurner case. This is expected given that the increased flow rate and decreased luminal diameter of the compressed left iliac vein. In addition, Figure 5.2(C,D) shows volume rendered plots of the shear rate for both models. Increased shear rates are observed in the May-Thurner model, greater than 1000 s^{-1}, which corresponds to levels of shear that can unravel VWF and lead to increased rates of thrombosis formation[153].

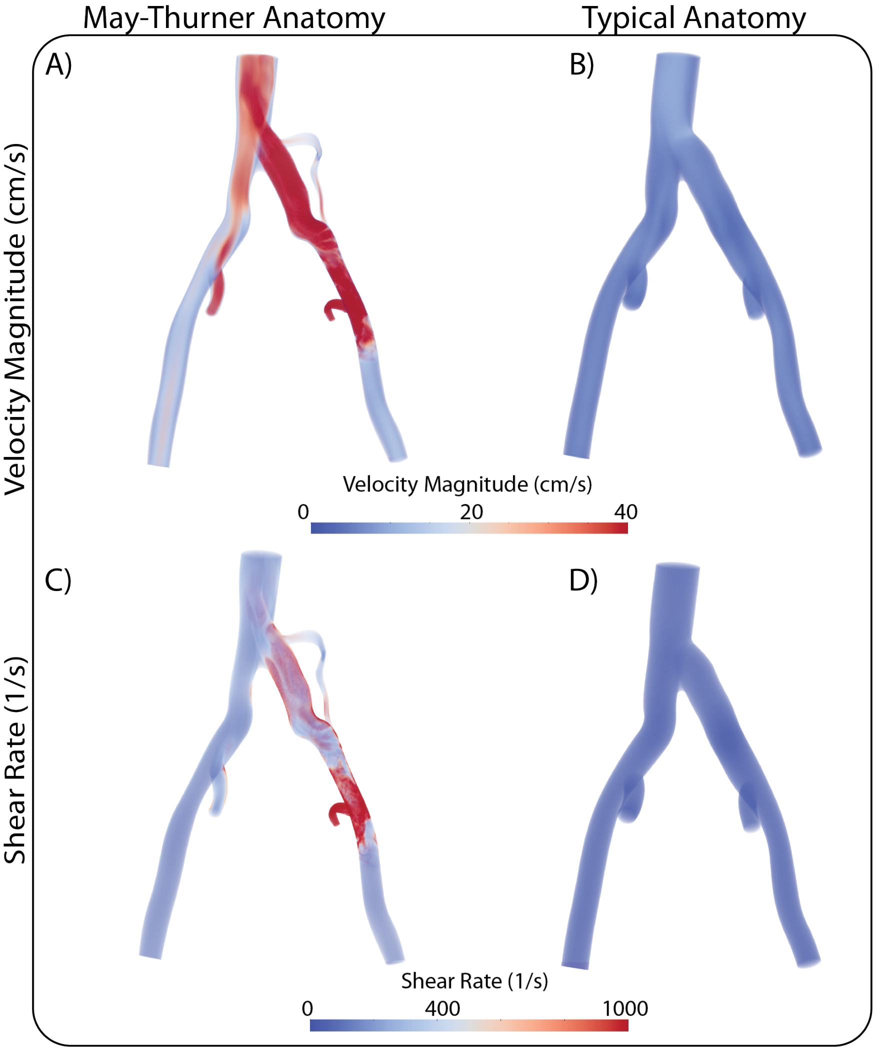

Figure 5.2: Flow Metrics

Figure 5.3 shows a comparison of WSS for the May-Thurner and healthy venous models. Increased WSS is observed in the May-Thurner anatomy (left) compared to the healthy venous model (right). The highest regions of WSS are observed in the left internal and common iliac veins of the May-Thurner model. In particular, the left common iliac vein shows higher WSS than the right common iliac in the diseased anatomy suggesting that the left iliac vein compression is responsible for the higher values of WSS.

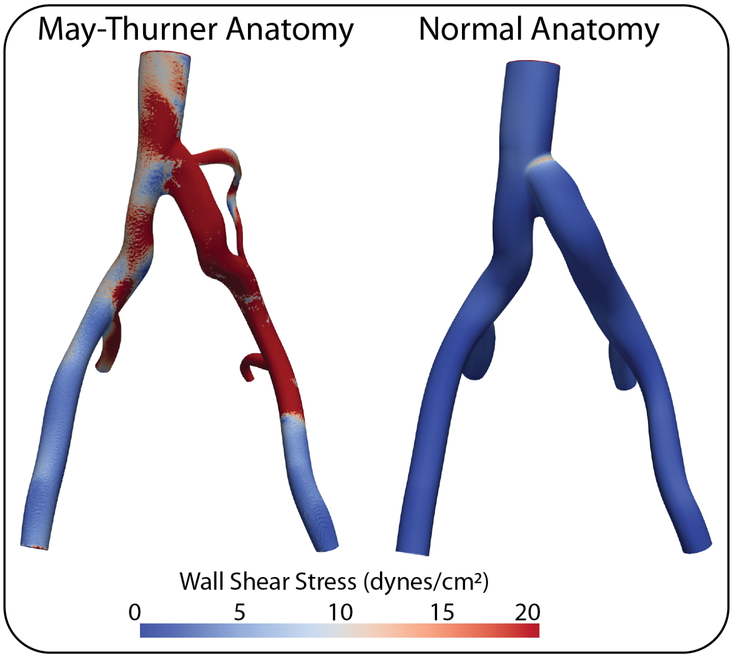

Figure 5.3: Computer model showing values of WSS for a patient with May-Thurner syndrome (Left) and a normal venous anatomy (Right). Higher values of WSS are observed in the May-Thurner anatomy with highest values occurring in the region of left iliac vein compression.

5.3.2 Lagrangian Particle Tracking Analysis

The transport of biochemical species such as proteins, platelets and chemical signaling species plays a significant role in the initiation and propagation of various cardiovascular diseases such as thrombosis and atherosclerosis[16,60,130]. We next investigate the effect of the May-Thurner anatomy and hemodynamics on Lagrangian transport in the two patient-specific models.

In this work, approximately one million particles were injected into both venous computational domains and tracked for ten cardiac cycles. Particles were collected in virtual spheres at the outflow(s) as they left each domain. For both venous simulations, four particle boluses, each with approximately 250,000 particles, were released from the inflows (left EI, left II, right EI, and right II). Particles were tracked as they were passively advected through each computational domain over time. Statistics on platelet activation potential (PLAP) and the number of particles in the computational domains were recorded.

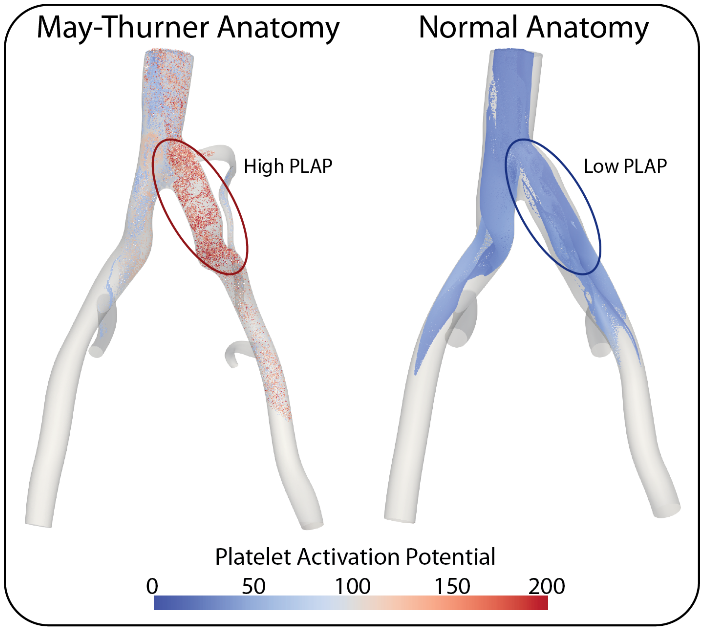

Figure 5.4: (Left) Computer model of a patient with May-Thurner syndrome displaying values of PLAP. Area of highest platelet activation potential is visualized by the red circle. (Right) Simulation of PLAP in a healthy venous anatomy. Lowest values of PLAP (accumulated shear) are highlighted by the blue circle.

Figure 5.4 shows the particles left in the May-Thurner and healthy venous domains. PLAP is observed to be significantly higher in the May-Thurner case. In addition, the particles in the May-Thurner anatomy leave the domain at a faster rate. Higher values of PLAP correspond to higher platelet activation potential and have previously been linked to thrombosis formation[36,98]. Therefore, the higher PLAP values observed in the diseased May-Thurner anatomy can serve as a possible additional explanation for the formation of large thrombi in these patients.

5.4 Conclusion

In this investigation, we performed a preliminary comparison of hemodynamic and transport metrics that have been associate with thrombosis formation[36,98] between a May-Thurner and healthy venous anatomy. Preliminary results suggest that the compressed common iliac vein in the May-Thurner anatomy leads to increased velocity, shear rate magnitude, wall shear stresses, and increased accumulation of shear assessed through Lagrangian particle tracking. Suggesting possible mechanisms for thrombosis formation in May-Thurner patients.

Virchow described the leading factors that contribute to venous thrombosis as hemodynamics (stasis), hypercoagulability, and endothelial injury (wall damage). It is generally accepted that venous thrombosis most often forms due to stasis in combination with hypercoagulability or endothelial injury. Venous thrombi have long been described as 'red thrombi' rich in red blood cells as compared to the platelet rich arterial thrombi. We previously described in Section I that platelets can be activated with high shear rates which in turn increases the rate of arterial thrombosis. Based on the current preliminary hemodynamic analysis of a patient with May-Thurner syndrome we propose that in patients with May-Thurner anatomy due to the compression of the left iliac vein, arterial shear rates are achieved that contribute to the formation of venous thrombosis in these patients. These increased shear rates have previously been observed to cause platelet activation and thrombosis formation in arterial stenosis. We argue that these patients are at a higher risk of venous thrombosis formation because of increased venous shear rates from the compression of the left iliac vein.

First, we performed a hemodynamic comparison between the May-Thurner and healthy venous models. For the May-Thurner model, increased velocity magnitude, shear stress magnitude, and WSS were observed. Next, we performed a Lagrangian mass transport analysis in both the May-Thurner and normal models to assess the effect of the compressed left iliac vein on cardiovascular mass transport. Here, we employed a particle tracking technique where numerous massless tracer particles were introduced in the flow field. These particles are then tracked as they traverse through the computational domain to enable a Lagrangian interpretation of the flow field. This analysis allows us to calculate 'platelet activation potential' (PLAP), a metric to assess the history of shear stresses experienced by the particles as they travel through the computational domain. Our Lagrangian mass transport analysis revealed a significant increase in PLAP values in the May-Thurner anatomy.

Additional studies on more patients are needed to confirm the current hypothesis. In addition, it will be imperative to perform non-Newtonian analyses on these patients based on results from Chapter II where is was observed that Newtonian viscosity can lead to increased values of PLAP and altered values of WSS compared to non-Newtonian viscosity. Although the current data serves only as a preliminary analysis, the results show an exciting new explanation for the high rate of formation of venous thrombi in patients with May-Thurner anatomy.

CHAPTER VI

Novel Applications of ARAD Framework

Contributions. *Dr. Yunus Ahmed, MD is the main investigator on the ECMO project. He created the patient-specific hemodynamics models and I preformed the scalar mass transport analysis. Kritika Iyer is the main investigator on the coronary flow project. She performed the hemodynamics analysis and I was responsible the scalar mass transport model.*

After the implementation and investigation of thrombosis initiation the developed scalar framework has been applied to study two other cardiovascular diseases: (1) extracorporeal membrane oxygenation (ECMO) and (2) impaired coronary flow.

6.1 ECMO

6.1.1 Introduction

Extracorporeal membrane oxygenation (ECMO) is a mechanical device that temporarily supports the function of both the heart and lungs and is designed to help patients with failing hearts. There are two types of ECMO used clinically, (1) Veno-venous-ECMO (VV-ECMO) where the ECMO cannula is connected to one or more veins, usually near the heart, and is used when a patient's lungs are failing and (2) Venoarterial-ECMO (VA-ECMO) where the cannula is connected to both a vein and an artery and is used when both the heart and lungs are unable to function sufficiently[117]. In VA-ECMO blood flow is routed to an artificial lung that adds oxygen to the blood and is subsequently pumped back into the patient's circulation. VA-ECMO therapy may be prompted in the following conditions: acute myocardial infarction, sepsis, hypothermia, post-transplantation, COVID-19, as well as others. ECMO provides circulatory support and allows time for the heart and lungs to rest and recover or bridges the gap to a more permanent therapy/solution (i.e. transplantation, Left Ventricular Assist Device (LVAD), etc.). ECMO driven flow is non-pulsatile, and thus ECMO patients have unique blood flow characteristics from the combination of cardiac-driven pulsatile hemodynamics and ECMO-driven steady-state hemodynamics. This interplay results in regions involving high shear flows, abnormal pulsatility, and lower perfusion pressures.

The focus of this investigation is VA-ECMO. Two principal VA-ECMO configurations exist (1) peripheral and (2) central. Peripheral ECMO cannulation involves inserting the ECMO cannula in either the femoral or subclavian artery. The venous cannula with be placed into the femoral artery and positioned at the level of the right atrium. The main advantage of peripheral artery cannulation is the ease of insertion of the arterial ECMO cannula, unlike central ECMO cannulation, peripheral cannula does not require a sternotomy and can be performed outside of the operating room. However, disadvantages of peripheral ECMO cannulation can include aortic root thrombus formation and left ventricular distension, and lower extremity ischemia[69]. Furthermore, when using femoral cannulation the femoral arterial lumen becomes partially occluded by the cannula, little blood from the ECMO cannula is able to flow in the retrograde direction[69]. This results in little to no blood flow in the distal femoral tree[69]. To overcome this, a distal perfusion cannula will be placed to perfuse the distal femoral tree. Finally, when the cannula is placed in the femoral artery, features retrograde flow from the arterial cannula competing with the native antegrade blood flow generated by the impaired heart. This can lead to scenarios where regions of the body receive blood from different sources (heart or ECMO) and becomes clinically relevant when the heart and lungs are too weak to produce sufficiently blood oxygenation levels. Therefore, scenarios arise where the upper body only receives semi- or de-oxygenated blood from the weakened heart, resulting in arterial hypoxemia in regions of the upper part of the body. This is also known as the Harlequin or North-South syndrome[30,107].

Alternatively, in central VA-ECMO the arterial cannula is inserted directly into the ascending aorta. The venous cannula will be placed directly into the right atrium. In this instance the chest is open. Central VA-ECMO cannulation is used when the ventricle is too weak to wean off bypass following open heart surgery or as an alternative if peripheral ECMO does not achieve adequate flows and/or end-organ function[107]. The invasive nature of central cannulation serves as its main disadvantage due to complications from sternotomy related issues (i.e. bleeding, infection, etc.), aortic dissection, inability to mobilize the patient, ischemic events, etc[122].

Not much is currently known about which VA-ECMO cannulation strategy is ideal. In particular, little is known about how the cannulation site affects the hemodynamics of the patient. The goal of this study is to investigate the hemodynamics and mass transport of blood in different configurations for vascular access in VA-ECMO, seen in Fig. 6.1.

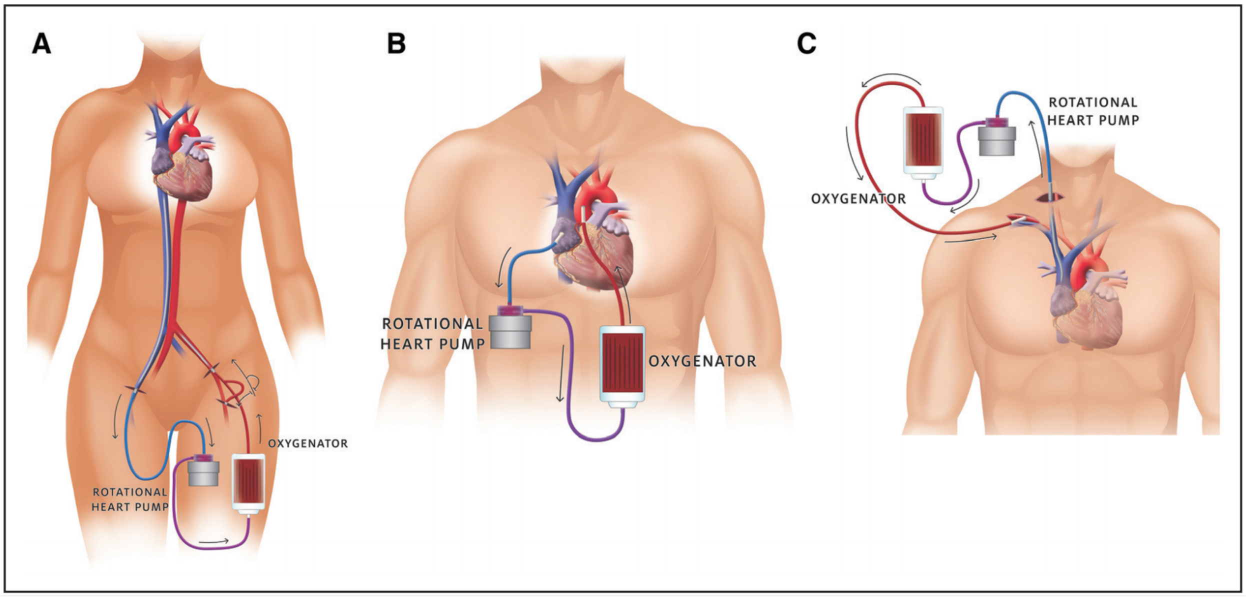

Figure 6.1: VA-ECMO cannulation locations taken from Rao, P. et al.[117]. Femoral artery cannulation (A), ascending aorta cannulation (B) and subclavian artery cannulation (C).

6.1.2 Methods

In this investigation, scalar mass transport was used to study and compare three different configurations for vascular access for VA-ECMO using patient-specific models. A 56-year old female patient with a history of non-ischemic cardiomyopathy was treated at the University of Michigan's Cardiovascular Center. The patient presented with non-sustained ventricular tachycardia and unstable hemodynamics and was treated with a combination of an implantable cardioverter defibrillator and hemodynamic support from VA-ECMO via a femoral access for 10 days.

6.1.2.1 Computational Modeling

The arterial baseline geometry was built from computed tomography angiography (CTA) image data and adapted to represent the three possible locations of ECMO cannulation ((1) femoral, (2) subclavian, and (3) ascending aorta) using the cardiovascular hemodynamic modeling environment CRIMSON[6]. Figure 6.2 shows the baseline and adapted computational domains. The baseline domain is comprised of the aortic inflow and 13 outlet branches, while the three adapted domains are comprised of both the aortic and ECMO cannula inflows as well as the 13 outlet branches.

Each aortic geometry was discretized into 3.9 million linear tetrahedral elements. For the baseline geometry, a prescribed periodic flow waveform (with time period $T = 0.90\,\mathrm{s}$) mapped to a parabolic velocity profile was imposed at the aortic inflow, and three-element Windkessel models[135] were prescribed at each outlet face, representing the behavior of the distal vascular beds (numerical values given in Supplementary Material). For the three VA-ECMO configurations, an additional constant inflow was prescribed at the at ECMO cannula. Based on patient-specific data collected at the University of Michigan hospital, a cardiac output of 1.08 L/min and an ECMO output of 3.4 L/min were prescribed.

Cycle-to-cycle periodicity was achieved after running the flow problem under a rigid wall assumption for five cardiac cycles, corresponding to a physical time of $t = 4.50\,\mathrm{s}$. Subse-

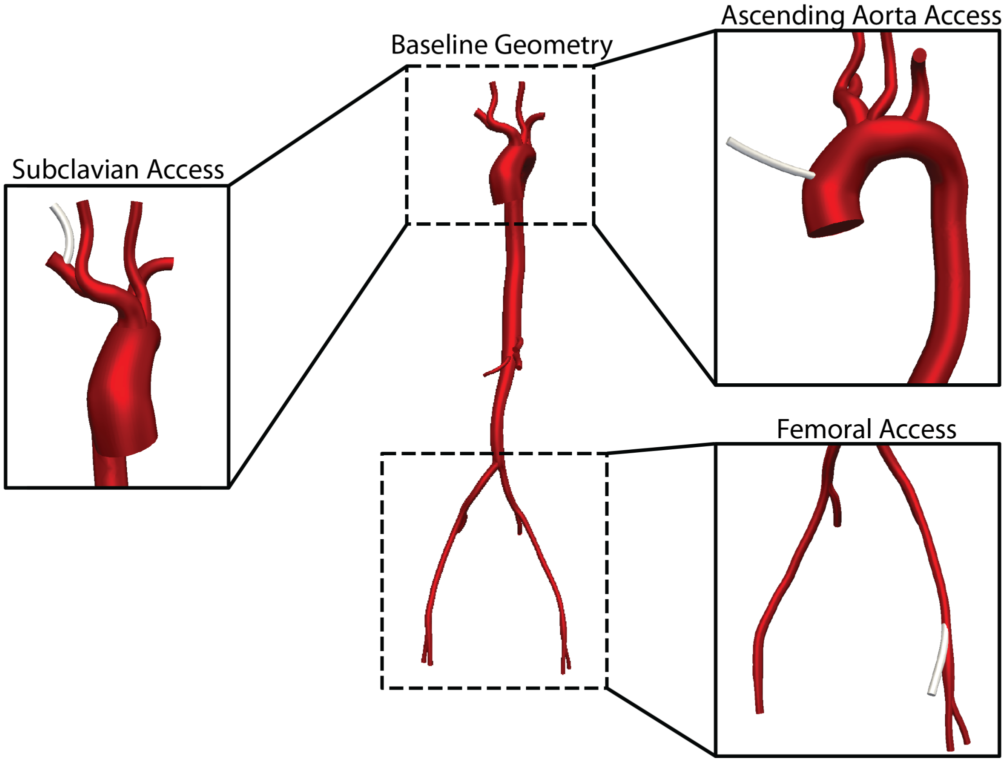

Figure 6.2: Baseline and adapted ECMO Geometries

quently, the scalar advection-diffusion equations were solved for the ECMO configurations using a staggered approach for two scalar species, assuming a zero-reaction term ($R = 0$) for each species. A zero-concentration initial condition was prescribed for both scalar species. Two Dirichlet inlet boundary conditions of $c = 10$ mol/mm^3 were prescribed at the ascending aortic inflow face to track the transport of blood by the weakened heart and the ECMO cannula inlet face to track the transport of blood from the ECMO circulation. Zero total flux boundary conditions were prescribed for both scalars at the vessel walls. For both scalars, a Consistent-flux boundary condition was prescribed for all outlets, except the aortic inflow and ECMO cannula, where zero-Dirichlet boundary conditions were prescribed. Simulations were run using a constant time step size of $\Delta t = 2x10^{-5}$ s until cycle-cycle periodicity was achieved for the scalar problem (approximately 22 cardiac cycles).

6.1.3 Results

The femoral access ECMO simulation was first investigated as it corresponds to the access location used to treat the patient at the University of Michigan hospital. Fig. 6.3 shows results of the femoral ECMO model after 22 cardiac cycles corresponding to diastole. It can be observed that due to the weakened heart and corresponding impaired cardiac output, the blood velocity is lower in the aortic arch and abdominal aorta. Due to the higher constant flow rate from the ECMO cannula insert at the femoral artery, blood velocity is higher in the femoral and the infrarenal aortic arteries, this is particularly emphasized during diastole, see Fig. 6.3. The pressure contours seen in Fig. 6.3 correspond to lower values typically observed during diastole throughout the computational domain, except in the ECMO cannula where higher pressure 100 mmHg is observed. Lastly, in the plot of both scalar concentrations we can see that blood transported from the heart and ECMO cannula mix and form the Harlequin region at the location of the left subclavian artery when flow stabilized after approximately 20 cardiac cycles.

Subsequently, the ascending aorta and subclavian cannula access locations were investigated. After running each VA-ECMO configuration until cycle-to-cycle periodicity was achieved for the scalar problem, scalar concentration results from each configuration were compared. Fig. 6.4 shows similar results for the ascending aorta and subclavian ECMO cannula configurations. Both configurations show similar mass transportation of oxygenated blood from the ECMO cannula to all main aortic branches and outlets. These configurations are highly invasive and pose higher risks to the patients (compared to femoral access) related to coronary arteries or cerebral perfusion because the cannula is positioned closer to the heart and aortic arch. Conversely, the femoral VA-ECMO model shows predominately transport of blood form the heart to the right subclavian and carotid arteries with the Harlequin region forming around the left subclavian artery.

In this work we compared hemodynamics (flow, pressure, and mass transport) between 3 VA-ECMO configurations. This serves as preliminary work to investigate VA-ECMO

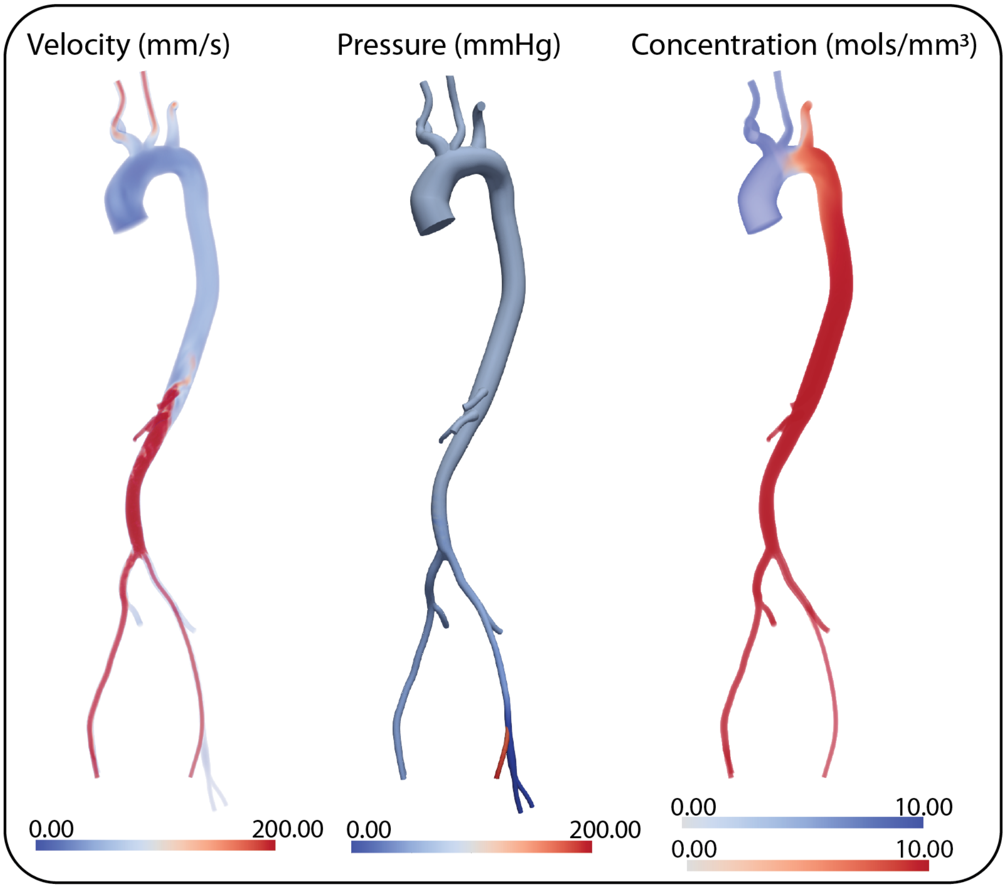

Figure 6.3: Velocity volume rendering (A), pressure contours (B) and volume rendering of scalar from the heart (blue) and ECMO cannula (red) after 22 cardiac cycles (C). Time point corresponds to diastole.

configurations for patient treatment. Additional work is needed to further study the effects of cannulation location on hemodynamic metrics such as wall shear stress and vorticity, similar to Section II. Future work should address varying ECMO and cardiac flow rates and investigate the effects of ECMO flow rate on transport, Harlequin region, and hemodynamic metrics (WSS and vorticity).

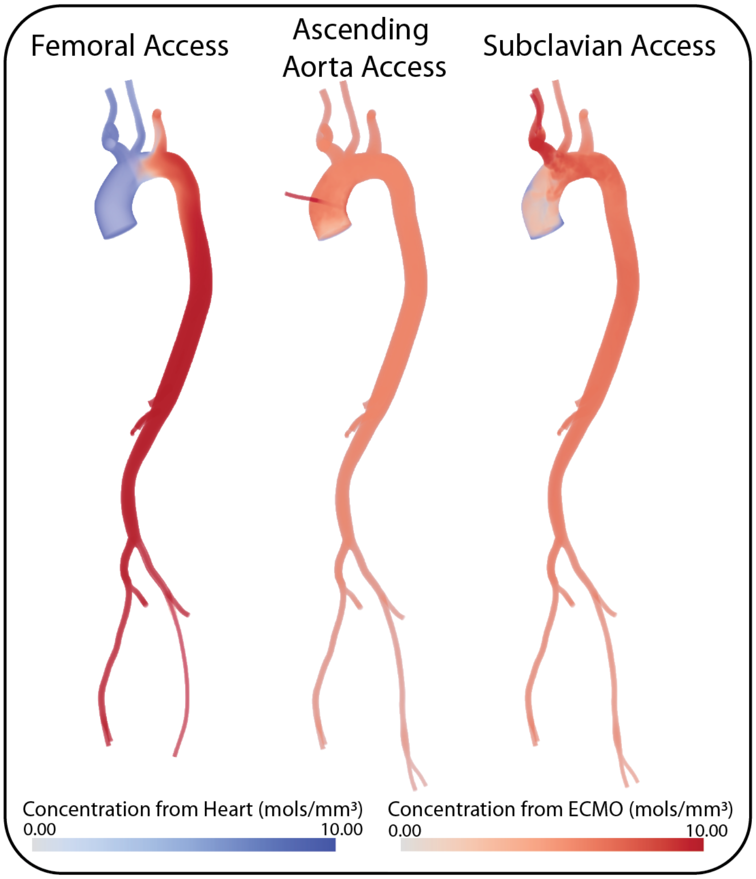

Figure 6.4: Volume rendering of scalars species from the heart (blue) and ECMO cannula (red) for (A) Femoral, (B) Ascending Aorta, and (C) Subclavian cannula locations.

6.2 Coronary Flow

Next, the stabilized reaction-advection-diffusion framework developed in Section III was applied to study coronary transport. In this example a patient-specific model of the coronary tree of a 58 year-old man treated at the University of Michigan Cardiovascular Center was built and tuned to match patient-specific flow data using CRIMSON[6]. The patient had calcified and non-calcified lesions in the major branches of both the left and right coronary arteries. Specifically, the patient had a 30%, 50%, and $> 70\%$ stenosis in his left anterior descending coronary artery, a 50% and 70% stenosis in his left circumflex coronary artery, and a $> 70\%$ stenosis in his right coronary artery with diffuse $40 - 70\%$ throughout the midsection of the vessel.

The flow and pressure fields were solved for using the developed computational model. In addition, a virtual angiogram was created using our scalar transport model. Briefly, a catheter inserted into the aortic root and directed at the left coronary artery was modeled using CRIMSON. A single scalar species, mimicking a dye, was virtually injected into the catheter and the spatial temporal evolution of the injected scalar species was tracked through the distal left coronary tree over time, creating a virtual coronary angiogram, see Fig. 6.5. In this example, again only the advection and diffusion of the scalar species through the flow field was considered without any reaction terms.

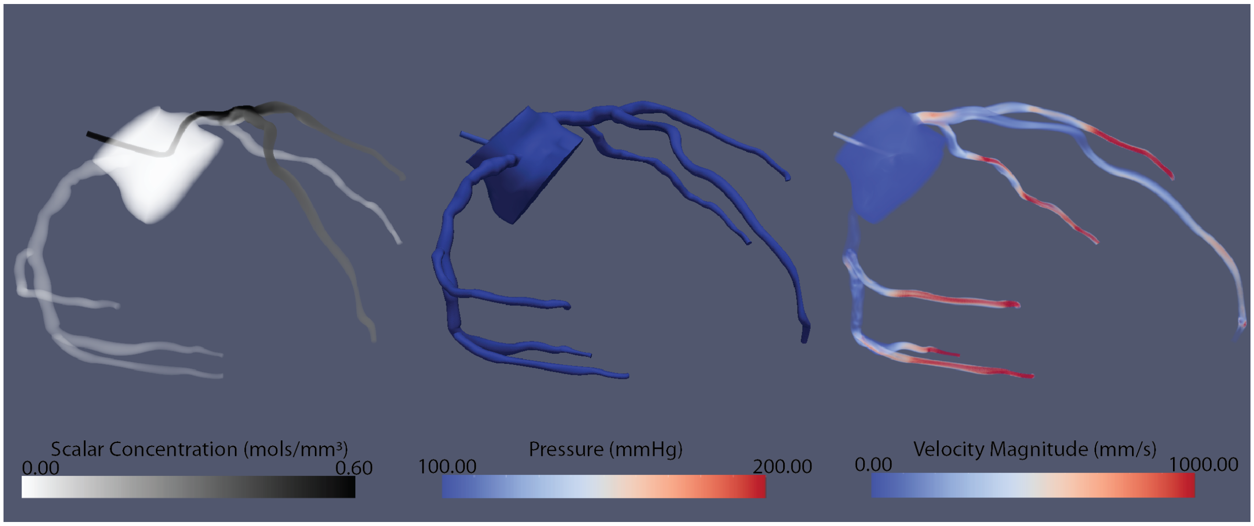

Figure 6.5: Coronary Flow

Fig 6.5 shows results of the scalar, pressure, and velocity fields for the coronary model. Preliminary results demonstrate the ability to create a computational angiogram. Future studies will work on using this data to aid in diagnosis and treatment of coronary stenosis.

CHAPTER VII

Discussion

7.1 General Discussion

Thrombosis represents a large burden for the health care system[56,85]. Despite recent advancements in thrombosis research[38,52,137], the understanding of the pathophysiology of thrombosis initiation is incomplete and still evolving. Understanding the effects of hemodynamics and biochemistry on thrombosis initiation is of significant importance to develop more effective thrombolytic therapies and preventative measures. In comparison with *in vitro* or *in vivo* experiments, computational modeling can give insights into the hemodynamic and biochemical processes with high spatial and temporal resolution. In this thesis, we developed advanced computational models of thrombosis to investigate the effects of complex hemodynamics on thrombosis initiation. The goal of this work was to develop a robust and flexible model of thrombosis initiation that can be used to probe this disease. Furthermore, the key question that we have investigated with our model is whether hemodynamics at the early stages of thrombosis initiation affects thrombosis formation.

Thrombosis occurs in both arterial and venous flows over a large range of shear rates. Blood is known to exhibit non-Newtonian viscosity, particularly in regions of low shear. Therefore in this investigation, we first implemented non-Newtonian rheological models into CRIMSON to accurately capture the hemodynamics in both arterial and venous flows. In this study, two non-Newtonian rheological models (Power Law and Carreau-Yasuda) were implemented into the cardiovascular hemodynamic modeling environment CRIMSON and the Carreau-Yasuda model was used to investigate patient-specific arterial and venous flows. The Carreau-Yasuda model revealed important differences in both hemodynamic and Lagrangian transport metrics relative to a Newtonian approximation. In-plane velocity, vorticity, recirculation, and platelet activation were consistently larger in the Newtonian approximation for both models The Newtonian assumption rendered larger values of wall shear stress for the arterial model. Conversely, the non-Newtonian model produced larger wall shear stress for the venous model. These findings demonstrate the importance of including non-Newtonian rheological models in cardiovascular simulations where low shear rates are expected, such as diseased arterial and venous flows.

In order to simulate thrombosis initiation, it is necessary to first develop a framework for mass transport simulations. Numerical simulations of cardiovascular mass transport pose significant challenges due to the wide range of Péclet numbers and backflow at Neumann boundaries. In this work we presented and discussed several numerical tools to address these challenges in the context of a stabilized finite element computational framework. To overcome numerical instabilities when backflow occurs at Neumann boundaries, we proposed an approach based on the prescription of the total flux. In addition, we introduced a "consistent flux" outflow boundary condition and demonstrated its superior performance over the traditional zero diffusive flux boundary condition. Lastly, we discussed discontinuity capturing (DC) stabilization techniques to address the well-known oscillatory behavior of the solution near the concentration front in advection-dominated flows. We presented numerical examples in both idealized and patient-specific geometries to demonstrate the efficacy of the proposed procedures. The three contributions discussed in this thesis enable us to successfully address commonly found challenges when simulating mass transport processes in cardiovascular flows.

Despite the gains made during this investigation various limitations still exist regarding scalar advection-diffusion finite element implementation. Although herein the authors have demonstrated the superiority of consistent flux boundary condition in reducing boundary effects, small effects were still observed and serve as a limitation to this condition. In addition, the DC operator used in this investigation is nonlinear and therefore converts the scalar advection-diffusion equations from linear to nonlinear. Therefore, the DC operator should only be employed in situations of high Pe flows where large gradients exist at the scalar wavefront. Although, the use of these operators is non-ideal due to the increased nonlinearity, they are ultimately necessary because without the DC operator oscillations in the solution persist.

We next presented a stabilized flexible arbitrary scalar reaction-advection-diffusion (ARAD) framework for computational modeling of thrombosis initiation in patient-specific cardiovascular models. We implemented and verified our numerical framework within CRIMSON. The developed framework relies heavily on Python to interface with CRIMSON's C++/FORTRAN flowsolver without the need to recompile or edit the source code. Strong and weak scalability tests were performed over a broad range of mesh sizes and computing hours. Results showed the Python-based framework did not result in a reduction in computational efficiency. We next applied the developed ARAD framework to study thrombosis initiation in both idealized and patient-specific geometries. Three different biochemical models of increasing complexity, ranging from purely phenomenological to mechanistic, were investigated in an idealized-cylinder. After prototyping the thrombin generation models, the most complex and biochemically informative model was used to investigate thrombosis initiation in both an idealized and patient-specific abdominal aortic aneurysm. Results showed that complex hemodynamics affects both thrombin generation and propagation. In addition, 'methods of best practice' were discussed for thrombosis modeling, including the use of refined boundary layer meshes and non-dimensionalization to address near-wall mass transport. Overall, this work presented a stabilized numerical framework for mass transport that allows for the flexible prescription of complex nonlinear reaction models of thrombosis initiation. Investigation into thrombin formation in idealized and patient-specific geometries suggested that hemodynamics has a significant role in thrombin initiation and propagation *in vivo*.

Our computational model of thrombosis initiation is limited by the complexity of the scalar models used. Currently, using the developed ARAD framework it is possible to prototype ODE-based reaction models with up to 20 scalar species. Often, reaction networks describing thrombosis initiation contain 30 or more scalar species[62]. Additionally, blood cells (RBCs, WBCs, and platelets) are known to affect the thrombotic process, but have not been incorporated into our model.

7.2 Future Work

One of the primary limitations of the hemodynamic and transport studies presented in this work is the use of rigid wall assumption. Particularly in the case of the venous models, this assumption is no longer valid. Given the implementation of deformable wall models within CRIMSON, it is possible to directly extend the current study to incorporate vessel wall compliance. Furthermore, given the disparate observations concerning WSS in arterial and venous models in our analysis, future studies will include a broader range of flow conditions and model geometries to better understand their effects on flow and transport metrics.

In the future we plan to expand our computational model of thrombosis initiation by increasing the number of scalar species that can be modeled to 34 or more. Future investigations may also incorporate platelet and cellular binding sites. The thrombosis model presented herein utilizes one-way coupling between the Navier-Stokes and RAD equations. Future work should address implementing a model for two-way coupling between the flow and transport equations. This will be vital in enabling the model to accurately describe not only thrombosis initiation but platelet plug formation and propagation. Other groups have implemented two-way coupling between the flow and RAD equations by treating the bound platelet mass as a porous media and using Darcy's Law to describe flow through the platelet plug[81]. We plan to follow a similar approach by adding a forcing term to the Navier-Stokes equations to describe the force of the growing thrombus on the fluid field. This will enable the exploration of RAD transport within the growing thrombus and the effect of reduced luminal size on flow through a vessel.

In Chapter III we proposed the "consistent flux" boundary condition for scalar mass transport and investigated its accuracy compared to the typically prescribed zero-diffusive flux condition. Although this is an improvement to the typically used zero Dirichlet or zero Neumann boundary conditions this is still not an accurate representation of what happens *in vivo* where blood vessels form a closed-loop system. Similarly to reduced-order models widely adopted for cardiovascular flow problems[5,134,135], it is critically important to develop reduced-order models of mass transport for the proximal and distal portions of the vascular system not included in the 3D geometric model. This is particularly important when dealing with closed-loop models and simulations involving reaction. Furthermore, this will be crucial for thrombosis models where it is necessary to track the amount of thrombin for example that leaves and reenters a domain through transient flow at a boundary.

Additionally, the proposed model of thrombosis initiation discussed in Chapter IV simulates thrombin generation and transport on the span of seconds to minutes. At this stage the thrombus is young and not fully formed. Numerous *in vivo* works have investigated the differences between acute (days) and chronic (weeks-months) thrombosis, as well as the long term effects of chronic thrombosis on vessel walls. Histological techniques allow for a better understanding of the structural components of a biological sample. Using a stasis murine model for DVT (the stenosis model), 3 day old acute and 9 month chronic thrombi were previously analyzed for their structural components. Four staining techniques were utilized: Hematoxylin and eosin (H&E), Masson's Trichrome, Picrosirius Red, and Martius Scarlet Blue (MSB) were utilized. Results can be seen in Figures 7.1 and 7.2.

From this investigation, we gained insight into structure of thrombus. Figure 7.1 reveals that acute thrombus is predominately composed of fibrin and red blood cells. The formation

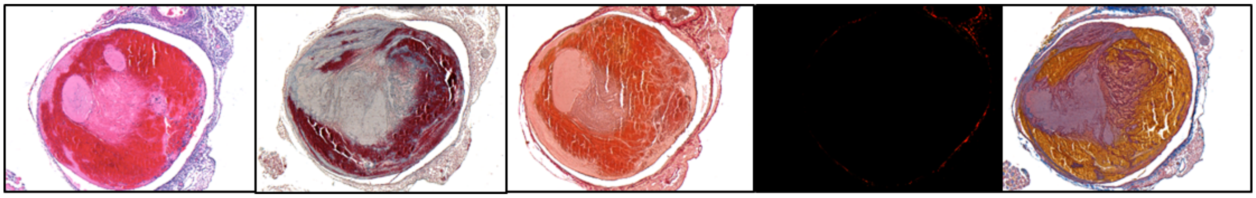

Figure 7.1: Acute thrombus stained with (a) H&E, (b) Masson's Trichrome, (c) Picrosirius, (d) Picrosirius with polarized light, and (e) MSB.

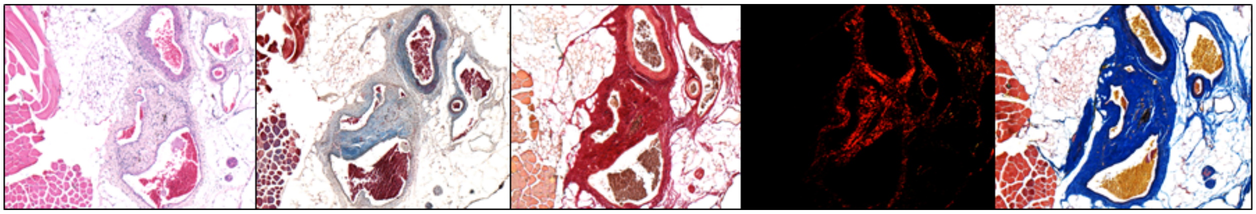

Figure 7.2: Chronic thrombus stained with (a) H&E, (b) Masson's Trichrome, (c) Picrosirius, (d) Picrosirius with polarized light, and (e) MSB.

of fibrin begins at the wall and moves in towards the center of the vessel. Small amounts of Type I collagen were observed around the wall of the IVC. Conversely, the chronic thrombi depicted in Figure 7.2 are composed predominately of collagen and red blood cells. In addition to collagen content, changes in the shape of the IVC were observed between both groups. The IVC wall appeared regular and circular in the acute samples whereas in the chronic group it appears non-regular and non-circular. The change in shape of the IVC is likely due to the fibrosis of the vein wall because of the original thrombotic event. This illustrates the chronic effects that a large thrombotic event has on the vessel wall.

Spatial variation occurs throughout the length of a thrombus and can be seen in Figure 7.3 for the acute group. These variations highlight the heterogeneity of the thrombus structure. We argue that this heterogeneity is greatly dictated by the interplay between hemodynamics and the specifics of enzymatic reactions at time zero. Therefore, it will be necessary to employ a growth and remodeling framework, similar to Humphrey and Rajagopal[66], to study both the acute versus chronic nature of thrombi as well as to study the long term effects of thrombosis on thrombus and vein structure. Creating 3-dimensional computational models of thrombi will also enable investigation into the 3-dimensional heterogeneity of thrombus structure.

Lastly, future work should aim at validating the proposed thrombosis model through the use of either *in vitro* or *in vivo* experiments. For ethical and practical reasons, human samples of thrombosis are not readily available for research. Animal models are often used to study the stages of DVT *in vivo*. Animals do not naturally develop thrombosis so specific methods must be used to artificially induce these events. Currently, models exist to mimic both acute and chronic thrombotic events in small and large animals[37]. These models rely on a combination of stasis, chemical activation and/or of endothelial damage to initiate a thrombotic event. Examples include: a stenosis model, ligation model, and an electrolytic vein model (EIM). Animal models allow researchers to obtain information about thrombosis that would otherwise be impossible and will play a large role in this investigation.

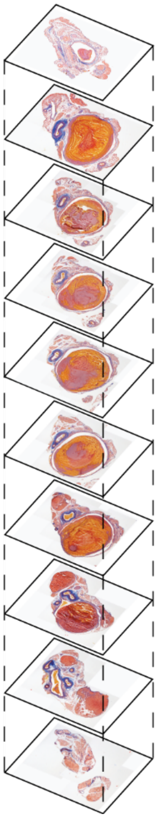

Figure 7.3: MSB stain of axial cross sections for acute thrombus

Ultimately, we hope that the proposed thrombosis models will lead to advancements in thrombosis treatment and prevention. Future work should also include using the developed transport and reaction framework in other applications such as atherosclerosis and drug delivery research.

APPENDICES

APPENDIX A

Three-element Windkessel values used for Aortic and Venous Models

Outlet	Proximal Resistance $(g/(mm^4 \cdot s))$	Capacitance $(mm^4 \cdot s^2/g)$	Distal Resistance $(g/(mm^4 \cdot s))$
RSA	0.19	0.15	2.29
REC	0.63	0.11	7.09
LEC	0.28	0.10	3.28
TA	0.01	5.18	0.22
LSA	0.18	0.15	2.27
LIC	0.19	0.18	2.36
RIC	0.17	0.23	2.19
RVA	0.54	0.09	6.03
LVA	0.44	0.07	4.80

Table A.1: Three-element Windkessel values used for thoracic aortic aneurysm model

RSA- Right subclavian artery

REC - Right external carotid artery

LEC - Left external carotid artery

TA -Thoracic Aorta

LSA- Left subclavian artery

LIC- Left internal carotid artery

RIC- Right internal carotid artery

RVA- Right vertebral artery

LVA- Left vertebral artery

Outlet	**Proximal Resistance (g/(mm^4·s))**	**Capacitance (mm^4· s^2/g)**	**Distal Resistance (g/(mm^4· s))**
IVC	0.0033	3.4	0.063

Table A.2: Three-element Windkessel values used for venous model of the inferior vena cava and iliac veins.

IVC- Inferior vena cava

APPENDIX B

Reaction Models and Associated Parameter Values and Initial Conditions

4-Species Thrombin Model

Species	**Initial Concentration (M)**
RP	0.95
AP	0.05
II	1.4 x 10^{-6}
IIa	0

(a) Prescribed Initial concentrations.

Rate Constant	**Value**	**Units**
$\mathrm{k_{surf}}$	7.223 x 10^{-6}	$\mathrm{s^{-1}}$
$\mathrm{k_{II}^{AP}}$	0.525	$\mathrm{M^{-1}s^{-1}}$
$\mathrm{k_{in}}$	0.0262	$\mathrm{s^{-1}}$
$\mathrm{k_{AP}^{AP}}$	5.24 x 10^{-2}	$\mathrm{M^{-1}s^{-1}}$
$\mathrm{k_{AP}^{IIa}}$	0.002 if [IIa] $\geq 1.0x10^{-8}$	$\mathrm{s^{-1}}$

(b) Rate constants used.

Table B.1: Initial conditions and rate constants used for the 4-species coagulation model.

$$\begin{aligned}
\frac{\mathrm{d[RP]}}{\mathrm{dt}} &= -\mathrm{k_{AP}^{AP}[AP][RP]} - \mathrm{k_{AP}^{IIa}[RP]}, \qquad \text{(B.1)}\\
\frac{\mathrm{d[AP]}}{\mathrm{dt}} &= \mathrm{k_{AP}^{AP}[AP][RP]} + \mathrm{k_{AP}^{IIa}[RP]},\\
\frac{\mathrm{d[II]}}{\mathrm{dt}} &= -(\mathrm{k_{surf}} + \mathrm{k_{II}^{AP}} * \mathrm{[AP]})\mathrm{[II]},\\
\frac{\mathrm{d[IIa]}}{\mathrm{dt}} &= -\mathrm{k_{in}[IIa]} + (\mathrm{k_{surf}} + \mathrm{k_{II}^{AP}[AP]})\mathrm{[II]},
\end{aligned}$$

7-Species Thrombin Model

Species	**Initial Concentration (M)**
TF	1.0×10^{-9}
IIa	0
X	1.6×10^{-7}
II	1.4×10^{-6}
V	2×10^{-8}
Xa:Va	0
IIa:ATIII	0

(a) Prescribed Initial concentrations.

Rate Constant	**Value**	**Units**
k_1	6.93938×10^{20}	$M^{-3}s^{-1}$
k_2	3.49444×10^{3}	$M^{-2}s^{-1}$
k_3	1.48266×10^{8}	$M^{-1}s^{-1}$
k_4	2.82183×10^{-2}	s^{-1}

(b) Rate constants used.

Table B.2: Initial conditions and rate constants used for the 7-species coagulation model.

$$\begin{aligned}
\frac{d[TF]}{dt} &= -k_1[TF][IIa][X][V], \qquad (B.2)\\
\frac{d[IIa]}{dt} &= -k_1[TF][IIa][X][V] + k_2[TF][X][II] + k_3[Xa:Va][II] - k_4[IIa],\\
\frac{d[X]}{dt} &= -k_1[TF][IIa][X][V],\\
\frac{d[II]}{dt} &= -k_2[TF][X][II] - k_3[XaVa][II],\\
\frac{d[V]}{dt} &= -k_1[TF][IIa][X][V],\\
\frac{d[Xa:Va]}{dt} &= k_1[TF][IIa][X][V],\\
\frac{d[IIa:ATIII]}{dt} &= k_4[IIa],
\end{aligned}$$

*Note: The “:” is used to describe the complex of two proteins, i.e. Factor Xa and Factor Va coming together to form the complex Xa:Va

18-Species Thrombin Model

Species	**Initial Concentration (M)**
IX	9.0 x 10^{-8}
TF:VIIa	1 x 10^{-9}
X	1.7 x 10^{-7}
V	2.0 x 10^{-8}
VIII	7.0 x 10^{-10}
VIIa	1.0 x 10^{-10}
II	1.4 x 10^{-6}
IX:TF:VIIa	0
IXa	0
X:TF:VIIa	0
Xa	0
VIIIa:IXa	0
X:VIIIa:IXa	0
Va	0
IIa	0
Va:Xa	0
II:Va:Xa	0
mIIa	0

(a) Prescribed Initial concentrations.

Rate Constant	**Value**	**Units**
k_1	2 x 10^7	$M^{-1}s^{-1}$
k_2	2 x 10^7	$M^{-1}s^{-1}$
k_3	1x 10^7	$M^{-1}s^{-1}$
k_4	2x 10^7	$M^{-1}s^{-1}$
k_5	1x 10^7	$M^{-1}s^{-1}$
k_6	1x 10^8	$M^{-1}s^{-1}$
k_7	1x 10^7	$M^{-1}s^{-1}$
k_8	4x 10^8	$M^{-1}s^{-1}$
k_9	0.005	s^{-1}
$k_1 0$	0.4	s^{-1}
$k_1 1$	0.3	s^{-1}
$k_1 2$	1.15	s^{-1}
$k_1 3$	8.2	s^{-1}
$k_1 4$	32	s^{-1}
$k_1 5$	1x 10^5	$M^{-1}s^{-1}$
$k_1 6$	24	s^{-1}
$k_1 7$	44	s^{-1}
$k_1 8$	0.001	s^{-1}
$k_1 9$	70	s^{-1}

(b) Rate constants used.

Table B.3: Initial conditions and rate constants used for the 18-species coagulation model.

$$\frac{\mathrm{d[IX]}}{\mathrm{dt}} = -\mathrm{k}_6[\mathrm{IX}][\mathrm{TF:VIIa}] + \mathrm{k}_{16}[\mathrm{IX:TF:VIIa}] - \mathrm{k}_{15}[\mathrm{IX}][\mathrm{Xa}], \tag{B.3}$$

$$\begin{aligned}
\frac{\mathrm{d[TF:VIIa]}}{\mathrm{dt}} &= -\mathrm{k}_6[\mathrm{IX}][\mathrm{TfVIIa}] + \mathrm{k}_{16}[\mathrm{IX:TF:VIIa}] - \mathrm{k}_6[\mathrm{X}][\mathrm{TF:VIIa}] \\
&\quad + \mathrm{k}_{17}[\mathrm{X:TF:VIIa}] + \mathrm{k}_{11}[\mathrm{IX:TFVIIa}] + \mathrm{k}_{12}[\mathrm{X:TF:VIIa}], \\
\frac{\mathrm{d[IX:TF:VIIa]}}{\mathrm{dt}} &= \mathrm{k}_6[\mathrm{IX}][\mathrm{TF:VIIa}] - \mathrm{k}_{16}[\mathrm{IX:TF:VIIa}] - \mathrm{k}_{11}[\mathrm{IX:TF:VIIa}], \\
\frac{\mathrm{d[IXa]}}{\mathrm{dt}} &= {\scriptstyle \mathrm{k11}}[\mathrm{IX:TF:VIIa}] + \mathrm{k}_{15}[\mathrm{IX}][\mathrm{Xa}] - \mathrm{k}_7[\mathrm{VIIIa}][\mathrm{IXa}] + \mathrm{k}_9[\mathrm{VIIIa:IXa}], \\
\frac{\mathrm{d[X]}}{\mathrm{dt}} &= -\mathrm{k}_6[\mathrm{X}][\mathrm{TF:VIIa}] + \mathrm{k}_{17}[\mathrm{X:TF:VIIa}] - \mathrm{k}_6[\mathrm{X}][\mathrm{VIIIa:IXa}] \\
&\quad + \mathrm{k}_{18}[\mathrm{X:VIIIa:IXa}], \\
\frac{\mathrm{d[X:TF:VIIa]}}{\mathrm{dt}} &= \mathrm{k}_6[\mathrm{X}][\mathrm{TF:VIIa}] - \mathrm{k}_{17}[\mathrm{X:TF:VIIa}] - \mathrm{k}_{12}[\mathrm{X:TF:VIIa}], \\
\frac{\mathrm{d[Xa]}}{\mathrm{dt}} &= \mathrm{k}_{13}[\mathrm{X:VIIIa:IXa}] + \mathrm{k}_{12}[\mathrm{XTF:VIIa}] - \mathrm{k}_8[\mathrm{Va}][\mathrm{Xa}] + \mathrm{k}_{10}[\mathrm{Va:Xa}],
\end{aligned}$$

$$\begin{aligned}
\frac{\mathrm{d[VIIIa:IXa]}}{\mathrm{dt}} &= -\mathrm{k}_6[\mathrm{X}][\mathrm{VIIIa:IXa}] + \mathrm{k}_{18}[\mathrm{X:VIIIa:IXa}] + \mathrm{k}_{13}[\mathrm{X:VIIIa:IXa}] \\
&\quad + \mathrm{k}_7[\mathrm{VIIIa}][\mathrm{IXa}] - \mathrm{k}_9[\mathrm{VIIIa:IXa}],
\end{aligned} \tag{B.4}$$

$$\begin{aligned}
\frac{\mathrm{d[X:VIIIa:IXa]}}{\mathrm{dt}} &= \mathrm{k}_6[\mathrm{X}][\mathrm{VIIIa:IXa}] - \mathrm{k}_{18}[\mathrm{X:VIIIa:IXa}] - \mathrm{k}_{13}[\mathrm{X:VIIIa:IXa}], \\
\frac{\mathrm{d[V]}}{\mathrm{dt}} &= -\mathrm{k}_1[\mathrm{V}][\mathrm{Xa}] - \mathrm{k}_2[\mathrm{V}][\mathrm{IIa}], \\
\frac{\mathrm{d[Va]}}{\mathrm{dt}} &= \mathrm{k}_1[\mathrm{V}][\mathrm{Xa}] + \mathrm{k}_2[\mathrm{V}][\mathrm{IIa}] - \mathrm{k}_8[\mathrm{Va}][\mathrm{Xa}] + \mathrm{k}_{10}\mathrm{Va:Xa}, \\
\frac{\mathrm{d[VIII]}}{\mathrm{dt}} &= -\mathrm{k}_3[\mathrm{VIII}][\mathrm{Xa}] - \mathrm{k}_4[\mathrm{VIII}][\mathrm{IIa}], \\
\frac{\mathrm{d[VIIIa]}}{\mathrm{dt}} &= \mathrm{k}_3[\mathrm{VIII}][\mathrm{Xa}] + \mathrm{k}_4[\mathrm{VIII}][\mathrm{IIa}] - \mathrm{k}_7[\mathrm{VIIIa}][\mathrm{IXa}] + \mathrm{k}_9[\mathrm{VIIIa:IXa}], \\
\frac{\mathrm{d[IIa]}}{\mathrm{dt}} &= \mathrm{k}_5[\mathrm{mIIa}][\mathrm{VaXa}], \\
\frac{\mathrm{d[II]}}{\mathrm{dt}} &= -\mathrm{k}_6[\mathrm{II}][\mathrm{Va:Xa}] + \mathrm{k}_{19}[\mathrm{II:Va:Xa}], \\
\frac{\mathrm{d[Va:Xa]}}{\mathrm{dt}} &= -\mathrm{k}_6[\mathrm{II}][\mathrm{Va:Xa}] + \mathrm{k}_{19}[\mathrm{II:Va:Xa}] + \mathrm{k}_{14}[\mathrm{II:Va:Xa}] + \mathrm{k}_8[\mathrm{Va}][\mathrm{Xa}] - \mathrm{k}_{10}[\mathrm{Va:Xa}], \\
\frac{\mathrm{d[II:Va:Xa]}}{\mathrm{dt}} &= \mathrm{k}_6[\mathrm{II}][\mathrm{VaXa}] - \mathrm{k}_{19}[\mathrm{II:Va:Xa}] - \mathrm{k}_{14}[\mathrm{II:Va:Xa}], \\
\frac{\mathrm{d[mIIa]}}{\mathrm{dt}} &= \mathrm{k}_{14}[\mathrm{II:Va:Xa}] - \mathrm{k}_5[\mathrm{mIIa}][\mathrm{Va:Xa}],
\end{aligned}$$

BIBLIOGRAPHY

BIBLIOGRAPHY

[1] Abraham, F., Behr, M., and Heinkenschloss, M. Shape optimization in steady blood flow: A numerical study of non-Newtonian effects. *Computer Methods in Biomechanics and Biomedical Engineering 8*, 2 (4 2005), 127–137.

[2] Alshehri, A. M. Stroke in atrial fibrillation: Review of risk stratification and preventive therapy. *Journal of family & community medicine 26*, 2 (2019), 92–97.

[3] Alwan, A. Global status report on noncommunicable diseases 2010. *Global status report on noncommunicable diseases 2010.* (2011).

[4] Anand, M., Rajagopal, K., and Rajagopal, K. R. A model for the formation, growth, and lysis of clots in quiescent plasma. A comparison between the effects of antithrombin III deficiency and protein C deficiency. *Journal of Theoretical Biology 253*, 4 (8 2008), 725–738.

[5] Arthurs, C. J., Agarwal, P., John, A. V., Dorfman, A. L., Grifka, R. G., and Figueroa, C. A. Reproducing patient-specific hemodynamics in the Blalock-Taussig circulation using a flexible multi-domain simulation framework: Applications for optimal shunt design. *Frontiers in Pediatrics 5* (4 2017).

[6] Arthurs, C. J., Khlebnikov, R., Melville, A., Marčan, M., Gomez, A., Dillon-Murphy, D., Cuomo, F., Vieira, M. S., Schollenberger, J., and Lynch, S. R. e. a. CRIMSON: An Open-Source Software Framework for Cardiovascular Integrated Modelling and Simulation. *bioRxiv* (2020).

[7] Arumugam, J., and Srinivasa, A. A Novel Simplified Model for Blood Coagulation: A piecewise dynamical model for thrombin with robust predictive capabilities. *arXiv* (2017), 1–20.

[8] Arzani, A., Gambaruto, A. M., Chen, G., and Shadden, S. C. Lagrangian wall shear stress structures and near-wall transport in high-schmidt-number aneurysmal flows. *Journal of Fluid Mechanics 790* (2016), 158–172.

[9] Aycock, K. I., Campbell, R. L., Lynch, F. C., Manning, K. B., and Craven, B. A. The Importance of Hemorheology and Patient Anatomy on the Hemodynamics in the Inferior Vena Cava. *Annals of Biomedical Engineering* (2016).

[10] Bark, D. L., and Ku, D. N. Wall shear over high degree stenoses pertinent to atherothrombosis. *Journal of Biomechanics 43*, 15 (11 2010), 2970–2977.

[11] Bernsdorf, J., and Wang, D. Non-Newtonian blood flow simulation in cerebral aneurysms. *Computers and Mathematics with Applications 58*, 5 (9 2009), 1024–1029.

[12] Bertoglio, C., and Caiazzo, A. A tangential regularization method for backflow stabilization in hemodynamics. *Journal of Computational Physics 261* (2014), 162–171.

[13] Bertoglio, C., Caiazzo, A., Bazilevs, Y., Braack, M., Esmaily, M., Gravemeier, V., L. Marsden, A., Pironneau, O., E. Vignon-Clementel, I., and A. Wall, W. Benchmark problems for numerical treatment of backflow at open boundaries. *International journal for numerical methods in biomedical engineering 34*, 2 (2018), e2918.

[14] Biasetti, J., Gasser, T. C., Auer, M., Hedin, U., and Labruto, F. Hemodynamics of the normal aorta compared to fusiform and saccular abdominal aortic aneurysms with emphasis on a potential thrombus formation mechanism. *Annals of biomedical engineering 38*, 2 (2 2010), 380–90.

[15] Biasetti, J., Hussain, F., and Gasser, T. C. Blood flow and coherent vortices in the normal and aneurysmatic aortas: a fluid dynamical approach to intra-luminal thrombus formation. *Journal of The Royal Society Interface 8*, 63 (2011), 1449–1461.

[16] Biasetti, J., Spazzini, P. G., Swedenborg, J., and Christian Gasser, T. An integrated fluid-chemical model toward modeling the formation of intra-luminal thrombus in abdominal aortic aneurysms. *Frontiers in Physiology 3 JUL*, July (2012), 1–16.

[17] Boyd, J., Buick, J. M., and Green, S. Analysis of the Casson and Carreau-Yasuda non-Newtonian blood models in steady and oscillatory flows using the lattice Boltzmann method. *Physics of Fluids 19*, 9 (9 2007), 093103.

[18] Braack, M., and Mucha, P. B. Directional Do-Nothing Condition for the Navier-Stokes Equations. *Source: Journal of Computational Mathematics 32*, 5 (2014), 507–521.

[19] Brooks, A. N., and Hughes, T. J. Streamline upwind/petrov-galerkin formulations for convection dominated flows with particular emphasis on the incompressible navier-stokes equations. *Computer methods in applied mechanics and engineering 32*, 1-3 (1982), 199–259.

[20] Brooks, A. N., and Hughes, T. J. Streamline upwind/Petrov-Galerkin formulations for convection dominated flows with particular emphasis on the incompressible Navier-Stokes equations. *Computer Methods in Applied Mechanics and Engineering 32*, 1-3 (1982), 199–259.

[21] Bruneau, C.-H., and Fabrie, P. Effective downstream boundary conditions for incompressible Navier-Stokes equations. *International Journal for Numerical Methods in Fluids 19*, 8 (10 1994), 693–705.

[22] Bruneau, C.-H., and Fabrie, P. New efficient boundary conditions for incompressible navier-stokes equations : a well-posedness result. *ESAIM: Mathematical Modelling and Numerical Analysis - Modélisation Mathématique et Analyse Numérique 30*, 7 (1996), 815–840.

[23] Bungay, S. D. A mathematical model of lipid-mediated thrombin generation. *Mathematical Medicine and Biology 20*, 1 (2003), 105–129.

[24] Burroughs, K. E. New Considerations in the Diagnosis and Therapy of Deep Vein Thrombosis. *Southern Medical Journal 92*, 5 (5 1999), 517–520.

[25] Butros, S. R., Liu, R., Oliveira, G. R., Ganguli, S., and Kalva, S. Venous compression syndromes: Clinical features, imaging findings and management, 10 2013.

[26] Catabriga, L., and Coutinho, A. L. G. A. Improving convergence to steady state of implicit SUPG solution of Euler equations. *Communications in Numerical Methods in Engineering 18*, 5 (3 2002), 345–353.

[27] Ceretani, A. N., and Rautenberg, C. N. The Boussinesq system with mixed non-smooth boundary conditions and do-nothing boundary flow. *Zeitschrift für angewandte Mathematik und Physik 70* (2019).

[28] Cheng, A. L., Pahlevan, N. M., and Wood, J. C. Non-Newtonian behavior significantly affects hemodynamic efficiency in a four-dimensional flow magnetic resonance Fontan model. *Journal of the American College of Cardiology 71* (2018), A622.

[29] Chung, J., and Hulbert, G. M. A Time Integration Algorithm for Structural Dynamics With Improved Numerical Dissipation: The Generalized-α Method. *Journal of Applied Mechanics 60*, 2 (06 1993), 371–375.

[30] Chung, M., Shiloh, A. L., and Carlese, A. Monitoring of the adult patient on venoarterial extracorporeal membrane oxygenation. *The Scientific World Journal 2014* (2014).

[31] Cobbe, S. M. Sudden cardiac death and acute coronary thrombosis. *British Medical Journal (Clinical research ed.) 290*, 6462 (1 1985), 93–94.

[32] Codina, R. A discontinuity-capturing crosswind-dissipation for the finite element solution of the convection-diffusion equation. *Computer Methods in Applied Mechanics and Engineering 110*, 3-4 (1993), 325–342.

[33] Coppola, G., and Caro, C. Arterial geometry, flow pattern, wall shear and mass transport: Potential physiological significance. *Journal of the Royal Society Interface 6*, 35 (6 2009), 519–528.

[34] Dave, H. D., and LaPelusa, A. *Physiology, Hemostasis.* StatPearls Publishing, 7 2019.

[35] De Sampaio, P., and Coutinho, A. L. G. d. A. A natural derivation of discontinuity capturing operator for convection–diffusion problems. *Computer methods in applied mechanics and engineering 190*, 46-47 (2001), 6291–6308.

[36] Di Achille, P., Tellides, G., Figueroa, C. A., and Humphrey, J. D. A haemodynamic predictor of intraluminal thrombus formation in abdominal aortic aneurysms. *Proceedings of the Royal Society A: Mathematical, Physical and Engineering Sciences 470*, 2172 (2014), 20140163–20140163.

[37] Diaz, J. A., Obi, A. T., Myers, D. D., Wrobleski, S. K., Henke, P. K., MacKman, N., and Wakefield, T. W. Critical review of mouse models of venous thrombosis, 2012.

[38] Diaz José A., Ballard-Lipka NE, F. D. e. a. Impaired fibrinolytic system in ApoE null mice with hyperlipidemia augments deep vein thrombosis. *Journal of Vascular Surgery 55*, 3 (2012), 815–822.

[39] DiCarlo, A. L., Holdsworth, D. W., and Poepping, T. L. Study of the effect of stenosis severity and non-Newtonian viscosity on multidirectional wall shear stress and flow disturbances in the carotid artery using particle image velocimetry. *Med Eng Phys. 65* (3 2019), 8–23.

[40] Dillon-Murphy, D., Noorani, A., Nordsletten, D., and Figueroa, C. A. Multi-modality image-based computational analysis of haemodynamics in aortic dissection. *Biomechanics and Modeling in Mechanobiology* (2016).

[41] Dong, S. A convective-like energy-stable open boundary condition for simulations of incompressible flows. *Journal of Computational Physics 302* (12 2015), 300–328.

[42] Dong, S., Karniadakis, G. E., and Chryssostomidis, C. A robust and accurate outflow boundary condition for incompressible flow simulations on severely-truncated unbounded domains. *Journal of Computational Physics 261* (3 2014), 83–105.

[43] Dong, S., and Shen, J. A pressure correction scheme for generalized form of energy-stable open boundary conditions for incompressible flows. *Journal of Computational Physics 291* (6 2015), 254–278.

[44] Esmon, C. T. Basic mechanisms and pathogenesis of venous thrombosis. *Blood Reviews 23*, 5 (9 2009), 225–229.

[45] Ethier, C. R. Computational modeling of mass transfer and links to atherosclerosis. *Annals of Biomedical Engineering 30*, 4 (2002), 461–471.

[46] Etufugh, C. N., and Phillips, T. J. Venous ulcers. *Clinics in Dermatology 25*, 1 (2007), 121–130.

[47] Farghadan, A., and Arzani, A. The combined effect of wall shear stress topology and magnitude on cardiovascular mass transport. *International Journal of Heat and Mass Transfer 131* (2019), 252–260.

[48] Feistauer, M., and Neustupa, T. On the Existence of a Weak Solution of Viscous Incompressible Flow Past a Cascade of Profiles with an Arbitrarily Large Inflow. *J. Math. Fluid Mech 15* (2013), 701–715.

[49] Folie, B. J., and Mclntire, L. V. Mathematical analysis of mural thrombogenesis. *Biophysical Journal 56*, December (1989), 1122–1141.

[50] Ford, M. D., Stuhne, G. R., Nikolov, H. N., Habets, D. F., Lownie, S. P., Holdsworth, D. W., and Steinman, D. A. Virtual angiography for visualization and validation of computational models of aneurysm hemodynamics. *IEEE Transactions on Medical Imaging 24*, 12 (12 2005), 1586–1592.

[51] Fouchet-Incaux, J. Artificial boundaries and formulations for the incompressible navier–stokes equations: applications to air and blood flows. *SeMA Journal 64*, 1 (2014), 1–40.

[52] Furie, B., and Furie, B. C. In vivo thrombus formation. *Journal of Thrombosis and Haemostasis 5*, SUPPL. 1 (2007), 12–17.

[53] Furlan, M. Von Willebrand factor: Molecular size and functional activity, 6 1996.

[54] Gravemeier, V., Comerford, A., Yoshihara, L., Ismail, M., and Wall, W. A. A novel formulation for neumann inflow boundary conditions in biomechanics. *International Journal for Numerical Methods in Biomedical Engineering 28*, 5 (2012), 560–573.

[55] Griffiths, D. F. The 'no boundary condition' outflow boundary condition. *International Journal for Numerical Methods in Fluids 24*, 4 (1997), 393–411.

[56] Grosse, S. D., Nelson, R. E., Nyarko, K. A., Richardson, L. C., and Raskob, G. E. The economic burden of incident venous thromboembolism in the United States: A review of estimated attributable healthcare costs, 2016.

[57] Hansen, K. B., Arzani, A., and Shadden, S. C. Finite element modeling of near-wall mass transport in cardiovascular flows. *International Journal for Numerical Methods in Biomedical Engineering 35*, 1 (2019), 1–15.

[58] Hansen, K. B., Arzani, A., and Shadden, S. C. Finite element modeling of near-wall mass transport in cardiovascular flows. *International Journal for Numerical Methods in Biomedical Engineering 35*, 1 (1 2019), e3148.

[59] Hansen, K. B., and Shadden, S. C. Automated reduction of blood coagulation models. *International Journal for Numerical Methods in Biomedical Engineering 35*, 10 (10 2019).

[60] Hathcock, J. J. Flow effects on coagulation and thrombosis. *Arteriosclerosis, thrombosis, and vascular biology 26*, 8 (2006), 1729–1737.

[61] Hockin, M. F., Jones, K. C., Everse, S. J., and Mann, K. G. A model for the stoichiometric regulation of blood coagulation. *Journal of Biological Chemistry 277*, 21 (2002), 18322–18333.

[62] Hockin, M. F., Jones, K. C., Everse, S. J., and Mann, K. G. A model for the stoichiometric regulation of blood coagulation. *Journal of Biological Chemistry 277*, 21 (5 2002), 18322–18333.

[63] Holinstat, M. Normal platelet function. *Cancer and Metastasis Reviews 36*, 2 (6 2017), 195–198.

[64] Hughes, T. J., and Mallet, M. A new finite element formulation for computational fluid dynamics: Iv. a discontinuity-capturing operator for multidimensional advective-diffusive systems. *Computer Methods in Applied Mechanics and Engineering 58*, 3 (1986), 329–336.

[65] Hughes, T. J., and Wells, G. N. Conservation properties for the galerkin and stabilised forms of the advection–diffusion and incompressible navier–stokes equations. *Computer methods in applied mechanics and engineering 194*, 9-11 (2005), 1141–1159.

[66] Humphrey, J. D., and Rajagopal, K. R. A constrained mixture model for growth and remodeling of soft tissues. *Mathematical Models and Methods in Applied Sciences 12*, 3 (11 2002), 407–430.

[67] JA, K., and Masud, A. A stabilized mixed finite element method for shear-rate dependent non-Newtonian fluids: 3D benchmark problems and application to blood flow in bifurcating arteries. *Comput Mech* (2013), 20–22.

[68] Jackson, S. P. Arterial thrombosis-insidious, unpredictable and deadly, 11 2011.

[69] Jayaraman, A., Cormican, D., Shah, P., and Ramakrishna, H. Cannulation strategies in adult veno-arterial and veno-venous extracorporeal membrane oxygenation: Techniques, limitations, and special considerations, 1 2017.

[70] Jones, K. C., and Mann, K. G. A model for the tissue factor pathway to thrombin. ii. a mathematical simulation. *Journal of Biological Chemistry 269*, 37 (1994), 23367–23373.

[71] Kaazempur-Mofrad, M. R., Wada, S., Myers, J. G., and Ethier, C. R. Mass transport and fluid flow in stenotic arteries: Axisymmetric and asymmetric models. *International Journal of Heat and Mass Transfer 48*, 21-22 (10 2005), 4510–4517.

[72] Kahl, F. R., Hackshaw, B. T., and Headley, R. N. Coronary Artery Thrombus. *Southern Medical Journal 74*, 6 (6 1981), 751–752.

[73] Kibbe, M. R., Ujiki, M., Goodwin, A. L., Eskandari, M., Yao, J., Matsumura, J., Gloviczki, P., and Bassiouny, H. Iliac vein compression in an asymptomatic patient population. *Journal of Vascular Surgery 39*, 5 (5 2004), 937–943.

[74] Kim, H. J., Figueroa, C. A., Hughes, T., Jansen, K., and Taylor, C. Augmented lagrangian method for constraining the shape of velocity profiles at outlet boundaries for three-dimensional finite element simulations of blood flow. *Computer Methods in Applied Mechanics and Engineering 198*, 45-46 (2009), 3551–3566.

[75] Kim, J. Y., Choi, D., Guk Ko, Y., Park, S., Jang, Y., and Lee, D. Y. Percutaneous treatment of deep vein thrombosis in May-Thurner syndrome. *CardioVascular and Interventional Radiology* (2006).

[76] Klug, P., Lawrence, L., and Peter, R. Rheological Aspects Sickle Cell Disease. *Archives of Internal Medicine 133* (1974), 577–590.

[77] Lanzendörfer, M., and Stebel, J. On pressure boundary conditions for steady flows of incompressible fluids with pressure and shear rate dependent viscosities. *Applications of Mathematics 56*, 3 (2011), 265–285.

[78] Lawson, J. H., Kalafatis, M., Stram, S., and Mann, K. G. A model for the tissue factor pathway to thrombin. i. an empirical study. *Journal of Biological Chemistry 269*, 37 (1994), 23357–23366.

[79] Le Beau, G. J., Ray, S. E., Aliabadi, S. K., and Tezduyar, T. E. SUPG finite element computation of compressible flows with the entropy and conservation variables formulations. *Computer Methods in Applied Mechanics and Engineering 104*, 3 (1993), 397–422.

[80] Lee, S. W., Antiga, L., and Steinman, D. A. Correlations among indicators of disturbed flow at the normal carotid bifurcation. *Journal of Biomechanical Engineering 131*, 6 (6 2009).

[81] Leiderman, K., and Fogelson, A. L. Grow with the flow: a spatial–temporal model of platelet deposition and blood coagulation under flow. *Mathematical medicine and biology 28*, 1 (2011), 47–84.

[82] Les, A. S., Shadden, S. C., Figueroa, C. A., Park, J. M., Tedesco, M. M., Herfkens, R. J., Dalman, R. L., Taylor, C. A., Center, J. H. C., Biomed, A., and Author, E. Quantification of Hemodynamics in Abdominal Aortic Aneurysms During Rest and Exercise Using Magnetic Resonance Imaging and Computational Fluid Dynamics HHS Public Access Author manuscript. *Ann Biomed Eng 38*, 4 (2010), 1288–1313.

[83] Liu, X., and Liu, L. Effect of valve lesion on venous valve cycle: A modified immersed finite element modeling. *PLoS ONE 14*, 3 (3 2019), e0213012.

[84] Liu, X., Xie, Z., and Dong, S. On a simple and effective thermal open boundary condition for convective heat transfer problems. *International Journal of Heat and Mass Transfer 151* (4 2020), 119355.

[85] Lozano, R., Naghavi, M., and Foreman, K. e. a. Global and regional mortality from 235 causes of death for 20 age groups in 1990 and 2010: A systematic analysis for the Global Burden of Disease Study 2010. *The Lancet 380*, 9859 (12 2012), 2095–2128.

[86] Lugo-Fagundo, C., Nance, J. W., Johnson, P. T., and Fishman, E. K. May–Thurner syndrome: MDCT findings and clinical correlates, 10 2016.

[87] Lynch, S. R., Nama, N., Xu, Z., Arthurs, C. J., Sahni, O., and Figueroa, C. A. Numerical Considerations for Advection-Diffusion Problems in Cardiovascular Hemodynamics. *International Journal for Numerical Methods in Biomedical Engineering* (6 2020).

[88] Mach, G., Sherif, C., Windberger, U., Plasenzotti, R., and Gruber, A. A Non Newtonian Model for Blood Flow behind a Flow Diverting Stent. *Proceedings of the 2016 COMSOL Conference* (2016), 3–6.

[89] Mackman, N., Tilley, R. E., and Key, N. S. Role of the extrinsic pathway of blood coagulation in hemostasis and thrombosis, 8 2007.

[90] Marrero, V. L., Tichy, J. A., Sahni, O., and Jansen, K. E. Numerical study of purely viscous non-newtonian flow in an abdominal aortic aneurysm. *Journal of Biomechanical Engineering 136*, 10 (2014).

[91] Martin, P. J., Counts, G. W., Appelbaum, F. R., Lee, S. J., Sanders, J. E., Deeg, H. J., Flowers, M. E. D., Syrjala, K. L., Hansen, J. A., Storb, R. F., and Storer, B. E. Life expectancy in patients surviving more than 5 years after hematopoietic cell transplantation. *Journal of Clinical Oncology 28*, 6 (2010), 1011–1016.

[92] Mathers, C. D., Boerma, T., and Ma Fat, D. Global and regional causes of death\r10.1093/bmb/ldp028 . *British Medical Bulletin 92* (1 2009), 7–32.

[93] Mehri, R., Mavriplis, C., and Fenech, M. Red blood cell aggregates and their effect on non-Newtonian blood viscosity at low hematocrit in a two-fluid low shear rate microfluidic system. *PLoS ONE 13*, 7 (7 2018).

[94] Menichini, C., Cheng, Z., Gibbs, R. G. J., and Xu, X. Y. Predicting false lumen thrombosis in patient-specific models of aortic dissection. *The Royal Society* (2016).

[95] Menichini, C., Cheng, Z., Gibbs, R. G. J., and Yun, X. A computational model for false lumen thrombosis in type B aortic dissection following thoracic endovascular repair. *Journal of Biomechanics 66* (2018), 36–43.

[96] Menichini, C., and Xu, X. Y. Mathematical modeling of thrombus formation in idealized models of aortic dissection: initial findings and potential applications. *Journal of Mathematical Biology* (2016), 1–22.

[97] Moghadam, M. E., Bazilevs, Y., Hsia, T.-Y., Vignon-Clementel, I. E., Marsden, A. L., et al. A comparison of outlet boundary treatments for prevention of backflow divergence with relevance to blood flow simulations. *Computational Mechanics 48*, 3 (2011), 277–291.

[98] Nauta, F. J., Lau, K. D., Arthurs, C. J., Eagle, K. A., Williams, D. M., Trimarchi, S., Patel, H. J., and Figueroa, C. A. Computational Fluid Dynamics and Aortic Thrombus Formation Following Thoracic Endovascular Aortic Repair. *The Annals of Thoracic Surgery 103*, 6 (2017), 1914–1921.

[99] Neustupa, T. The weak solvability of the steady problem modelling the flow of a viscous incompressible heat-conductive fluid through the profile cascade. *International Journal of Numerical Methods for Heat & Fluid Flow 27*, 7 (2017), 1451–1466.

[100] Ni, N., Yang, Z., and Dong, S. Energy-stable boundary conditions based on a quadratic form: Applications to outflow/open-boundary problems in incompressible flows. *Journal of Computational Physics 391* (8 2019), 179–215.

[101] Oğuzkurt, L., Özkan, U., Tercan, F., and Koç, Z. Ultrasonographic diagnosis of iliac vein compression (May-Thurner) syndrome. *Diagn Interv Radiol* (2007).

[102] Oshima, M., Torii, R., Kobayashi, T., Taniguchi, N., and Takagi, K. Finite element simulation of blood flow in the cerebral artery. *Computer methods in applied mechanics and engineering 191*, 6-7 (2001), 661–671.

[103] Papadopoulos, K. P., Gavaises, M., and Atkin, C. A simplified mathematical model for thrombin generation. *Medical Engineering and Physics 36*, 2 (2014), 196–204.

[104] Papadopoulos, K. P., Gerotziafas, G. T., and Gavaises, M. Modelling of thrombin generation under flow in realistic left anterior descending geometries. *Medical Engineering and Physics 50* (12 2017), 50–58.

[105] Papaioannou, T. G., Karatzis, E. N., Vavuranakis, M., Lekakis, J. P., and Stefanadis, C. Assessment of vascular wall shear stress and implications for atherosclerotic disease, 10 2006.

[106] Papanastasiou, T. C., Malamataris, N., and Ellwood, K. A new outflow boundary condition. *International Journal for Numerical Methods in Fluids 14*, 5 (1992), 587–608.

[107] Pavlushko, E., Berman, M., and Valchanov, K. Cannulation techniques for extracorporeal life support, 2 2017.

[108] Pérez, C. E., Thomas, J.-M., Blancher, S., and Creff, R. The steady Navier-Stokes/energy system with temperature-dependent viscosity-Part 1: Analysis of the continuous problem. *International Journal for Numerical Methods in Fluids 56*, 1 (1 2008), 63–89.

[109] Pérez, C. E., Thomas, J.-M., Blancher, S., and Creff, R. The steady Navier-Stokes/energy system with temperature-dependent viscosity-Part 2: The discrete problem and numerical experiments. *International Journal for Numerical Methods in Fluids 56*, 1 (1 2008), 91–114.

[110] Perktold, K., Leuprecht, A., Prosi, M., Berk, T., Czerny, M., Trubel, W., and Schima, H. Fluid dynamics, wall mechanics, and oxygen transfer in peripheral bypass anastomoses. *Annals of Biomedical Engineering 30*, 4 (2002), 447–460.

[111] Perktold, K., and Rappitsch, G. Computer simulation of local blood flow and vessel mechanics in a compliant carotid artery bifurcation model. *Journal of biomechanics 28*, 7 (1995), 845–856.

[112] Perktold, K., Resch, M., and Peter, R. O. Three-dimensional numerical analysis of pulsatile flow and wall shear stress in the carotid artery bifurcation. *Journal of Biomechanics 24*, 6 (1 1991), 409–420.

[113] Peters, M., Syed, R. K., Katz, M., Moscona, J., Press, C., Nijjar, V., Bisharat, M., and Baldwin, D. May-Thurner Syndrome: A Not So Uncommon Cause of a Common Condition. *Baylor University Medical Center Proceedings 25*, 3 (7 2012), 231–233.

[114] Porpora, A., Zunino, P., Vergara, C., and Piccinelli, M. Numerical treatment of boundary conditions to replace lateral branches in hemodynamics. *International Journal for Numerical Methods in Biomedical Engineering 28*, 12 (12 2012), 1165–1183.

[115] Pries, A., and Secomb, T. Rheology of the microcirculation, 2003.

[116] Raffini, L., Raybagkar, D., Cahill, A. M., Kaye, R., Blumenstein, M., and Manno, C. May–Thurner syndrome (iliac vein compression) and thrombosis in adolescents. *Pediatric Blood & Cancer 47*, 6 (11 2006), 834–838.

[117] Rao, P., Khalpey, Z., Smith, R., Burkhoff, D., and Kociol, R. D. Venoarterial Extracorporeal Membrane Oxygenation for Cardiogenic Shock and Cardiac Arrest Cardinal Considerations for Initiation and Management Circulation: Heart Failure. *Circ Heart Fail 11* (2018), 4905.

[118] Rayz, V. L., Boussel, L., Ge, L., Leach, J. R., Martin, A. J., Lawton, M. T., McCulloch, C., and Saloner, D. Flow residence time and regions of intraluminal thrombus deposition in intracranial aneurysms. *Annals of Biomedical Engineering 38*, 10 (10 2010), 3058–3069.

[119] Razaghi, R., Karimi, A., Rahmani, S., and Navidbakhsh, M. A computational fluid–structure interaction model of the blood flow in the healthy and varicose saphenous vein. *Vascular 24*, 3 (2016), 254–263.

[120] Razavi, A., Shirani, E., and Sadeghi, M. R. Numerical simulation of blood pulsatile flow in a stenosed carotid artery using different rheological models. *Journal of Biomechanics 44*, 11 (7 2011), 2021–2030.

[121] Renardy, M. Imposing 'no' boundary condition at outflow: Why does it work? *International Journal for Numerical Methods in Fluids 24*, 4 (1997), 413–417.

[122] Saeed, D., Stosik, H., Islamovic, M., Albert, A., Kamiya, H., Maxhera, B., and Lichtenberg, A. Femoro-Femoral Versus Atrio-Aortic Extracorporeal Membrane Oxygenation: Selecting the Ideal Cannulation Technique. *Artificial Organs 38*, 7 (7 2014), 549–555.

[123] Sagar, A., and Varner, J. Dynamic Modeling of the Human Coagulation Cascade Using Reduced Order Effective Kinetic Models. *Processes 3*, 1 (2015), 178–203.

[124] Saposnik, G., Gladstone, D., Raptis, R., Zhou, L., and Hart, R. G. Atrial fibrillation in ischemic stroke: Predicting response to thrombolysis and clinical outcomes. *Stroke 44*, 1 (1 2013), 99–104.

[125] Schirmer, C. M., and Malek, A. Wall shear stress gradient analysis within an idealized stenosis using non-Newtonian flow. *Neurosurgery 61*, 4 (10 2007), 853–864.

[126] Scott, T. E., LaMorte, W. W., Gorin, D. R., and Menzoian, J. O. Risk factors for chronic venous insufficiency: A dual case-control study. *Journal of Vascular Surgery 22*, 5 (1995), 622–628.

[127] Seo, J. H., Abd, T., George, R. T., and Mittal, R. A coupled chemo-fluidic computational model for thrombogenesis in infarcted left ventricles. *American Journal of Physiology-Heart and Circulatory Physiology 310*, 11 (6 2016), H1567–H1582.

[128] Shadden, S. C., and Hendabadi, S. Potential fluid mechanic pathways of platelet activation. *Biomechanics and Modeling in Mechanobiology 12*, 3 (6 2013), 467–474.

[129] Shang, J. K., Esmaily, M., Verma, A., Reinhartz, O., Figliola, R. S., Hsia, T. Y., Feinstein, J. A., and Marsden, A. L. Patient-Specific Multiscale Modeling of the Assisted Bidirectional Glenn. *Annals of Thoracic Surgery 107*, 4 (4 2019), 1232–1239.

[130] Tarbell, J. M. Mass Transport in Arteries and the Localization of Atherosclerosis. *Annual Review of Biomedical Engineering 5*, 1 (8 2003), 79–118.

[131] Taylor, C. A., Hughes, T. J., and Zarins, C. K. Finite element modeling of blood flow in arteries. *Computer Methods in Applied Mechanics and Engineering 158*, 1-2 (5 1998), 155–196.

[132] Unger, E. C., McCreery, T. P., Sweitzer, R. H., Shen, D., and Wu, G. In vitro studies of a new thrombus-specific ultrasound contrast agent. *Am J Cardiol 81*, 12A (1998), 58G–61G.

[133] van Bakel, T. M., Arthurs, C. J., van Herwaarden, J. A., Moll, F. L., Eagle, K. A., Patel, H. J., Trimarchi, S., and Figueroa, C. A. A computational analysis of different endograft designs for zone 0 aortic arch repair. *European Journal of Cardio-Thoracic Surgery 54*, 2 (2018), 389–396.

[134] Vignon-Clementel, I. E., Figueroa, C. A., Jansen, K., and Taylor, C. A. Outflow boundary conditions for 3D simulations of non-periodic blood flow and pressure fields in deformable arteries. *Computer Methods in Biomechanics and Biomedical Engineering 13*, 5 (10 2010), 625–640.

[135] Vignon-Clementel, I. E., Figueroa, C. A., Jansen, K. E., and Taylor, C. A. Outflow boundary conditions for three-dimensional finite element modeling of blood flow and pressure in arteries. *Computer methods in applied mechanics and engineering 195*, 29-32 (2006), 3776–3796.

[136] Virmani, R., Burke, A. P., and Farb, A. Sudden cardiac death. *Cardiovascular Pathology 10*, 5 (9 2001), 211–218.

[137] von Brühl, M.-L., Stark, K., Steinhart, A., Chandraratne, S., Konrad, I., Lorenz, M., Khandoga, A., Tirniceriu, A., Coletti, R., Köllnberger, M., Byrne, R. A., Laitinen, I., Walch, A., Brill, A., Pfeiler, S., Manukyan, D., Braun, S., Lange, P., Riegger, J., Ware, J., Eckart, A., Haidari, S., Rudelius, M., Schulz, C., Echtler, K., Brinkmann, V., Schwaiger, M., Preissner, K. T., Wagner, D. D., Mackman, N., Engelmann, B., and Massberg, S. Monocytes, neutrophils, and platelets cooperate to initiate and propagate venous thrombosis in mice in vivo. *The Journal of Experimental Medicine 209*, 4 (2012), 819–835.

[138] Vorobtsova, N., Chiastra, C., Stremler, M. A., Sane, D. C., Migliavacca, F., and Vlachos, P. Effects of Vessel Tortuosity on Coronary Hemodynamics: An Idealized and Patient-Specific Computational Study. *Annals of Biomedical Engineering 44*, 7 (7 2016), 2228–2239.

[139] Wang, D., and Bernsdorf, J. Lattice Boltzmann simulation of steady non-Newtonian blood flow in a 3D generic stenosis case. *Computers and Mathematics with Applications 58*, 5 (9 2009), 1030–1034.

[140] Weddell, J. C., Kwack, J. H., Imoukhuede, P. I., and Masud, A. Hemodynamic analysis in an idealized artery tree: Differences in wall shear stress between Newtonian and non-Newtonian blood models. *PLoS ONE 10*, 4 (4 2015).

[141] Weisel, J. W., and Litvinov, R. I. Fibrin formation, structure and properties. *Sub-Cellular Biochemistry 82* (1 2017), 405–456.

[142] Weiss, R. A., Heagle, C. R., and Raymond-Martimbeau, P. The Bulletin of the North American Society of Phlebology. Insurance Advisory Committee Report. *The Journal of dermatologic surgery and oncology 18*, 7 (1992), 609–616.

[143] Welsh, J. D., Hoofnagle, M. H., Bamezai, S., Oxendine, M., Lim, L., Hall, J. D., Yang, J., Schultz, S., Engel, J. D., Kume, T., Oliver, G., Jimenez, J. M., and Kahn, M. L. Hemodynamic regulation of perivalvular endothelial gene expression prevents deep venous thrombosis. *Journal of Clinical Investigation 129*, 12 (12 2019), 5489–5500.

[144] Wendelboe, A. M., and Raskob, G. E. Global Burden of Thrombosis: Epidemiologic Aspects. *Circulation Research 118*, 9 (4 2016), 1340–1347.

[145] Whiting, C. H., and Jansen, K. E. A stabilized finite element method for the incompressible Navier–Stokes equations using a hierarchical basis. *International Journal for Numerical Methods in Fluids 35*, 1 (1 2001), 93–116.

[146] Widmayer, E. p., Raff, H., and Strang, K. T. *Vander's Human Physiology.* No. 1. 2014.

[147] Wilson, N., Wang, K., Dutton, R. W., and Taylor, C. A software framework for creating patient specific geometric models from medical imaging data for simulation based medical planning ofvascular surgery. In *Lecture Notes in Computer Science (including subseries Lecture Notes in Artificial Intelligence and Lecture Notes in Bioinformatics)* (10 2001), vol. 2208, Springer Verlag, pp. 449–456.

[148] Wolberg, A. S., and Campbell, R. A. Thrombin generation, fibrin clot formation and hemostasis. *Transfusion and Apheresis Science 38*, 1 (2 2008), 15–23.

[149] Xu, Z., Chen, N., and Kamocka, M. M. e. a. A multiscale model of thrombus development. *Journal of the Royal Society, Interface / the Royal Society 5*, 24 (2008), 705–22.

[150] Xu, Z., Kamocka, M., Alber, M., and Rosen, E. D. Computational approaches to studying thrombus development. *Arteriosclerosis, Thrombosis, and Vascular Biology 31*, 3 (2011), 500–505.

[151] Yazdani, A., Li, H., Bersi, M. R., Di Achille, P., Insley, J., Humphrey, J. D., and Karniadakis, G. E. Data-driven modeling of hemodynamics and its role on thrombus size and shape in aortic dissections. *Scientific reports 8*, 1 (2018), 2515.

[152] Yun, S. H., Sim, E. H., Goh, R. Y., Park, J. I., and Han, J. Y. Platelet activation: The mechanisms and potential biomarkers, 2016.

[153] Zlobina, K. E., and Guria, G. T. Platelet activation risk index as a prognostic thrombosis indicator. *Scientific Reports 6*, 1 (7 2016), 1–6.